2006

On The Use Of Variable Coherence In Inverse Scattering Problems

Erwan Baleine
University of Central Florida

On the use of variable coherence in inverse scattering problems

by

Erwan Baleine
M.S. École Supérieure d'Optique, 2002
M.S. University of Central Florida, 2003

A dissertation submitted in partial fulfillment of the requirements
for the degree of Doctor of Philosophy
in the Department of Optics
in the College of Optics and Photonics, CREOL
at the University of Central Florida
Orlando, Florida

Fall Term
2006

Major Professor: Aristide Dogariu

ABSTRACT

Even though most of the properties of optical fields, such as wavelength, polarization, wavefront curvature or angular spectrum, have been commonly manipulated in a variety of remote sensing procedures, controlling the degree of coherence of light did not find wide applications until recently. Since the emergence of optical coherence tomography, a growing number of scattering techniques have relied on temporal coherence gating which provides efficient target selectivity in a way achieved only by bulky short pulse measurements. The spatial counterpart of temporal coherence, however, has barely been exploited in sensing applications. This dissertation examines, in different scattering regimes, a variety of inverse scattering problems based on variable spatial coherence gating.

Within the framework of the radiative transfer theory, this dissertation demonstrates that the short range correlation properties of a medium under test can be recovered by varying the size of the coherence volume of an illuminating beam. Nonetheless, the radiative transfer formalism does not account for long range correlations and current methods for retrieving the correlation function of the complex susceptibility require cumbersome cross-spectral density measurements. Instead, a variable coherence tomographic procedure is proposed where spatial coherence gating is used to probe the structural properties of single scattering media over an extended volume and with a very simple detection system.

Enhanced backscattering is a coherent phenomenon that survives strong multiple scattering. The variable coherence tomography approach is extended in this context to diffusive

media and it is demonstrated that specific photon trajectories can be selected in order to achieve depth-resolved sensing. Probing the scattering properties of shallow and deeper layers is of considerable interest in biological applications such as diagnosis of skin related diseases.

The spatial coherence properties of an illuminating field can be manipulated over dimensions much larger than the wavelength thus providing a large effective sensing area. This is a practical advantage over many near-field microscopic techniques, which offer a spatial resolution beyond the classical diffraction limit but, at the expense of scanning a probe over a large area of a sample which is time consuming, and, sometimes, practically impossible. Taking advantage of the large field of view accessible when using the spatial coherence gating, this dissertation introduces the principle of variable coherence scattering microscopy. In this approach, a subwavelength resolution is achieved from simple far-zone intensity measurements by shaping the degree of spatial coherence of an evanescent field.

Furthermore, tomographic techniques based on spatial coherence gating are especially attractive because they rely on simple detection schemes which, in principle, do not require any optical elements such as lenses. To demonstrate this capability, a correlated lensless imaging method is proposed and implemented, where both amplitude and phase information of an object are obtained by varying the degree of spatial coherence of the incident beam.

Finally, it should be noted that the idea of using the spatial coherence properties of fields in a tomographic procedure is applicable to any type of electromagnetic radiation. Operat-

ing on principles of statistical optics, these sensing procedures can become alternatives for various target detection schemes, cutting-edge microscopies or x-ray imaging methods.

In memory of my brother, Pierre

To my parents

ACKNOWLEDGMENTS

I wish to acknowledge my advisor, Dr. Aristide Dogariu, for his support, guidance, and above all, his friendship, which has made this PhD an unforgettable journey. It was a pleasure and an honor to work with him.

I am grateful to Professor Emil Wolf for his kind and continuous encouragements.

The Random Group has been a place of countless captivating discussions and interactions. Thanks to all of the current and former members for their priceless support.

A mi familia cubana, gracias por el recibimiento tan acogedor y por su hospitalidad. Gracias por todo.

Merci à toute ma famille pour leur soutient tout au long de ma thèse. Un gros bisou à Papa et Maman pour leur patience et leurs encouragements. Sans vous tous, rien de tout cela ne serait arrivé.

Thank you Clara for being with me...

TABLE OF CONTENTS

LIST OF FIGURES . . . . . **xii**

LIST OF SYMBOLS . . . . . **xxi**

CHAPTER 1 INTRODUCTION **1**

CHAPTER 2 SPATIAL COHERENCE PROPERTIES AND SCATTERING OF PARTIALLY COHERENT BEAMS **7**

2.1 Second-order coherence properties of partially coherent fields 8

2.1.1 Space-frequency representation of partially coherent fields 8

2.1.2 Angular correlation of partially coherent fields 10

2.1.3 Quasi-homogeneous fields 11

2.2 Scattering of partially coherent fields in random media 17

2.2.1 Scalar scattering theory 17

2.2.2 Perturbation theory and the first-order Born approximation 19

2.2.3 Multiple scattering and the field moments 23

2.2.4 The radiative transfer equation 26

2.2.5 The diffusion equation 28

CHAPTER 3 TRANSPORT EQUATION OF THE COHERENCE FUNCTION 32

3.1 Wigner distribution - Transport equation: the small angle approximation . . 34

3.2 Divergence of a partially coherent beam 36

3.3 Propagation of a partially coherent beam in a particulate medium 39

3.4 Conclusion 45

CHAPTER 4 VARIABLE COHERENCE TOMOGRAPHY 47

4.1 Spatial coherence shaping 48

4.2 Variable coherence tomography – Principle 53

4.3 Experimental results 56

4.3.1 Construction of a correlated scattering system 56

4.3.2 Synthesis of the partially coherent probe beam 58

4.3.3 Scattering potential reconstruction using variable coherence tomography 60

4.4 Conclusion 64

CHAPTER 5 ENHANCED BACKSCATTERING WITH SHAPED PARTIALLY COHERENT LIGHT 67

5.1 Enhanced coherent backscattering 68

5.1.1 Multiple scattering and weak localization of light 68

5.1.2 Angular dependence in the diffusion approximation 71

5.1.3 Polarization of the enhanced backscattering peak 75

5.2 Enhanced backscattering of partially coherent light 76

5.3 Experimental results for a diffusive medium 85

5.4 Conclusion 90

CHAPTER 6 VARIABLE COHERENCE SCATTERING MICROSCOPY 92

6.1 Spatial coherence shaping of an evanescent field 93

6.2 Experimental results on a monolayer of microspheres 98

6.3 Conclusion 103

CHAPTER 7 CORRELATED IMAGING WITH SHAPED SPATIALLY PARTIALLY COHERENT LIGHT 105

7.1 Correlated imaging 106

7.1.1 Correlated imaging with a classical source 106

7.1.2 Correlated imaging with shaped spatially partially coherent light . . . 111

7.1.3 Klyshko's geometrical optics approach 119

7.1.4 Duality between classical and two-photon correlated imaging 121

7.2 Experimental results 126

7.3 Conclusion 130

CHAPTER 8 SUMMARY OF ORIGINAL CONTRIBUTIONS AND CONCLUSIONS **132**

APPENDIX: PUBLICATIONS AND PRESENTATIONS **137**

LIST OF REFERENCES **142**

LIST OF FIGURES

2.1 Typical scattering experiment configuration. 21

3.1 Illustration of the notation relating to the propagation of the beam. 35

3.2 Experimental setup used to study the scattering of partially coherent beams. 40

3.3 Three-dimensional representation of the angular intensity $I^{(s)}(\theta)$ recorded by the CCD detector. 41

3.4 Divergence for partially coherent beams with different coherence parameters. The dots are the experimental data and the continuous curve represents the result of calculations based on Eq. (3.2). 42

3.5 Normalized angular scattered intensity for an incident beam with a diameter of 9mm and a coherence parameter $\sigma_\mu = 390\mu m$ (A) and for $\sigma_\mu = 57\mu m$ (B). Solid curves, the experimental results; Dashed curves, the calculations based on Eq. (3.2). 43

3.6 The rms angular spread of the beam after the particulate medium relative to its initial value. The coherence length σ_μ of the partially coherent beam ranges from 1.3mm to $57\mu m$. 44

4.1 Typical scattering configuration for variable coherence tomography. 49

4.2 Intensity pattern in the plane (ξ, η) of the source. 51

4.3 Degree of spatial coherence $\mu^{(i)}(\Delta x, \Delta y, \Delta z)$ of the incident field plotted as a function of the two points separation Δy and Δz and for $\Delta x = 0$. 52

4.4 Schematic representation of the scattering medium. 57

4.5 Experimental setup for variable coherence tomography. 59

4.6 Oscillating part of the scattered intensity for $x_0 = 0.2mm$ and three different values of y_0. From top to bottom, $y_0 = -3mm$, $y_0 = -3.3mm$, $y_0 = -2.6mm$. The dashed line is the intensity envelope. 62

4.7 Envelopes of the scattered intensity for $x_0 = 0.2mm$ and $y_0 = -3mm$, $y_0 = -3.3mm$ and $y_0 = -2.6mm$. 63

5.1 (a) Scattering trajectory contributing to the incoherent background intensity. (b) Time reciprocal path at the origin of coherent enhanced backscattering. . 69

5.2 Angular intensity $\alpha(\mathbf{s}_b, \mathbf{s}_a)$ backscattered from a diffusive medium characterized by $l_t = 100\mu m$ and illuminated by a monochromatic plane wave at normal incidence, i.e. $\mathbf{s}_a = \mathbf{z}$. The albedo is normalized to the background intensity at large angles. 74

5.3 Schematic of the experimental setup used for enhanced backscattering with shaped spatially partially coherent light. 76

5.4 Normalized representation of the coherence function g defined in Eq. (5.14) and plotted for the parameters $R = 1.5mm$, $\lambda = 532nm$ and $f = 200mm$. . . 78

5.5 (a) Scattering paths contributing to the coherent backscattering peak when the incident light has a shaped degree of spatial coherence. (b) Photon migration path distributions for the light entering and exiting at points separated by ρ_0 [75]. The medium occupies the half space $z \geq 0$ and the coordinate units are normalized to the diffusive light migration length $L_{eff} = 1/\mu_{eff}$. . 83

5.6 Distribution of backscattered intensity $\overline{I_b}(\mathbf{s}, \boldsymbol{\rho}_0)$ normalized to the background intensity. The calculation is performed for an incident field characterized by the angular distribution $I(\mathbf{s}_0, \boldsymbol{\rho}_0)$ with $\rho_0 = 100\mu m$ (top) and $\rho_0 = 200\mu m$ (bottom). The diffusive medium has a transport mean free path $l_t = 100\mu m$ while the source, with a radius set to $R_s = 1.5mm$, is located at a focal distance $f = 200mm$ from L_s. 84

5.7 Angular intensity distribution $I(\mathbf{s}_0, \boldsymbol{\rho}_0)$ of the incident partially coherent beam when the distance between correlated speckle is $\rho_0 = 220\mu m$. 85

5.8 Schematic of the experimental detection setup used for enhanced backscattering with shaped spatially partially coherent light. 87

5.9 (solid line) Modulated part $\widetilde{I_c}(s_x, \boldsymbol{\rho}_0)$ of the angular scattered intensity measured for $\rho_0 = 72\mu m$ and $\rho_0 = 142\mu m$, respectively. (dashed lined) Fit of the experimental data with a cosine function in order to determine the amplitude of the modulation. 88

5.10 Experimental measurement of $P(\rho)$ as a function of the transverse separation ρ. The dashed curves correspond to the analytical solution for $P(\rho)$ obtained from Eqs. (5.10) and (5.12) for $l_t = 70$, 100 and $130\mu m$. 89

6.1 Normalized cross-spectral density of the evanescent field as evaluated from Eq. (6.3) for $z_1 = z_2 = 0$, $Q(\mathbf{q}) = 1$ and $k_0 \leq |\mathbf{q}| \leq nk_0$. 96

6.2 Schematic of the setup used to generate evanescent waves with transverse wave vectors $k_0 \leq |\mathbf{q}| \leq nk_0$. 99

6.3 High spatial frequency content of the intensity $I^{(m)}(\mathbf{k}_{sz}, \mathbf{q})$ scattered by a monolayer of $0.97\mu m$ diameter particles. The solid line represents the results of the Hankel transform of the measured intensity $I^{(s)}(\mathbf{k}_{sz},\Delta\rho_0)$ whereas the dashed line corresponds to the analytical result obtained as explained in the text. The inset shows part of the normalized intensity $I^{(s)}(\mathbf{k}_{sz},\Delta\rho_0)$ obtained experimentally for $0 \leq \Delta\rho_0 \leq 10\mu m$. 102

7.1 Schematic of the setup used for correlated imaging. The source is thermal, quasi monochromatic and spatially incoherent with a uniform intensity distribution. 107

7.2 Schematic of the setup used for correlated imaging with shaped spatially partially coherent light. 112

7.3 Reference intensity as a function of the coherence parameter $\mathbf{\Delta r}_0$ and normalized to its asymptotic limit $g(0)$. The wavelength is $\lambda = 532nm$ and the source parameters are $f = 62mm$, $m = 1$, $\phi = 0$ and $R = 2mm$. 117

7.4 Measurement of the intensities $\langle I_1 \rangle_{meas}$, $\langle I_2 \rangle_{meas}$, and the coincidence counts $G^{(2)}_{meas}$ as a function of the position r_2 of the detector D_2. The number of counts $\langle I_1 \rangle_{meas}$ and $\langle I_2 \rangle_{meas}$ are normalized to their average value and then shifted in the graph for better legibility. $G^{(2)}_{meas}$ was normalized to its average background value. 118

7.5 Scheme (a) corresponds to the unfolded representation of the setup used in conventional correlated imaging where the spatially incoherent source S has a uniform intensity distribution. In scheme (b), the intensity distribution across S is modulated according to Eq. (7.17). 121

7.6 Unfolded representation of the two-photon correlated imaging setup. The complex Fourier transform of the object is reconstructed by using a biphoton source with adjustable degree of entanglement. 122

7.7 Schematic of the experimental setup used for correlated imaging with shaped spatially partially coherent light. 127

7.8 Coincidence counts $G^{(2)}$ and intensities in the object arm (I_1) and the reference arm (I_2) measured as a function of the source parameter Δr_0 for $\phi = 0$ (solid curve) and $\phi = \pi$ (dotted curve) when the grating is in the position $T(0) = 0$. The intensities are normalized with respect to the values obtained without the object and for $\Delta r_0 \sim 200\mu m$. 128

7.9 The analytic Fourier transform of the grating's transmittance is shown in graphic (a1) for the case $T(0) = 1$. The measured amplitude $|\chi_e|^2$ and the phase cosine are represented in plots (a2) and (a3), respectively. As shown in (b2) and (b3), the same measurements were performed in the case $T(0) = 0$ corresponding to the analytic Fourier transform plotted in (b1). 129

LIST OF SYMBOLS

λ	Wavelenght
$\boldsymbol{k}$	Wave vector
ω	Frequency
W	Cross-spectral density
J_1	First order Bessel function
$\mathcal{W}$	Wigner distribution function
μ_s, μ_a	Scattering and absorption coefficients
l_s	Scattering mean free path
l_t	Transport mean free path

CHAPTER 1

INTRODUCTION

The fluctuations in the optical properties of random media usually prevent direct imaging techniques from providing relevant structural information. Instead, optical sensing procedures based on statistical approaches must be considered in order to target specific properties, which are pertinent to the material system under test. In this respect, a significant effort has been devoted to relate the descriptors of a scattered wave to the effective parameters such as the particle sizes, the transport mean-free-path or the correlation of the scattering potential.

Usually, in addition to characterizing the scattered field, solving the inverse scattering problem requires varying one of the properties of the incident wave such as wavelength, polarization, angle of incidence, wavefront curvature or angular spectrum. For instance, Mueller polarimetry operates by controlling the state of polarization of the illuminating beam while polarimetric measurements are performed on the scattered field [1]. Spectroscopic procedures are based on changing the wavelength of the incoming light. A recently introduced backscattering technique relies on adjusting the angular momentum of an incident vortex beam in order to retrieve the scattering parameters of a diffusive medium [2]. Diffraction tomography permits the reconstruction of deterministic and weakly scattering objects by changing the direction of the illuminating plane wave [3]. In the case of random media, mea-

suring the correlation function of the scattering potential is performed using fully coherent plane waves illuminating the object at different angles of incidence and then measuring the cross-spectral density of the field scattered in two different planes [4]. In multiple scattering media, various positions of the light sources are needed to be able to solve the diffusion equation and reconstruct biological images [5].

Whereas most of the optical field's properties mentioned above have been commonly manipulated in a variety of remote sensing procedures, controlling the degree of coherence of light did not find wide applications until recently with the emergence of optical coherence tomography [6]. In this procedure, temporal coherence gating isolates the single scattering contributions from a diffuse signal to produce, for example, depth resolved images of the retina [7]. Since the introduction of optical coherence tomography, a growing number of scattering techniques have relied on temporal coherence gating, which provides path-length resolved measurements of scattering trajectories [8] in a way achieved only by cumbersome short pulse measurements [9].

Even though the scattering of spatially partially coherent fields has been extensively studied [10] and the relationship between spatial coherence and radiometry has received considerable attention [11, 12], the spatial counterpart of temporal coherence gating has been given little consideration in sensing applications. A notable accomplishment is the so-called fluctuation microscopy where higher order correlation of a distribution of atoms is probed by varying the spatial coherence volume of an electron beam and recording the scattered intensity [13]. Recently, a tomographic technique has been developed based on

the energy theorem for scattering of spatially partially coherent beams [14]. This method avoids the problem of phase measurement encountered in diffraction tomography and allows for determining the absorptive part of the susceptibility for a deterministic scatterer or the fluctuation strength of a quasi-homogeneous random medium. Notably, one experiment has relied on shaping, in the longitudinal direction, the degree of spatial coherence of the incident field [15]. However, this technique was applied to profilometry and the interaction of the incident field with a scattering medium was not considered.

Based on shaping the spatial coherence of the incident radiation, this dissertation proposes and demonstrates several novel procedures for solving inverse problems related to the scattering of light in scattering media. A number of sensing techniques applicable to different scattering regimes are introduced. We demonstrate that imaging, characterization of structural properties, or depth sensitive sensing in both deterministic and random media can be achieved using very simple detection schemes.

After introducing the general formalism necessary for describing spatial properties of partially coherent fields, Chapter 2 of this dissertation presents the basis of the variable coherence tomographic approach and focuses on the fundamental role of second-order coherence properties in the scattering of light in random media. An overview of the multiple scattering theory establishes the main concepts which link a rigorous description of the scattered field to the conventional radiative transfer approach.

Although it was already shown in the late 1960's that the small angle approximation of the radiative transfer equation accounts for the partial coherence of the field [16], there is

limited experimental data that demonstrate the effect of the degree of spatial coherence on the propagation of a beam in a particulate media. Using the radiative transfer formalism, we show in Chapter 3 that both the density and the size of particles in a multiple scattering medium can be measured by varying the size of the coherence volume of the incident field. Unfortunately, the radiative transfer equation only accounts for small range correlation in the inhomogeneities and a different approach must be considered in order to evaluate the long-range structural properties of a scattering system.

Based on the concept of spatial coherence gating, Chapter 4 introduces the concept of variable coherence tomography. Using the first order Born approximation, we show that coherent scattering can be induced from different regions of a medium by shaping the degree of spatial coherence of the illuminating beam. The structural characteristics of the medium, given by the second-order statistical properties of the complex susceptibility, are then recovered from far-field intensity measurements performed in a single direction. Thus, variable coherence tomography is based on a much simpler detection scheme in comparison to other approaches which require evaluating the cross-spectral density in different planes [4].

Since the first Born approximation is only valid in the single scattering regime, variable coherence tomography can hardly be generalized to higher order scattering regimes. However, in highly diffusive media, the influence of long-range correlations is enhanced in the exact backscattering direction as a result of constructive interferences between time reversal trajectories. Experimentally however, current techniques do not have the ability to differentiate between the different scattering paths. Measurements of long-range correlations

are either integrated over all scattering paths or relates only to the superficial layers of the medium [17]. After briefly reviewing the phenomenon of enhanced backscattering [18], we demonstrate in Chapter 5 that spatial coherence gating offers the possibility to select of specific photon trajectories, thus providing a depth sensitive measurement.

Superresolution is the ultimate goal in microscopy. Methods based on spatial coherence gating are particularly attractive since the resolution is defined by the size of the coherence volume while the active sensing area is determined by the extended spatial dimensions of the illuminating beam. In classical microscopic techniques, on the other hand, high resolution imaging is achieved by using spatial gating techniques which rely on either the focusing capability of a coherent field or the confinement of light at the end of a fiber tip as, for instance, in near-field optical scanning microscopy [19]. However, because a scanning operation is required to build up the image point by point, the approach is time consuming and, moreover, it is practically restricted to imaging of very small areas. In Chapter 6, we introduce and demonstrate the principle of variable coherence scattering microscopy, where an object under test is probed by an evanescent field which has its spatial coherence properties adjustable at subwavelength scales. The results are remarkable in the sense that the subwavelength resolution is achieved over a large field of view from simple far zone intensity measurements. Notably, this technique can be implemented without any moving parts for both illuminating the sample and detecting the scattered light.

It should be pointed out that, from a practical perspective, tomographic techniques based on variable coherence are especially appealing because they rely on a simple detection scheme

which, potentially, does not require any optical elements such as lenses. In the last Chapter of this dissertation, we propose and implement a correlated lensless imaging method where both the amplitude and phase information about the spatial frequencies of an object can be recovered by varying the degree of spatial coherence of the incident beam.

CHAPTER 2

SPATIAL COHERENCE PROPERTIES AND SCATTERING OF PARTIALLY COHERENT BEAMS

The first part of this chapter is devoted to the statistical representation of partially coherent fields in the frame work of the coherence theory [20]. We introduce the general concepts of cross-spectral density and angular correlation, which are then applied to the particular case of quasi-uniform fields. In the second part, we study the scattering of partially coherent fields by inhomogeneous media. Starting from the scalar wave scattering theory in random inhomogeneous media, a general solution for the scattered field is introduced based on perturbation theory. Within the limits of the single scattering regime, this result is applied to relate the scattered intensity to the coherence properties of the incident field. Using the equations for the statistical moments of the wave field, the main approximations leading to the expression of the radiative transfer equation are then presented. This formulation permits treating the propagation of the second-order coherence properties of the field in a multiple scattering regime.

2.1 Second-order coherence properties of partially coherent fields

2.1.1 Space-frequency representation of partially coherent fields

An electromagnetic field at a position vector $\mathbf{r}$ and a time t can be represented by the real variable $V^{(r)}(\mathbf{r},t)$. In any realistic situation where the light originates from a thermal source or a laser, $V^{(r)}$ is a random variable which fluctuates as a function of time and, therefore, only a statistical approach can be considered. It is mathematically convenient to use the analytic signal $V(\mathbf{r},t)$ associated with the real field variable $V^{(r)}(\mathbf{r},t)$ [21]. One can regard $V(\mathbf{r},t)$ as a particular member of the ensemble $\{V(\mathbf{r},t)\}$ composed of all the possible field realizations. Since the oscillations of an optical field are too fast to be recorded by any detector, the measured quantity is often proportional to the intensity, which depends on the second-order correlation of the field at two space-time points. The correlation between the fluctuations $V(\mathbf{r}_1,t_1)$ of the field at position $\mathbf{r}_1$ and time t_1 and the fluctuation $V(\mathbf{r}_2,t_2)$ at position $\mathbf{r}_2$ and time t_2 is evaluated by the cross-correlation function defined as

$$\Gamma(\mathbf{r}_1,\mathbf{r}_2;t_1,t_2) = \langle V^*(\mathbf{r}_1,t_1)\, V(\mathbf{r}_2,t_2)\rangle\,, \tag{2.1}$$

where $\langle ...\rangle$ denotes the ensemble average over the field realizations.

In most applications the field is considered to be stationary, at least in the wide sense, meaning that the random process is independent of the origin of time and that the cross-correlation function depends only on the time difference $\tau = t_1 - t_2$. Moreover, the field is assumed to be ergodic and therefore the ensemble average is equivalent to a time average.

Consequently, $\Gamma(\mathbf{r}_1, \mathbf{r}_2; t_1, t_2)$ can be replaced by the mutual coherence function [21]

$$\Gamma(\mathbf{r}_1, \mathbf{r}_2, \tau) = \langle V^*(\mathbf{r}_1,t)\, V(\mathbf{r}_2,t+\tau)\rangle_t\,, \tag{2.2}$$

where $\langle ...\rangle_t$ denotes the time average of the random process. As the instantaneous intensity is defined as $I(\mathbf{r},t) = V^*(\mathbf{r},t)\, V(\mathbf{r},t)$, we deduce from Eq. (2.2) that $\Gamma(\mathbf{r}, \mathbf{r}, 0)$ represents the average intensity at point $\mathbf{r}$.

Because the field fluctuates in time, it cannot be considered monochromatic and, according to the generalized Wiener-Khintchine theorem, its properties may be characterized by the cross-spectral density function

$$W(\mathbf{r}_1, \mathbf{r}_2, \omega) = \int_{-\infty}^{\infty} \Gamma(\mathbf{r}_1, \mathbf{r}_2, \tau) \exp(i\omega t)\, dt. \tag{2.3}$$

It has been shown that $W(\mathbf{r}_1, \mathbf{r}_2, \omega)$ represents the correlation between two monochromatic members of a suitably constructed ensemble $\{U(\mathbf{r}, \omega) \exp(-i\omega t)\}$ composed of all the monochromatic realizations of the field [22]. The cross-spectral density takes then the form

$$W(\mathbf{r}_1, \mathbf{r}_2, \omega) = \langle U^*(\mathbf{r}_1, \omega)\, U(\mathbf{r}_2, \omega)\rangle_\omega\,, \tag{2.4}$$

where $\langle ...\rangle_\omega$ is the statistical average over the frequency-dependant realizations ensemble.

The cross-spectral density depends on the intensity's spatial distribution and, in order to characterize the spatial coherence of the field, it is useful to normalize $W(\mathbf{r}_1, \mathbf{r}_2, \omega)$ by defining the spectral degree of coherence:

$$\mu(\mathbf{r}_1, \mathbf{r}_2, \omega) = \frac{W(\mathbf{r}_1, \mathbf{r}_2, \omega)}{\sqrt{\langle I(\mathbf{r}_1, \omega)\rangle \langle I(\mathbf{r}_2, \omega)\rangle}}, \tag{2.5}$$

where $\langle I(\mathbf{r},\omega)\rangle \equiv W(\mathbf{r},\mathbf{r},\omega)$ is the averaged spectral density of the field at position $\mathbf{r}$ and frequency ω.

Very often an electromagnetic field propagates close to a given direction and can be considered as a beam. It follows that the electric field mainly lays in a plane transverse to the direction of propagation. The correlation between two orthogonal components of the electric field characterizes the polarization of the beam. In general, the beam is described by the 2×2 cross-spectral density matrix [23]

$$\underline{\underline{\mathbf{W}}} \equiv W_{ij}(\mathbf{r}_1,\mathbf{r}_2,\omega) = \langle U_i^*(\mathbf{r}_1,\omega)\, U_j(\mathbf{r}_2,\omega)\rangle\,, \tag{2.6}$$

where i and j are two orthogonal directions in a plane transverse to the beam axis. A scalar treatment of the field will be considered in the subsequent sections of this dissertation.

2.1.2 Angular correlation of partially coherent fields

When propagating into the half-space $z \geq 0$ free of sources, the monochromatic wavefield realization $U(\mathbf{r},\omega)$ can be decomposed in terms of its angular spectrum of planes waves [24]

$$U(\mathbf{r},\omega) = \iint_{-\infty}^{\infty} a(p,q;\omega)\exp\left[ik\left(px+qy+mz\right)\right]dpdq, \tag{2.7}$$

where $\mathbf{r} = (x,y,z)$ is the space position vector, $k = \omega/c$ is the wave number and $a(p,q;\omega)$ is the spectral-amplitude in the plane-wave mode decomposition of the field. The plane wave modes can be regrouped into two categories. The propagating or homogeneous waves

satisfy $p^2 + q^2 \leq 1$ with $m = \sqrt{1 - p^2 - q^2}$, while the evanescent or inhomogeneous waves correspond to $p^2 + q^2 > 1$ with $m = i\sqrt{p^2 + q^2 - 1}$.

Substituting Eq. (2.7) into Eq. (2.4), the cross-spectral density $W(\mathbf{r}_1, \mathbf{r}_2, \omega)$ at two points $\mathbf{r}_1 = (x_1, y_1, z_1)$ and $\mathbf{r}_2 = (x_2, y_2, z_2)$ in the half space $z \geq 0$ becomes

$$\begin{aligned} W(\mathbf{r}_1, \mathbf{r}_2, \omega) &= \iiiint_{-\infty}^{\infty} \mathcal{A}(p_1, q_1; p_2, q_2; \omega) \\ &\quad \times \exp\left[-ik\left(p_1 x_1 + q_1 y_1 + m_1^* z_1 - p_2 x_2 - q_2 y_2 - m_2 z_2\right)\right] dp_1 dq_1 dp_2 dq_2, \end{aligned} \tag{2.8}$$

where the angular correlation function of the field $\mathcal{A}(p_1, q_1; p_2, q_2; \omega)$ is defined as

$$\mathcal{A}(p_1, q_1; p_2, q_2; \omega) = \langle a^*(p_1, q_1; \omega)\, a(p_2, q_2; \omega) \rangle . \tag{2.9}$$

From Eq. (2.8), $W(\mathbf{r}_1, \mathbf{r}_2, \omega)$ can be regarded as a superposition of mutually correlated plane waves. The correlation between the different homogeneous and evanescent plane waves is characterized by the function $\mathcal{A}$.

2.1.3 Quasi-homogeneous fields

In a typical scattering experiment, where a partially coherent field is incident upon a particle, two simple mechanisms can influence the scattering process [25]. One relates to the modulation of intensity over the object, while the other is associated with the spatial coherence characteristic of the field. In order to remove the former effect and obtain a scattering process dependant only on the coherence properties, we consider an incident field

with a uniform average intensity $\langle I_0 \rangle$, at least in the volume occupied by the object in the absence of inhomogeneities. It follows from Eq. (2.8) that the angular correlation function must satisfy the relation

$$\begin{aligned} \langle I_0(\omega) \rangle &= \iiiint_{-\infty}^{\infty} \mathcal{A}\left(p_1, q_1; p_2, q_2; \omega\right) \\ &\quad \times \exp\left\{-ik\left[x\left(p_1 - p_2\right) + y\left(q_1 - q_2\right) + z\left(m_1^* - m_2\right)\right]\right\} dp_1 dq_1 dp_2 dq_2, \end{aligned} \tag{2.10}$$

where $I_0(\omega)$ is independent of x, y and z. This last relation must also hold for the particular case where $z = 0$, and defining the new variables $\Delta p = p_1 - p_2$, $\Delta q = q_1 - q_2$, $\overline{p} = \left(p_1 + p_2\right)/2$ and $\overline{q} = \left(q_1 + q_2\right)/2$, Eq. (2.10) becomes

$$\begin{aligned} \langle I_0(\omega) \rangle &= \iiiint_{-\infty}^{\infty} \mathcal{A}\left(\overline{p}, \overline{q}, \Delta p, \Delta q; \omega\right) \\ &\quad \times \exp\left[-ik\left(x\Delta p + y\Delta q\right)\right] d\overline{p} d\overline{q} d\Delta p d\Delta q. \end{aligned} \tag{2.11}$$

Noting that the integration with respect to the coordinate difference and the mean position separates, one can rewrite Eq. (2.11) in the form

$$\begin{aligned} \langle I_0(\omega) \rangle &= \iint_{-\infty}^{\infty} \overline{\mathcal{A}}\left(\Delta p, \Delta q; \omega\right) \\ &\quad \times \exp\left[-ik\left(x\Delta p + y\Delta q\right)\right] d\Delta p d\Delta q, \end{aligned} \tag{2.12}$$

where

$$\overline{\mathcal{A}}\left(\Delta p, \Delta q; \omega\right) = \iint_{-\infty}^{\infty} \mathcal{A}\left(\overline{p}, \overline{q}, \Delta p, \Delta q; \omega\right) d\overline{p} d\overline{q}. \tag{2.13}$$

According to Eq. (2.12), $\overline{\mathcal{A}}$ must be of the form

$$\overline{\mathcal{A}}\left(\Delta p, \Delta q; \omega\right) \propto \delta\left(\Delta p\right) \delta\left(\Delta q\right), \tag{2.14}$$

with δ being the Dirac delta function. It follows from Eqs. (2.13) and (2.14) that the angular correlation function can be expressed as

$$\mathcal{A}\left(\overline{p},\overline{q},\Delta p,\Delta q;\omega\right)=\left\langle I_a\left(\overline{p},\overline{q};\omega\right)\right\rangle \delta\left(\Delta p\right)\delta\left(\Delta q\right), \tag{2.15}$$

where $\left\langle I_a\left(\overline{p},\overline{q};\omega\right)\right\rangle = \left\langle a^*\left(\overline{p},\overline{q};\omega\right) a\left(\overline{p},\overline{q};\omega\right)\right\rangle$ is the spectral intensity of the plane wave defined by the wave vector $\mathbf{k}=(\overline{p},\overline{q},\overline{m})$.

The expression of $\mathcal{A}$ in Eq. (2.15) demonstrates that, in order to have a constant intensity in the plane $(x,y,z=0)$, the field must be composed of mutually uncorrelated plane waves. Indeed, any correlation between the plane waves would create interferences and therefore modulation would appear in the average intensity. Experimentally, such fields can be generated by placing, in the focal plane of a lens, a spatially incoherent source such as a thermal source or a laser beam impinging upon a rotating diffuser.

In order to deduce general properties about the degree of spatial coherence from the expression of the angular correlation function obtained in Eq. (2.15), we are considering in the next sections two special cases, one where only propagating waves are present and a second case where the field is only evanescent.

2.1.3.1 Degree of coherence of propagating fields

When measurements are performed sufficiently far from the source, evanescent waves can be neglected and the field is only composed of propagating plane waves with wave vector $\mathbf{k}$

such that $m_1^* = m_2 = \sqrt{1-p^2-q^2}$. Consequently, substituting Eq. (2.15) into Eq. (2.10), the average intensity $\langle I_0(\omega)\rangle$ becomes

$$\langle I_0(\omega)\rangle = \iint_{-\infty}^{\infty} \langle I_a\left(\overline{p},\overline{q};\omega\right)\rangle \, d\overline{p}d\overline{q}. \tag{2.16}$$

Equation (2.16) shows that, as desired, the average intensity $\langle I_0(\omega)\rangle$ is independent of x, y and z. Furthermore, using Eq. (2.5) and inserting Eq. (2.15) into Eq. (2.8), we obtain the following expression for the degree of spatial coherence:

$$\begin{aligned} \mu(\mathbf{r}_1,\mathbf{r}_2,\omega) &= \frac{1}{\langle I_0(\omega)\rangle}\iint_{-\infty}^{\infty} \langle I_a\left(\overline{p},\overline{q};\omega\right)\rangle \\ &\quad \times \exp\left\{-ik\left[\overline{p}\left(x_1-x_2\right)+\overline{q}\left(y_1-y_2\right)+\overline{m}\left(z_1-z_2\right)\right]\right\} d\overline{p}d\overline{q}. \end{aligned} \tag{2.17}$$

One can see from Eq. (2.17) that the function $\mu(\mathbf{r}_1,\mathbf{r}_2,\omega)$ is homogeneous meaning that it depends on $\mathbf{r}_1$ and $\mathbf{r}_2$ only through the difference $\mathbf{r}_1-\mathbf{r}_2$. Fields with such spatial coherence property are known as Schell-model fields [26]. Furthermore, when the intensity variations are much slower than the variations of $\mu(\mathbf{r}_1-\mathbf{r}_2,\omega)$ as a function of $\mathbf{r}_1-\mathbf{r}_2$, Schell-model fields are called quasi-uniform or quasi-homogeneous [27]. Since, in our case, the intensity is constant, the incident cross-spectral density inside the volume occupied by the scattering object can be written as

$$W(\mathbf{r}_1,\mathbf{r}_2,\omega) = \langle I_0\left(\omega\right)\rangle \, \mu(\mathbf{r}_1-\mathbf{r}_2,\omega). \tag{2.18}$$

According to Eq. (2.17), $W(\mathbf{r}_1, \mathbf{r}_2, \omega)$ is related to the plane wave spectral intensity $\langle I_a(p, q; \omega)\rangle$ through a Fourier transform relationship:

$$W(\mathbf{r}_1, \mathbf{r}_2, \omega) = \iint_{-\infty}^{\infty} \langle I_a(p, q; \omega)\rangle \times \exp\left[-ik\left(p\Delta x + q\Delta y + m\Delta z\right)\right] dpdq, \tag{2.19}$$

where $\Delta x = x_1 - x_2$, $\Delta y = y_1 - y_2$ and $\Delta z = z_1 - z_2$. Equation (2.19) corresponds to the van Cittert-Zernike theorem for an incoherent source with effective source distribution $\langle I_a(p, q; \omega)\rangle$ [28]. Since $W(\mathbf{r}_1, \mathbf{r}_2, \omega)$ depends only on the coordinate difference Δx, Δy and Δz, the cross-spectral density is invariant upon propagation [29]. This involves that, in the case where such a field illuminates an object, the scattering process does not depend on the relative position of the object in the incident field. This property has the advantage of relaxing the alignment constrains in an experimental procedure.

2.1.3.2 Degree of coherence of evanescent fields

If the field in Eq. (2.7) is only composed of evanescent waves, then we have $-m_1^* = m_2 = i\sqrt{p^2 + q^2 - 1}$. Substituting Eq. (2.15) into Eq. (2.10), the average intensity $\langle I_e(\omega)\rangle$ becomes

$$\langle I_e(z, \omega)\rangle = \iint_{-\infty}^{\infty} \langle I_a(\overline{p}, \overline{q}; \omega)\rangle \exp\left(-2\gamma z\right) d\overline{p}d\overline{q}, \tag{2.20}$$

where $\gamma = k\sqrt{\overline{p}^2 + \overline{q}^2 - 1}$.

As expected from an evanescent field, there is an exponential decay of the intensity along the z direction for each plane wave composing the field. However, the average intensity $\langle I_0(z,\omega)\rangle$ is constant in any plane (x,y) with constant height $z \geq 0$. Using Eq. (2.5) and substituting Eq. (2.15) into Eq. (2.8), the degree of spatial coherence takes the form

$$\begin{aligned}\mu(\mathbf{r}_1,\mathbf{r}_2,\omega) &= \frac{1}{\sqrt{\langle I_e(z_1,\omega)\rangle \langle I_e(z_2,\omega)\rangle}} \iint_{-\infty}^{\infty} \langle I_a(\overline{p},\overline{q};\omega)\rangle \exp\left[-\gamma(z_1+z_2)\right] \\ &\quad \times \exp\left\{-ik\left[\overline{p}(x_1-x_2)+\overline{q}(y_1-y_2)\right]\right\} d\overline{p}d\overline{q}. \end{aligned} \tag{2.21}$$

It follows from Eq. (2.21) that the degree of spatial coherence $\mu(\mathbf{r}_1,\mathbf{r}_2,\omega)$ is not homogeneous in the z direction but depends only on the transverse separation $\boldsymbol{\Delta\rho} = \mathbf{r}_{\perp 1} - \mathbf{r}_{\perp 2}$ with $\mathbf{r}_\perp$ being the projection of $\mathbf{r}$ onto the (x,y) plane. Fields with such degree of coherence can be called transversely quasi-homogeneous and their cross-spectral density is expressed as

$$W(\mathbf{r}_1,\mathbf{r}_2,\omega) = \sqrt{\langle I_e(z_1,\omega)\rangle \langle I_e(z_2,\omega)\rangle}\,\mu(\boldsymbol{\Delta\rho},z_1,z_2,\omega). \tag{2.22}$$

By considering an evanescent field with a constant average intensity $\langle I_e(\omega)\rangle$ in the plane $(x,y,z=0)$, we showed that the cross-spectral density is invariant transversely but depends on the vectors positions along the z axis. However, since $\langle I_e(z,\omega)\rangle$ decays exponentially, the extend of cross-spectral density along the direction z is limited to a fraction of the wavelength, which essentially makes $W(\mathbf{r}_1,\mathbf{r}_2,\omega)$ a transverse or two dimensional quantity.

In order to obtain a scattering process depending only on the spatial coherence properties of the field, we have considered an average intensity constant at least in the plane $(x,y,z=0)$. From this assumption, we have demonstrated that the field is composed of uncorrelated plane waves and is quasi-homogeneous for propagating waves and transversely quasi-homogeneous

for evanescent waves. This demonstration generalizes to uniform-intensity fields the conclusions drawn in reference [30] for the case of uniform-intensity and Schell-model fields. In the next section, we will show how the spatial coherence properties of the field affects the scattering process.

2.2 Scattering of partially coherent fields in random media

2.2.1 Scalar scattering theory

Let us consider a wave incident upon an object occupying a finite domain D. The medium is considered linear and is described by a dielectric constant ε and a magnetic permeability μ with local and instantaneous response in the spectral range considered. The electric and magnetic components of the field obey the wave equation

$$\bigtriangledown^2 p(\mathbf{r},t) - \frac{n^2(\mathbf{r})}{c^2}\partial_{tt} p(\mathbf{r},t) = Q(\mathbf{r},t), \tag{2.23}$$

where $n(\mathbf{r}) = \sqrt{\varepsilon(\mathbf{r})\,\mu(\mathbf{r})}$ is the refractive index, p represents either the electric or magnetic field and Q is a source term assumed external and independent from the medium. We consider both a monochromatic wave $p(\mathbf{r},t) = u(\mathbf{r})\exp(-i\omega t)$ of frequency ω and a monochromatic source $Q(\mathbf{r},t) = q(\mathbf{r})\exp(-i\omega t)$, thus Eq. (2.23) becomes

$$\bigtriangledown^2 u(\mathbf{r}) + k_0^2\left[1 + 4\pi\eta(\mathbf{r})\right] u(\mathbf{r}) = q(\mathbf{r}), \tag{2.24}$$

with k_0 being the wave number and $\eta = (n^2 - 1)/4\pi$ being the dielectric susceptibility.

Equation (2.24) describes the propagation of a partially coherent wave characterized by the random variable u in a scattering medium defined by the random variable η. The source term q generating the field incident onto the medium is also considered to be a random variable. In general, solving Eq. (2.24) is a complicated task and one has to perform some approximations in order to obtain a solution in terms of the first and second moments of the field.

Let's consider the operator form of the field equation (2.24):

$$\widehat{L}u \equiv \left(\widehat{L}_0 - \widehat{V}\right) u = q, \tag{2.25}$$

where $\widehat{L}_0 = \bigtriangledown^2 + k_0^2$ is the free-space propagator and $\widehat{V}$ is a random operator describing inhomogeneities in the medium. The operator $\widehat{V}$ acts on the field as

$$\widehat{V}u\left(\mathbf{r}\right) = \int_D V\left(\mathbf{r},\mathbf{r}'\right) u\left(\mathbf{r}'\right) d^3\mathbf{r}' = -k_0^2 4\pi\eta\left(\mathbf{r}\right) u\left(\mathbf{r}\right), \tag{2.26}$$

where the kernel of $\widehat{V}$ is defined as $V\left(\mathbf{r},\mathbf{r}'\right) = -k_0^2 4\pi\eta\left(\mathbf{r}\right)\delta\left(\mathbf{r},\mathbf{r}'\right)$. The inverse of the operator $\widehat{L}_0$ is represented by the free-space Green operator $\widehat{L}_0^{-1} = \widehat{G}_0$, with the nucleus of $\widehat{G}_0$ given by

$$G_0\left(\mathbf{r},\mathbf{r}'\right) = G_0\left(\mathbf{r}-\mathbf{r}'\right) = \frac{\exp\left(ik_0\left|\mathbf{r}-\mathbf{r}'\right|\right)}{\left|\mathbf{r}-\mathbf{r}'\right|}. \tag{2.27}$$

The general solution of the scattering problem defined by Eq. (2.25) is obtained from the unknown Green's operator $\widehat{L}^{-1} = \widehat{G}$ so that the total field can be expressed as

$$u = \widehat{G}q. \tag{2.28}$$

Inserting Eq. (2.28) into Eq. (2.25), multiplying both sides by $\widehat{G}_0$ and diving by q, we obtain the following relation for the random media propagator $\widehat{G}$:

$$\widehat{G} = \widehat{G}_0 + \widehat{G}_0 \widehat{V} \widehat{G}. \tag{2.29}$$

According to Eq. (2.29), the propagation of the field characterized by the propagator $\widehat{G}$ is composed of a free propagation $\widehat{G}_0$ in a medium without inhomogeneities and a scattering part corresponding to $\widehat{G}_0 \widehat{V} \widehat{G}$. It follows from Eqs. (2.28) and (2.29) that the total field u becomes

$$u = \widehat{G}_0 q + \widehat{G}_0 \widehat{V} u, \tag{2.30}$$

where $\widehat{G}_0 q = u^i$ relates to the incident wave and $\widehat{G}_0 \widehat{V} u = u^s$ corresponds to the scattered wave, which can also be written in the integral form [31]

$$u^s(\mathbf{r}) = k^2 \int_D \eta(\mathbf{r}') \, u(\mathbf{r}') \, G_0(\mathbf{r} - \mathbf{r}') \, d^3\mathbf{r}'. \tag{2.31}$$

No general solution exists for the integral equation (2.31) or the operator $\widehat{G}$. However, depending on the type of scattering regime considered, certain assumptions can be made in order to deduce an approximate expression for the scattered field.

2.2.2 Perturbation theory and the first-order Born approximation

In order to evaluate the operator $\widehat{G}$, we consider the following series expansion in powers of $\widehat{V}$ [12] obtained by iterating Eq. (2.29)

$$\widehat{G} = \widehat{G}_0 + \widehat{G}_0 \widehat{V} \widehat{G}_0 + \widehat{G}_0 \widehat{V} \widehat{G}_0 \widehat{V} \widehat{G}_0 + ... = \sum_{n=0}^{\infty} \widehat{G}_0 \left(\widehat{V} \widehat{G}_0 \right)^n. \tag{2.32}$$

The series expansion method assumes that $\widehat{V}$ describes a small variation of the refractive index in the medium and, therefore, Eq. (2.32) is understood as a perturbation series. The first term of the series (2.32) relates to propagation of the field in the absence of inhomogeneities, the second term $n = 1$ corresponds to the incident field scattered only one time, the third term $n = 2$ describes double scattering, and so on for larger n values. Solving the scattering problem becomes increasingly complex as more and more terms are retained in the series (2.32). The simplest approximation considers only single scattering by keeping the first two terms in Eq. (2.32):

$$\widehat{G} \approx \widehat{G}_0 + \widehat{G}_0 \widehat{V} \widehat{G}_0. \tag{2.33}$$

This last expansion is known as the first-order Born approximation and the scattered field takes the integral form

$$u^s(\mathbf{r}) = k^2 \int_D \eta(\mathbf{r}')\, u^i(\mathbf{r}')\, G_0(\mathbf{r} - \mathbf{r}')\, d^3\mathbf{r}'. \tag{2.34}$$

Comparing the scattered field expressions in Eq. (2.31) and Eq. (2.34), we notice that the total field u has been replaced by the incident field u^i. This approximation is valid when the scattering is sufficiently weak in the sense that the incident field is not perturbed by the medium and it dominates the scattered field. Using the fact that u^i and η are independent random processes in Eq. (2.34), the second moment of the scattered field takes the form [32]

$$W^{(s)}(\mathbf{r}_1, \mathbf{r}_2) = k^4 \iint_D C(\mathbf{r}, \mathbf{r}') W^{(i)}(\mathbf{r}, \mathbf{r}')\, G_0^*(\mathbf{r}_1 - \mathbf{r})\, G_0(\mathbf{r}_2 - \mathbf{r}')\, d^3\mathbf{r} d^3\mathbf{r}', \tag{2.35}$$

where $W^{(i)}(\mathbf{r}, \mathbf{r}') = \langle u^{i*}(\mathbf{r})\, u^{i}(\mathbf{r}')\rangle$ is the incident cross-spectral density and C is the second-order moment of η:

$$C(\mathbf{r}_1, \mathbf{r}_2) = \langle \eta^*(\mathbf{r}_1)\, \eta(\mathbf{r}_2)\rangle\,. \tag{2.36}$$

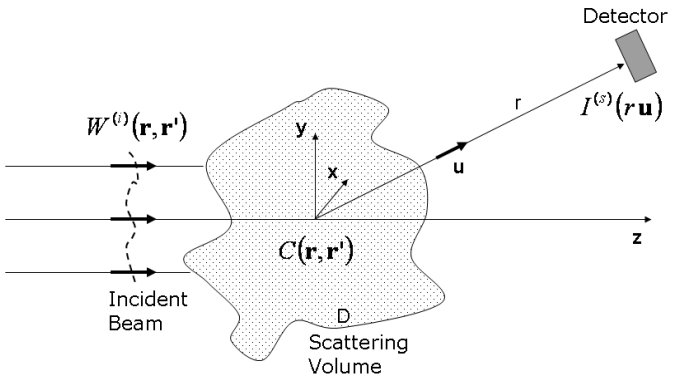

Figure 2.1: Typical scattering experiment configuration.

Equation (2.35) expresses the cross-spectral density of the scattered field at any two points $\mathbf{r}_1$ and $\mathbf{r}_2$. Although $W^{(s)}(\mathbf{r}_1, \mathbf{r}_2)$ can be determined directly [33, 34], its measurement requires a complicated detection system. In a typical experiment, as represented in Fig. 2.1, the scattered intensity is easily accessed at a distance r in the far zone and along a direction given by the unit vector $\mathbf{u}$. Under these conditions, the asymptotic approximation for the Green's function

$$G_0(r\mathbf{u} - \mathbf{r}') = \frac{\exp(ikr)}{r} \exp(-ik\mathbf{u}\cdot\mathbf{r}') \tag{2.37}$$

can be used. Considering Eqs. (2.35) through (2.37), the scattered intensity $I^{(s)}(r\mathbf{u}) \equiv W^{(s)}(r\mathbf{u}, r\mathbf{u})$ in the far zone at a distance r and in the direction $\mathbf{u}$ becomes

$$I^{(s)}(r\mathbf{u}) = \frac{k^4}{r^2}\iint_D C(\mathbf{r},\mathbf{r}')W^{(i)}(\mathbf{r},\mathbf{r}')\exp\left[ik\mathbf{u}\cdot\Delta\mathbf{r}'\right]d^3\mathbf{r}d^3\mathbf{r}', \tag{2.38}$$

where $\Delta\mathbf{r} = \mathbf{r} - \mathbf{r}'$.

Equation (2.38) constitutes the basis for tomographic procedures when both the incident field and the scattering medium are fluctuating. Because the dimensionality of the measured cross-spectral density is smaller than that of the unknown second-order moment C, the problem was shown to be in general underdetermined unless the random object is quasi-homogeneous as we will see in Chapter 4. Even under these conditions, the measurement procedure is quite challenging since the detection system needs access to a wide range of scattering angles in order to provide sufficient data for a robust inversion process [3]. It has been proposed [4] that one can obtain C by taking a fully coherent incident plane wave and then measuring the cross-spectral density of the scattered field in certain planes and for different angles of illumination. Inspecting further Eq. (2.38), one can immediately observe that another possibility exists to obtain the correlation function C. Instead of determining the scattered intensity at different angles, one can measure the intensity scattered in a single direction while varying the coherence properties of the incident field, which are described by $W^{(i)}$. This represents the basis of the variable coherence tomography technique as it will be discussed in details in Chapters 4 and 6.

2.2.3 Multiple scattering and the field moments

By retaining the first three terms in the series expansion (2.32), the scattered field can be computed taking into account single and double scattering events. However the problem becomes practically impossible for $n \geq 3$. Instead of estimating the scattered field by means of a power expansion like in Eq. (2.32), one can consider the solution for the moments of the field. In this approach, perturbation theory is used to evaluate the effective medium's parameters without assuming a small scattered field [12].

The first moment or the average of the field satisfies the Dyson equation [12] obtained by ensemble averaging of Eq. (2.25)

$$\widehat{D}\,\langle u\rangle = \left(\widehat{L}_0 - \widehat{V}_{eff}\right)\langle u\rangle = \langle q\rangle\,. \tag{2.39}$$

In Eq. (2.39), $\widehat{D}$ is the Dyson operator and $\widehat{V}_{eff}$ is the mass operator or operator of effective medium's inhomogeneity, defined as $\left\langle \widehat{V}u \right\rangle = \widehat{V}_{eff}\,\langle u\rangle$. The mean Green's function $\left\langle \widehat{G} \right\rangle$ in the scattering medium satisfies $\widehat{D}\left\langle \widehat{G} \right\rangle = \widehat{1}$ so that the average of the field is given by the relation $\langle u\rangle = \left\langle \widehat{G} \right\rangle \langle q\rangle$. The mean propagator $\left\langle \widehat{G} \right\rangle$ depends on the moments of the random operator $\widehat{V}$, which are usually expanded in a sum of cumulants of $\widehat{V}$, also called correlation functions [35]. Calculating $\langle u\rangle$ reduces to the evaluation of the cumulant functions which measure the statistical coupling between the different inhomogeneities composing the medium.

In order to study the light scattered by a random medium, one needs to consider the equation for the second moment of the field, or cross-spectral density $W(\mathbf{r}_1, \mathbf{r}_2)$, known as

the Bethe-Salpeter equation [12]

$$\left(\widehat{D}_1^*\widehat{D}_2 - \widehat{K}_{12}\right)\langle u_1^* u_2\rangle = \langle q_1^* q_2\rangle\,, \tag{2.40}$$

where we have used the subscript notation 1 and 2 to signify $\langle u_1^* u_2\rangle = \langle u^*(\mathbf{r}_1)\, u_2(\mathbf{r}_2)\rangle$. The operator $\widehat{D}_i$ acts only on the variable u_i whereas $\widehat{K}_{12}$ acts on both variables u_1 and u_2. The intensity operator $\widehat{K}_{12}$ relates to the inhomogeneities of the medium acting on the correlation of the field. The solution of Eq. (2.40) is given by the average operator $\left\langle \widehat{G}_1^*\widehat{G}_2\right\rangle$ describing the propagation of the cross-spectral density in the inhomogeneous medium, where $\widehat{G}_1$ and $\widehat{G}_2$ are the random propagators of the fields u_1 and u_2 in the inhomogeneous medium, respectively. From Eq. (2.40), $\left\langle \widehat{G}_1^*\widehat{G}_2\right\rangle$ satisfies a recurrence relation similar to Eq. (2.29), which, by iteration, can be expressed as a series expansion similar to Eq. (2.32)

$$\begin{aligned}\left\langle \widehat{G}_1^*\widehat{G}_2\right\rangle &= \left\langle \widehat{G}_1^*\right\rangle\left\langle \widehat{G}_2\right\rangle + \left\langle \widehat{G}_1^*\right\rangle\left\langle \widehat{G}_2\right\rangle \widehat{K}_{12}\left\langle \widehat{G}_1^*\right\rangle\left\langle \widehat{G}_2\right\rangle \\ &\quad + \left\langle \widehat{G}_1^*\right\rangle\left\langle \widehat{G}_2\right\rangle \widehat{K}_{12}\left\langle \widehat{G}_1^*\right\rangle\left\langle \widehat{G}_2\right\rangle \widehat{K}_{12}\left\langle \widehat{G}_1^*\right\rangle\left\langle \widehat{G}_2\right\rangle + \ldots\end{aligned} \tag{2.41}$$

According to Eq. (2.41), the propagation of the coherence function can be seen as a succession of independent propagations $\left\langle \widehat{G}_1^*\right\rangle$ and $\left\langle \widehat{G}_2\right\rangle$ of the fields in an effective medium followed by a scattering event characterized by $\widehat{K}_{12}$, which affects the correlation between u_1 and u_2.

Unfortunately, the series (2.41) was shown to be divergent [35]. Indeed, as the number of scatterer increases in the expansion of $\left\langle \widehat{G}_1^*\widehat{G}_2\right\rangle$, the number of possibilities for the statistical coupling between scatterers increases very rapidly. A useful approximation considers keeping only the first order cumulants when calculating the moments of the operators $\widehat{V}_{eff}$ and $\widehat{K}_{12}$. In this, so called, single-group approximation, the operators $\widehat{V}_{eff}^{1gr}$ and $\widehat{K}_{12}^{1gr}$ describe indepen-

dent effective inhomogeneities characterized by dimensions on the order of the correlation diameter l_c of the medium's inhomogeneities. In order for the single-group approximation to be applicable, the mean scattering free path length l_s must be much larger than l_c and the radiation's wavelength λ. It follows that the scattering centers can be seen in the far-field from one another. If the random medium obeys Gaussian statistic, the single-group approximation is know as the Bourret approximation for $\widehat{V}_{eff}^{1gr}$ and the ladder approximation for $\widehat{K}_{12}^{1gr}$.

Furthermore, considering a statistically uniform and stationary scattering medium, the kernels of the operators of effective inhomogeneities $\widehat{V}_{eff}^{1gr}$ and $\widehat{K}_{12}^{1gr}$ can be expressed as

$$\begin{aligned} V_{eff}^{1gr}\left(\mathbf{r}_1,\mathbf{r}_2\right) &= V_{eff}^{1gr}\left(\Delta\mathbf{r}\right), \\ K_{12}^{1gr}\left(\mathbf{r}_1,\mathbf{r}_1';\mathbf{r}_2,\mathbf{r}_2'\right) &= K_{12}^{1gr}\left(\mathbf{R}-\mathbf{R}',\Delta\mathbf{r},\Delta\mathbf{r}'\right), \end{aligned} \tag{2.42}$$

where $\Delta\mathbf{r}=\mathbf{r}_1-\mathbf{r}_2$ and $\Delta\mathbf{r}'=\mathbf{r}_1'-\mathbf{r}_2'$ are the coordinate differences and $\mathbf{R}=\left(\mathbf{r}_1+\mathbf{r}_2\right)/2$ and $\mathbf{R}'=\left(\mathbf{r}_1'+\mathbf{r}_2'\right)/2$ are the average positions. Both functions $V_{eff}^{1gr}\left(\Delta\mathbf{r}\right)$ and $K_{12}^{1gr}\left(\mathbf{R}-\mathbf{R}',\Delta\mathbf{r},\Delta\mathbf{r}'\right)$ vanish when the separations $\Delta\mathbf{r}$ and $\Delta\mathbf{r}'$ exceeds the coherence length l_c. This quasi-uniform assumption is one of the necessary conditions that will allow us to treat the propagation of a partially coherent beam in a multiple scattering medium in terms of the radiative transfer equation.

2.2.4 The radiative transfer equation

Bethe-Salpeter equation (2.40) for the second-order moment of the field is a rigorous integral equation whose kernel is difficult to compute explicitly and a general solution is unavailable at present. However, it was demonstrated that using the one group approximation, and under the condition that the extinction length is much larger than the wavelength, this equation simplifies and leads to an expression equivalent to the radiative transport equation [12].

The assumption of statistical uniformity of the medium, along with the approximate expressions (2.42) of the kernels of $\widehat{V}_{eff}^{1gr}$ and $\widehat{K}_{12}^{1gr}$, implies that the second moment $\langle u^*(\mathbf{r}_1)\, u_2(\mathbf{r}_2)\rangle = W(\mathbf{r}_1, \mathbf{r}_2)$ satisfies the inequality [12]

$$\left|\partial_{\mathbf{R}} W\left(\mathbf{R}+\frac{\Delta\mathbf{r}}{2}, \mathbf{R}-\frac{\Delta\mathbf{r}}{2}\right)\right| \ll \left|\partial_{\Delta\mathbf{r}} W\left(\mathbf{R}+\frac{\Delta\mathbf{r}}{2}, \mathbf{R}-\frac{\Delta\mathbf{r}}{2}\right)\right|. \tag{2.43}$$

Equation (2.43) characterizes a quasi-homogeneous fields and signifies that $W(\mathbf{r}_1, \mathbf{r}_2)$ varies much faster as a function of the coordinate difference $\Delta\mathbf{r} = \mathbf{r}_1 - \mathbf{r}_2$ than as a function of the average position $\mathbf{R} = (\mathbf{r}_1 + \mathbf{r}_2)/2$. To a good approximation, it follows that the cross-spectral density may be expressed in the form [26]

$$W\left(\mathbf{R}+\frac{\Delta\mathbf{r}}{2}, \mathbf{R}-\frac{\Delta\mathbf{r}}{2}\right) = I(\mathbf{R})\, \mu(\Delta\mathbf{r}), \tag{2.44}$$

where $I(\mathbf{R})$ is the intensity at position $\mathbf{R}$ and μ is the degree of spatial coherence. Note that the expression (2.44) of the cross-spectral density inside the scattering medium is similar to the form of the incident cross-spectral density given in Eq. (2.18). Assuming $I(\mathbf{R})$ constant

in Eq. (2.44) leads to a scattering process dependant only on the spatial coherence properties of the field.

At this point, it is convenient to introduce the Wigner distribution function defined as

$$\mathcal{W}(\mathbf{R},\mathbf{k}) = \iiint W(\mathbf{R}+\frac{\Delta\mathbf{r}}{2},\mathbf{R}-\frac{\Delta\mathbf{r}}{2})\exp(-i\mathbf{k}\cdot\Delta\mathbf{r})\frac{d^3\Delta\mathbf{r}}{(2\pi)^3}, \tag{2.45}$$

and which corresponds to a local spectrum of quasi-homogeneous radiations. In addition to naturally include the coherence properties of the field, the Wigner distribution function has the advantage of relating directly to measurable quantities such as spatial or angular intensities. Using the one group approximation of the Dyson equation (2.39) and the Bethe-Salpeter equation (2.40) along with the quasi-uniform assumptions for the operators $\widehat{V}_{eff}^{1gr}$ and $\widehat{K}_{12}^{1gr}$ in Eq. (2.42) and the field in (2.43), it has been shown that the Wigner distribution function verifies the radiative transfer equation (RTE) , which, in the steady state, can be expressed as [12]

$$\frac{\mathbf{k}}{|k|}\cdot\bigtriangledown_{\mathbf{R}}\mathcal{W}(\mathbf{R},\mathbf{k}) = -(\mu_a+\mu_s)\mathcal{W}(\mathbf{R},\mathbf{k}) + \frac{\mu_s}{4\pi}\int_{4\pi} p(\mathbf{k},\mathbf{k}')\mathcal{W}(\mathbf{R},\mathbf{k}')d\Omega_{\mathbf{k}'}. \tag{2.46}$$

In this equation, $p(\mathbf{k},\mathbf{k}')$ is the phase function of one particle. If the medium is composed of non identical particles, then p is a weighted sum of the different phase functions corresponding to each type of particle. The scattering and absorption coefficients μ_s and μ_a are associated with the scattering and absorption mean free paths $l_s = \mu_s^{-1}$ and $l_a = \mu_a^{-1}$, respectively. The mean separation l_s between two consecutive and independent scattering events is related to the scattering cross-section σ_s of the particle by the relation

$$l_s = \frac{1}{N\sigma_s}, \tag{2.47}$$

where N is the number density of the scatterers [36].

First introduced in the context of radiophysics, the RTE was initially derived using a phenomenological approach of local radiative energy balance [37]. In this derivation, the radiance or specific intensity $L(\mathbf{r}, \mathbf{u})$ replaces the Wigner distribution function $\mathcal{W}(\mathbf{R}, \mathbf{k})$ in Eq. (2.46). For a time dependant process, the radiometric quantity $L(\mathbf{r}, \mathbf{u}, t)$ represents the power flowing at a time t, in a direction $\mathbf{u}$ within a differential solid angle, through a elementary area located at the position $\mathbf{r}$. Despite the usual understanding of the RTE as a radiometric equation, we have seen that, in the previous two sections, the origin of the RTE from the rigorous equations of the field's moments enables a partially coherent description of the field. The solution of the RTE depends on the boundary conditions, which, apart from the geometry of the sample under test, vary with the coherence properties of the source. As we will see in Chapter 3, it becomes then possible to establish an inversion procedure in a multiple scattering experiment based on using the degree of coherence of the incident field as an adjustable parameter.

2.2.5 The diffusion equation

Except in a very limited number of situations, the radiative transfer equation cannot be solved analytically and one has to resort to elaborate and time consuming computational methods. As we will see in the next chapter, the small angle approximation is a simplification of the RTE which provides fast numerical results valid when a beam propagates in a

turbulent atmosphere or in media composed of large particles. However, this approximation loses its accuracy as the propagation distance increases beyond a certain point where the divergence of the field becomes too large due to multiple scattering. Indeed, depending on the concentration and on the size of the scatterers, there is a propagation distance after which the light forgets the direction of the initial wave and the radiation can then be considered incoherent and nearly isotropic. Under this condition, it becomes convenient to approximate the radiance L by the sum [38]

$$L(\mathbf{r}, \mathbf{u}, t) \approx \Phi(\mathbf{r}, t) + \frac{3}{4\pi}\mathbf{J}(\mathbf{r}, t) \cdot \mathbf{u}, \tag{2.48}$$

where $\Phi(\mathbf{r}, t)$ is the isotropic radiation defined as

$$\Phi(\mathbf{r}, t) = \frac{1}{4\pi}\int_{4\pi} L(\mathbf{r}, \mathbf{u}, t)\, d\Omega, \tag{2.49}$$

and $\mathbf{J}(\mathbf{r}, t)$ accounts for the small anisotropy in the radiance and corresponds to the average flux of scattered energy

$$\mathbf{J}(\mathbf{r}, t) = \int_{4\pi} L(\mathbf{r}, \mathbf{u}, t)\, \mathbf{u} d\Omega. \tag{2.50}$$

Equation (2.48) is a valid approximation provided that the intensity varies slowly in space and time. In this framework, the radiation can only be characterized at long time t, far from both the source and the boundaries of the medium. Moreover, the scattering mean free path l_s needs to be much greater than the absorption length l_a in order to avoid large gradient of intensity and keep the term $\mathbf{J}(\mathbf{r}, t) \cdot \mathbf{u}$ small in comparison to $\Phi(\mathbf{r}, t)$ in Eq. (2.48).

Substituting the Wigner distribution function $\mathcal{W}$ in Eq. (2.46) by the expression (2.48) and performing the integration over the angular space, one obtains the diffusion equation

which, for a time dependent process, gives [38]

$$\frac{1}{c}\frac{\partial\Phi\left(\mathbf{r},t\right)}{\partial t}-D\nabla^{2}\Phi\left(\mathbf{r},t\right)+\mu_{a}\Phi\left(\mathbf{r},t\right)=q\left(\mathbf{r},t\right). \tag{2.51}$$

In Eq. (2.51), c is the speed of light in the medium, $q\left(\mathbf{r},t\right)$ is an isotropic source term and D is the diffusion coefficient defined as

$$D=\frac{1}{3\left[\mu_{a}+\mu_{s}\left(1-g\right)\right]}. \tag{2.52}$$

The coefficient g in Eq. (2.52) measures the anisotropy of the phase function $p\left(\mathbf{u}\cdot\mathbf{u}'\right)$, which is assumed to depend only on the scattering angle $\mathbf{u}\cdot\mathbf{u}'=\cos\left(\theta\right)$ between the incident and scattered fields directions $\mathbf{u}$ and $\mathbf{u}'$, respectively. In average, the cosine of the scattering angle is [36]

$$g=\left\langle \cos\left(\theta\right)\right\rangle =\int_{4\pi}\mathbf{u}\cdot\mathbf{u}'p\left(\mathbf{u}\cdot\mathbf{u}'\right)d\Omega_{\mathbf{u}'}, \tag{2.53}$$

which equals zero for isotropic scattering and approaches one when the scattering is mainly forward.

The length D defined in Eq. (2.52) is proportional to the transport mean free path $l_{t}=3D$, which, in the case of a non absorbing medium, relates to both the scattering mean free path l_{s} and the anisotropy factor g as

$$l_{t}=\frac{l_{s}}{1-g}. \tag{2.54}$$

The parameter l_{t} is the minimum length scale on which the transport of radiation can be described by the diffusion equation. It corresponds to the distance travelled by the wave after which the direction of propagation is randomized.

Contrary to the radiative transfer equation, analytical results can be obtained from the diffusion equation in many practical situations [39]. The validity of this approximation has been tested repeatedly in highly multiple scattering media and it has been successfully applied in biological imaging [5], rheology of complex fluids [40] or in the measurement of optical path-length distribution using low coherence interferometry [8]. The path of a photon in the diffusion approximation is effectively a random walk and, consequently, the propagation of the field can be regarded as an incoherent transport of energy. Even though the diffusion equation ignores the coherence properties of light, its results can be used to interpret several coherent effects as it will be shown in Chapter 5.

CHAPTER 3

TRANSPORT EQUATION OF THE COHERENCE FUNCTION

Although the influence of atmospheric turbulence and aerosol scattering on either spatially fully coherent or fully incoherent beams has been a subject of active research [41, 42, 43], limited experimental data has been produced on the effect of scattering by aerosols and particulates on partially coherent beams (PCB). Previous research in this area focused on describing how the initially infinite spatial coherence is lost through propagation and scattering and indicated that, when coherent waves propagate through turbid media, the wavefront phase uniformly degrades much faster than the wave intensity decays when the propagation distance is increased [44, 45]. Recent works [46, 47, 48] have shown that the divergence of beams propagating through turbulences strongly depends on their initial degree of spatial coherence. It was noted that PCB are relatively less affected by turbulences than fully coherent beams.

In describing the optical properties of particulate media, just a few studies have addressed the influence of spatial coherence on the power of the scattered radiation. Notably, the optical theorem has been generalized to include scattering of a field with any state of coherence [49, 50] and, more recently, the influence of spatial coherence has been studied in the framework of the radiative transfer equation [25]. Scattering experiments have also been conducted to

evaluate the effect of the spatial coherence of an incident Gaussian Schell-model beam on the angular distribution of the scattered intensity [51].

From the results obtained in all these studies, one can conclude that a random scattering potential affects the spatial coherence of an incident field. Consequently, one can, in principle, recover the scattering potential from measurements of spatial coherence properties. As discussed in the previous chapter, the equation of radiation transfer is suitable for describing the propagation of second-order coherence properties of the field through a multiple scattering medium. We will demonstrate that the density and the size of the particles in a random medium can be evaluated from measurements of the angular intensity of the PCB after propagation through the scattering medium. We will also show here that upon propagation through a particulate medium, the PCB have a better stability – in terms of their divergence – than beams which are initially fully spatially coherent. Solving the transport equation in the paraxial approximation is simplified significantly and its solution, written in the formalism of the Wigner distribution function, agrees quantitatively with our experimental data.

3.1 Wigner distribution - Transport equation: the small angle approximation

Let us consider a partially coherent beam propagating along the **z** direction and incident upon a multiple scattering medium confined between the planes $z = 0$ and $z = L$. The field is characterized by the cross-spectral density $W(\mathbf{r}_1, \mathbf{r}_2; z = 0)$, where $\mathbf{r}_1$ and $\mathbf{r}_2$ are two position vectors in the transverse plane $z = 0$. Using Eq. (2.45), the Wigner distribution function $\mathcal{W}(\mathbf{R}, \mathbf{k}_\perp; z)$ of the incident field in a plane z can be expressed as the Fourier transform of the cross-spectral density $W(\mathbf{R} + \Delta\mathbf{r}/2, \mathbf{R} - \Delta\mathbf{r}/2; z)$ relative to $\Delta\mathbf{r}$ [52]:

$$\mathcal{W}(\mathbf{R}, \mathbf{k}_\perp; z) = \frac{1}{(2\pi)^2} \int W(\mathbf{R} + \frac{\Delta\mathbf{r}}{2}, \mathbf{R} - \frac{\Delta\mathbf{r}}{2}; z) \exp(-i\Delta\mathbf{r}.\mathbf{k}_\perp) d^2\Delta\mathbf{r}, \tag{3.1}$$

where $\mathbf{R} = (\mathbf{r}_1 + \mathbf{r}_2)/2$ and $\Delta\mathbf{r} = \mathbf{r}_1 - \mathbf{r}_2$ are the average position and coordinate difference of $\mathbf{r}_1$ and $\mathbf{r}_2$, respectively (see Fig. 3.1). The vector $\mathbf{k}_\perp$ corresponds to the projection onto the (x, y) plane of the wave vector $\mathbf{k}$ associated with the angular spectrum decomposition of the field.

Substituting Eq. (3.1) into Eq. (2.46) and assuming that the scattering is mainly forward, we obtain the small angle approximation of the radiative transfer equation [16, 52, 53, 54]:

$$(c\partial_z + \frac{c}{k}\mathbf{k}_\perp.\bigtriangledown_{\mathbf{R}})\mathcal{W}(\mathbf{R}, \mathbf{k}_\perp; z) = \int d^2\mathbf{k}'_\perp \widetilde{F}(\mathbf{k}_\perp - \mathbf{k}'_\perp)\mathcal{W}(\mathbf{R}, \mathbf{k}'_\perp; z), \tag{3.2}$$

where c is the speed of the wave in the medium characterized by the refractive index n_0 and the kernel $\widetilde{F}$ depends on the propagation parameters describing the energy transport

$$\widetilde{F}(\Delta\mathbf{k}_\perp) = -c\mu_T\delta^2(\Delta\mathbf{k}_\perp) + \frac{cN}{k^2}\frac{d\sigma(\Delta\mathbf{k}_\perp)}{d\Omega}. \tag{3.3}$$

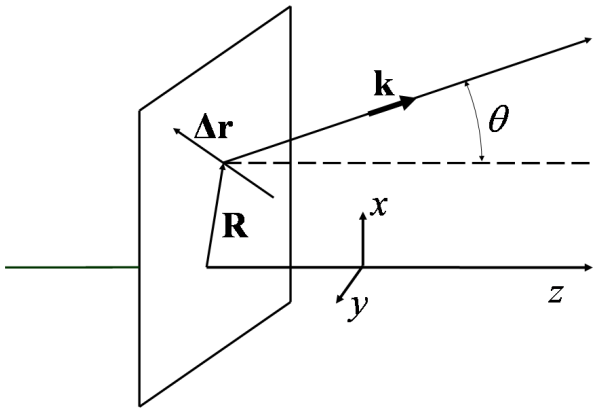

Figure 3.1: Illustration of the notation relating to the propagation of the beam.

In Eq. (3.3), $\mu_T = N(\sigma_A + \sigma_S)$ is the total extinction coefficient, where N is the number density of scattering events, while σ_A and σ_S are the absorption and scattering cross-sections, respectively. The condition of forward scattering in Eq. (3.2) implies that the differential cross section $d\sigma(\Delta\mathbf{k}_\perp)/d\Omega$ of the particles composing the medium is primarily defined in the region $|\Delta\mathbf{k}_\perp| \ll k = 2\pi n_0/\lambda$, where λ relates to the wavelength of the field. The vector $\Delta\mathbf{k}_\perp = \mathbf{k}_\perp - \mathbf{k}'_\perp$ defines the transfer of transverse momentum between the incident and scattered vectors $\mathbf{k}$ and $\mathbf{k}'$, respectively.

On the basis of the solution of the transport equation [45, 53], one can evaluate the mean irradiance distribution $I^{(s)}$ of the light leaving the scattering medium in the direction $\mathbf{k}$

$$I^{(s)}(\mathbf{k}_\perp) = \int \exp\left[-\Gamma\left(\Delta\mathbf{r}, 0, L\right)\right] H(\Delta\mathbf{r}, 0, L) \exp(-i\mathbf{k}_\perp.\Delta\mathbf{r}) d^2\Delta\mathbf{r}, \tag{3.4}$$

with

$$\Gamma(\Delta\mathbf{r}, 0, L) = \frac{L}{c} F(\Delta\mathbf{r}) = \mu_T L - \frac{LN}{k^2} \int \frac{d\sigma(\Delta\mathbf{k}_\perp)}{d\Omega} \exp(i\Delta\mathbf{r}.\Delta\mathbf{k}_\perp) d^2\Delta\mathbf{k}_\perp, \tag{3.5}$$

and

$$H(\Delta\mathbf{r},0,L)=\frac{1}{(2\pi)^2}\int W(\mathbf{R}'+\frac{\Delta\mathbf{r}}{2},\mathbf{R}'-\frac{\Delta\mathbf{r}}{2};0)d^2\mathbf{R}'. \tag{3.6}$$

It has been shown in Ref. [53] Appendix A that a result similar to Eq. (3.4) can be obtain using the extended Huygens-Fresnel principle. A closed-form solution for the Wigner distribution function has been derived in the general case of an ABCD optical system through random media. A comparison between Eqs. (3.4), (3.5) and (3.6) and Ref. [53] shows that the ABCD coefficients for a scattering medium of length L are : $A=1$, $B=L$, $C=0$ and $D=1$. As expected, these coefficients correspond to a translation matrix.

3.2 Divergence of a partially coherent beam

The divergence of the mean irradiance distribution can be expressed as

$$\Delta\theta=\frac{1}{k}\sqrt{\frac{\int\mathbf{k}_\perp^2 I^{(s)}(\mathbf{k}_\perp)d^2\mathbf{k}_\perp}{\int I^{(s)}(\mathbf{k}_\perp)d^2\mathbf{k}_\perp}}. \tag{3.7}$$

Using Eqs. (3.4)-(3.7), the mean square divergence becomes

$$\Delta\theta^2=\frac{1}{k^2S_{out}}\left\{H(0,0,L)\ \bigtriangledown^2_{\Delta\mathbf{r}}\exp\left[-\Gamma(\Delta\mathbf{r},0,L)\right]\big|_{\Delta\mathbf{r}=0}+\exp\left[-\Gamma(0,0,L)\right]\ \bigtriangledown^2_{\Delta\mathbf{r}}H(\Delta\mathbf{r},0,L)\big|_{\Delta\mathbf{r}=0}\right\}, \tag{3.8}$$

where $\bigtriangledown_{\Delta\mathbf{r}}\ldots|_{\Delta\mathbf{r}=0}$ is the gradient relative to the vector $\Delta\mathbf{r}$ taken at the point $\Delta\mathbf{r}=0$ and S_{out}, defined as $S_{out}=\int I^{(s)}(\mathbf{k}_\perp)d^2\mathbf{k}_\perp$, is the total intensity of the beam leaving the scattering medium. The term $H(0,0,L)=\int W(\mathbf{R}',\mathbf{R}',0)d^2\mathbf{R}'/(2\pi)^2$ corresponds to the total intensity S_{in} of the beam entering the scattering medium. Integrating Eq. (3.4) over $\mathbf{k}_\perp$ gives the

classic Beer-Lambert exponential law $S_{out} = S_{in} \exp(-NL\sigma_A)$. Using now the definition of $\Gamma(\Delta\mathbf{r}, 0, L)$ given in Eq. (3.5), we obtain the following expression for the mean square divergence:

$$\Delta\theta^2 = \frac{LN}{k^4} \int \Delta\mathbf{k}_\perp^2 \frac{d\sigma(\Delta\mathbf{k}_\perp)}{d\Omega} d^2\Delta\mathbf{k}_\perp + \frac{1}{k^2 S_{in}} \bigtriangledown^2_{\Delta\mathbf{r}} \left(H(\Delta\mathbf{r}, 0, L)\right)_{\Delta\mathbf{r}=0}. \tag{3.9}$$

This last equation can also be written as

$$\Delta\theta^2 = LN\sigma_S \Delta\theta_S^2 + \Delta\theta_0^2, \tag{3.10}$$

where

$$\Delta\theta_0^2 = \frac{1}{k^2 S_{in}} \bigtriangledown^2_{\Delta\mathbf{r}} H(\Delta\mathbf{r}, 0, L)\big|_{\Delta\mathbf{r}=0}, \tag{3.11}$$

and

$$\Delta\theta_S^2 = \frac{\int \Delta\mathbf{k}_\perp^2 \frac{d\sigma(\Delta\mathbf{k}_\perp)}{d\Omega} d^2\Delta\mathbf{k}_\perp}{k^4 \int \frac{d\sigma(\Delta\mathbf{k}_\perp)}{d\Omega} d^2\Delta\mathbf{k}_\perp} = \frac{\int \Delta\mathbf{k}_\perp^2 \frac{d\sigma(\Delta\mathbf{k}_\perp)}{d\Omega} d^2\Delta\mathbf{k}_\perp}{k^4 \sigma_S}. \tag{3.12}$$

The term $\Delta\theta_S^2$ on the right hand side of Eq. (3.10) includes only the properties of the scattering medium and it corresponds to the mean square divergence of the scattering function. The second term, $\Delta\theta_0^2$, represents the mean square divergence of the incident PCB. Equation (3.10) is similar to Eq. (20a) in Ref. [47] where the divergence of a PCB was derived in the case of propagation through turbulent media. In that case, the spectral density of the refractive index fluctuation is replaced by the scattering function $d\sigma(\Delta\mathbf{k}_\perp)/d\Omega$. Note that the term $LN\sigma_S$ equals the average number of scattering events, which means that the medium is equivalent to a succession of layers [55], each one of them adding $\Delta\theta_S^2$ to the mean square divergence.

We are interested in the variation of the angular spreading of a beam which propagates through a random scattering medium. Therefore, we consider the ratio $\mathcal{D}$ between the rms divergence of the beam leaving the random medium and the beam entering it. This ratio quantifies the angular degradation of the beam when propagating through the medium:

$$\mathcal{D} = \sqrt{\frac{\Delta\theta^2}{\Delta\theta_0^2}} = \sqrt{\frac{LN\sigma_S\Delta\theta_S^2 + \Delta\theta_0^2}{\Delta\theta_0^2}} = \sqrt{1 + \frac{LN\sigma_S\Delta\theta_S^2}{\Delta\theta_0^2}}. \tag{3.13}$$

One can see that $\mathcal{D}$ decreases as the initial divergence $\Delta\theta_0$ increases; consequently it can be of interest to adjust $\Delta\theta_0$ to obtain a desired ratio $\mathcal{D}$. A simple way to adjust $\Delta\theta_0$ is by changing the coherence properties of the beam. It has already been shown (see for example Ref. [46, 47]) that for a Gaussian Schell-model source, with a cross-spectral density in two points $\mathbf{r_1}$ and $\mathbf{r_2}$ of the form

$$W(\mathbf{r}_1, \mathbf{r}_2) = \exp(-\frac{\mathbf{r}_1^2 + \mathbf{r}_2^2}{w_0^2}) \exp(-\frac{|\mathbf{r}_1 - \mathbf{r}_2|^2}{2\sigma_\mu^2}), \tag{3.14}$$

the angular spread is

$$\Delta\theta_0^2 = \frac{2}{k^2}(\frac{1}{\sigma_\mu^2} + \frac{1}{w_0^2}), \tag{3.15}$$

where w_0^2 and σ_μ^2 are the waist of the intensity in the source plane and the variance of the degree of spatial coherence, respectively. One can control in this way the initial divergence by adjusting σ_μ.

3.3 Propagation of a partially coherent beam in a particulate medium

A systematic series of experiments has been performed and compared with the predictions of the model presented in Section 3.1. The experimental setup is schematically depicted in Fig. 3.2. The TM_{00} beam of a cw Ti:Sapphire laser ($\lambda = 800nm$) is focused by the lens L_1 on a rotating diffuser and the spot size can be adjusted by moving the lens L_1 mounted on a translation stage. The light emerging from the rotating diffuser can be regarded as a secondary, spatially incoherent source. Most of the scattered light is collected by a second lens L_2 placed at a focal distance from the diffuser. Therefore, the beam after L_2 is a collimated partially coherent beam with a degree of coherence that can be continuously adjusted by moving the lens L_1. A field aperture placed just in front of the scattering medium creates a beam of $9mm$ in diameter with a constant intensity over the entire aperture. The scattering medium is a cuvette ($L = 10mm$) filled with an aqueous solution of polystyrene microspheres. The beam exiting the scattering medium is then collected by the lens L_3 and a CCD camera placed in the focal plane of this lens records the far-field angular distribution of the beam exciting the random medium.

A typical intensity distribution of the scattered beam that is collected in the focal plane of L_3 is presented in Fig. 3.3. To obtain an average intensity, the exposure time was set to be around 30 seconds, while the scattering solution in the cuvette was sonicated to avoid sedimentation of the particles. From this data, we reconstructed the angular intensity $I^{(s)}(\theta)$

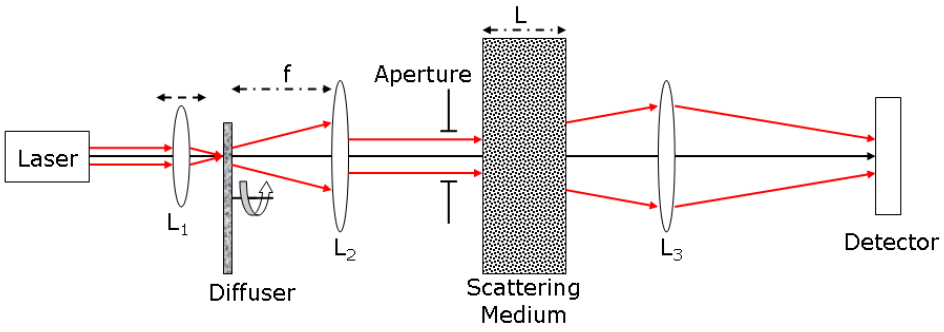

Figure 3.2: Experimental setup used to study the scattering of partially coherent beams.

by expressing the spatial position on the CCD in terms of the angle $\theta = |\mathbf{k}_\perp| / k$ using the value of the focal length of L_3.

In a first round of experiments, the divergence of the input beam was measured as a function of its state of coherence. Note that a direct comparison with the prediction of the model developed in Section 3.1 can be made by simply setting the concentration number density $N = 0$. Because the intensity impinging on the diffuser has a Gaussian profile, according to van Cittert-Zernike theorem, the degree of coherence has also a Gaussian distribution, as the diffuser is placed in the focal plane of L_2. In the plane of the field aperture, the incident beam has a radius $w_0 = 4.5mm$ and its intensity distribution is described by the function Q, defined as $Q(\mathbf{r}) = 1$ for $|\mathbf{r}| \leq w_0$ and equals zero otherwise. The cross-spectral density of the beam impinging on the cuvette has therefore the following form

$$W(\mathbf{r}_1, \mathbf{r}_2) = \sqrt{Q(\mathbf{r}_1) Q(\mathbf{r}_2)} \exp(-\frac{|\mathbf{r}_1 - \mathbf{r}_2|^2}{2\sigma_\mu^2}), \tag{3.16}$$

where σ_μ the variance of the degree of spatial coherence.

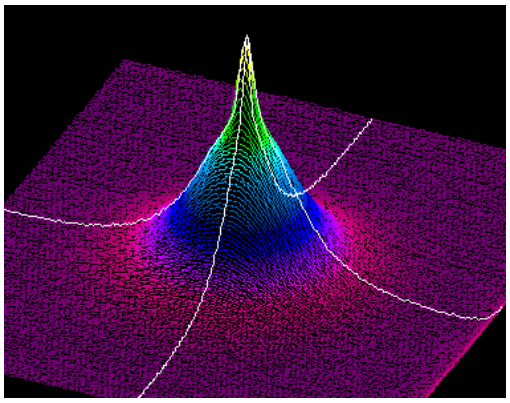

Figure 3.3: Three-dimensional representation of the angular intensity $I^{(s)}(\theta)$ recorded by the CCD detector.

The value of σ_μ changes between $1300\mu m$ and $57\mu m$ when the lens L_1 is translated during the experiment. In Fig. 3.4, the beam divergence is plotted versus the coherence parameter σ_μ^{-2}. The divergence was calculated using Eq. (3.7) and, in order to reduce the effect of the background noise, the intensity signal of the CCD was set to zero for values below 1% of the maximum value. To have a fair comparison with the model, we also set to zero the values of the irradiance given by Eq. (3.4) that are below 1% of the maximum irradiance. This procedure was applied for the calculation of all the divergences.

The experimental σ_μ is calculated as $\sigma_\mu = \lambda f / (\pi w)$, where f is the focal length of the lens L_2, λ is the free space wavelength, and w is the waist of the beam focused on the diffuser. We estimated the waist w by considering a Gaussian beam propagating toward and focused by the lens L_1.

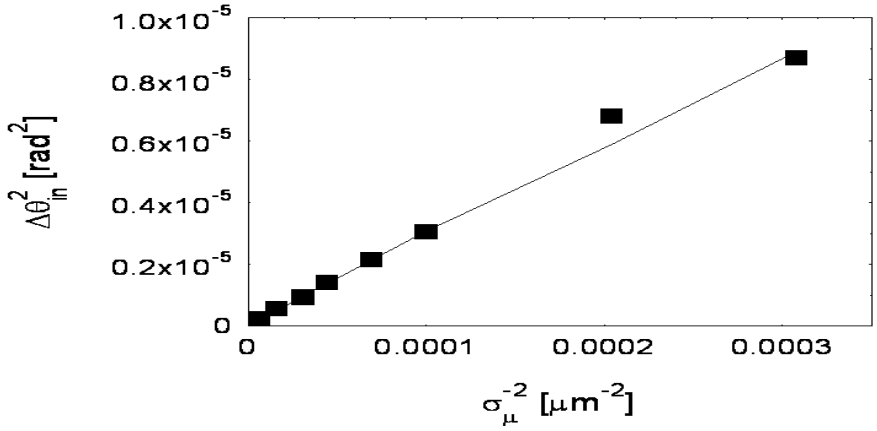

Figure 3.4: Divergence for partially coherent beams with different coherence parameters. The dots are the experimental data and the continuous curve represents the result of calculations based on Eq. (3.2).

A remarkable agreement is obtained between the experimentally measured divergences and the model predictions, proving that the description of the cross-spectral density at the entrance of the random medium is realistic.

Next, the scattering medium (the aqueous solution of polystyrene microspheres) is introduced as shown in Fig. 3.2 and the procedure for measuring the divergence is followed again. In Fig. 3.5, the normalized angular intensity is shown for beams propagating through a water suspension of $280\mu m$ diameter polystyrene microspheres (Duke Scientific Corporation, size distribution $13.5\mu m$, index of refraction $n = 1.59$, and scattering cross section $\sigma_S = 1.24 \times 10^{-7} m^2$). The volume fraction of the suspension was 6.2% corresponding to an average of 6.6 scattering events. The angular intensity was recorded for different values

of the degree of coherence σ_μ in the range of $57\mu m$ to $1300\mu m$. Also shown in Fig. 3.5, is the numerical solution derived from Eq. (3.2) calculated for 6.6 scattering events and for a differential scattering cross-section as predicted by Mie theory for the spheres considered.

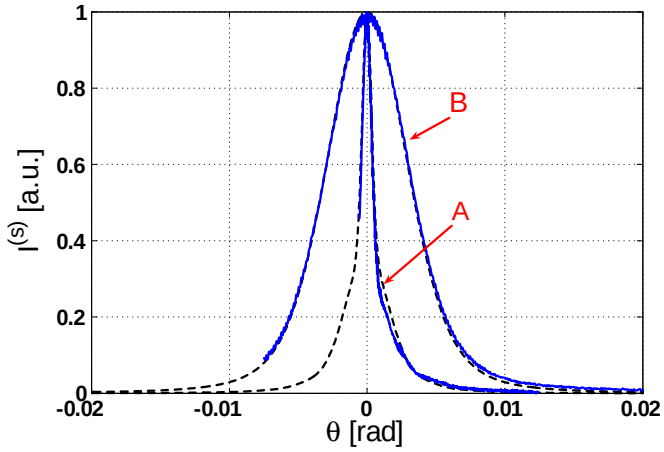

Figure 3.5: Normalized angular scattered intensity for an incident beam with a diameter of 9mm and a coherence parameter $\sigma_\mu = 390\mu m$ (A) and for $\sigma_\mu = 57\mu m$ (B). Solid curves, the experimental results; Dashed curves, the calculations based on Eq. (3.2).

As shown in Fig. 3.5, a good agreement is obtained between the experimental data and the theoretical predictions indicating that the transport equation for the Wigner distribution function is applicable in all cases studied. Knowing the spatial coherence length σ_μ of the incident beam, it is then possible to retrieve both the concentration and the size of the particles by fitting the measured divergence of the output intensity with the mean irradiance distribution $I^{(s)}$ derived form the transport equation. It is interesting to note that, for the results in (B), the spatial coherence length σ_μ was significantly smaller than the size of the particles composing the random medium. In fact, there are several coherence areas within

the projected surface of a scattering sphere but results derived from the Mie scattering theory are still appropriate in the contest of radiative transport equation. On the other hand, for the results in (A) , the coherence area largely exceeds the size of a particle which is in this case practically exposed to a plane wave [50].

The angular degradation ratio $\mathcal{D}$, defined in Eq.(3.13), is plotted in Fig. 3.6 as a function of the coherence parameter σ_μ^{-2} of the initial beam. One can clearly see that the beam with the lowest degree of coherence is the least affected with the smallest $\mathcal{D}$. A better stability of the divergence is therefore obtained in the case of PCB in comparison with the situation where a fully spatially coherent beam is incident on the scattering medium. This corroborate the conclusions stated in Ref. [47], which apply to turbulent media.

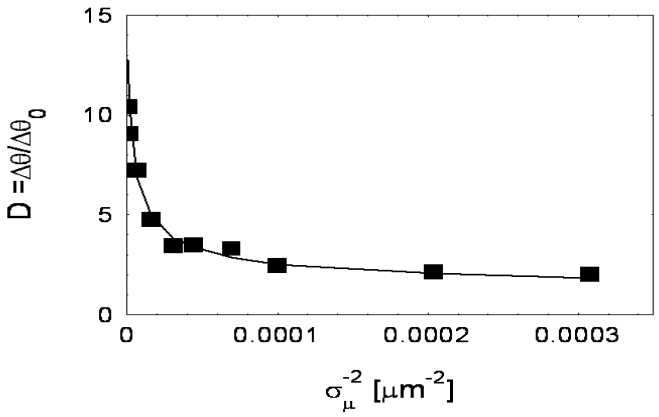

Figure 3.6: The rms angular spread of the beam after the particulate medium relative to its initial value. The coherence length σ_μ of the partially coherent beam ranges from 1.3mm to $57\mu m$.

3.4 Conclusion

The spectral theory of radiative transport in the paraxial approximation makes a good description of the experiment when the rms width σ_μ of the degree of coherence ranges from values larger to smaller than the size of the scatters. Both the concentration and the size of the particles can be determined from fitting the angular output intensity with the solution of the radiative transport equation obtained by using the incident cross-spectral density function. We have found an expression for the rms width of a PCB propagating in a particulate media that is similar to that already suggested for propagation through atmospheric turbulent media. Our results demonstrate that, in the case of particulate media, the increase of divergence relative to the divergence of the initial beam is significantly smaller in the case of beams which are, initially, less spatially coherent. This suggest new possibilities of controlling the divergence of beams propagating through scattering media with inhomogeneous properties and should be of interest for applications including guiding and tracking as well as active remote sensing through long atmospheric paths. Understanding the subtle effects of coherence could also lead to novel approaches for solving inverse problems associated with beams propagation and scattering.

As discussed in Chapter 2, the main approximation, which leads to the radiative transfer equation, assumes that the correlation radius of the medium's fluctuations is on the order of the size of effective inhomogeneities and it is much smaller than the free path length in the medium. Consequently, the radiative transfer formalism can only account for the

short-range correlation lengths related to the size of the particles. In order to estimate the second-order statistical properties of a random scattering potential, a method sensitive to long-range correlations will be presented in the next chapter.

CHAPTER 4

VARIABLE COHERENCE TOMOGRAPHY

The reconstruction of a three-dimensional scattering object is usually done by either computed tomography or diffraction tomography [3]. Traditionally, these methods have been applied to solve inverse problems involving deterministic objects. However, a large number of random media can only be characterized by their statistical properties and, in many applications, the main interest is in finding the pair-correlation function of the scattering potential. Conventionally, the correlation function of the scattering potential can be obtained by using a fully coherent plane wave illuminating with different angles of incidence and measuring the cross-spectral density of the field scattered in two different planes [4]. However, in many practical cases, the cross-spectral density is difficult to evaluate because it requires the use of interferometric methods and direct intensity measurements are preferred.

In this chapter, we describe a different approach where the degree of spatial coherence of a quasi-monochromatic beam is shaped such that the fields in two separate volumes are correlated [15, 56]. The spatial separation between these volumes can be varied continuously in order to induce coherent scattering from different parts of the medium. Using the spatial properties of the incident beam, we propose and demonstrate a tomographic procedure for determining the correlation function of a scattering potential. A notable feature is the simple

detection configuration which only requires to measure the intensity along a single direction of scattering.

4.1 Spatial coherence shaping

Let us consider the experimental setup sketched in Fig. 4.1 where a quasi-monochromatic spatially incoherent source S, placed in the focal plane of a collecting lens L_s, generates a partially coherent beam propagating along the $\mathbf{z}$ axis and incident upon a scattering volume D. The source is considered to be a collection of independent radiative points emitting uniformly in the direction of L_s. As a result, the intensity across the beam is constant and one can consider the incident field to be quasi-homogeneous with a cross-spectral density of the form [27]

$$W^{(i)}\left(\mathbf{r}_1, \mathbf{r}_2\right) = I^{(i)}\left(\mathbf{R}\right) \mu^{(i)}\left(\Delta\mathbf{r}\right), \tag{4.1}$$

where $\Delta\mathbf{r} = \mathbf{r}_1 - \mathbf{r}_2$, $\mathbf{R} = \left(\mathbf{r}_1 + \mathbf{r}_2\right)/2$, $\mu^{(i)}\left(\Delta\mathbf{r}\right)$ is the degree of spatial coherence of the incident beam and $I^{(i)}\left(\mathbf{r}\right)$ is the intensity at position $\mathbf{r}$.

A large class of random media have a degree of spatial correlation $\mu_\eta\left(\mathbf{r}_1, \mathbf{r}_2\right)$ that depends only on the separation $\Delta\mathbf{r} = \mathbf{r}_1 - \mathbf{r}_2$ between the two points P_1 and P_2 (see Fig. 4.1) and not on their average location $\mathbf{R} = \left(\mathbf{r}_1 + \mathbf{r}_2\right)/2$. Such media are quasi-homogeneous and the second moment of the spatial correlation of the complex susceptibility $\eta\left(\mathbf{r}\right)$ is well approximated by

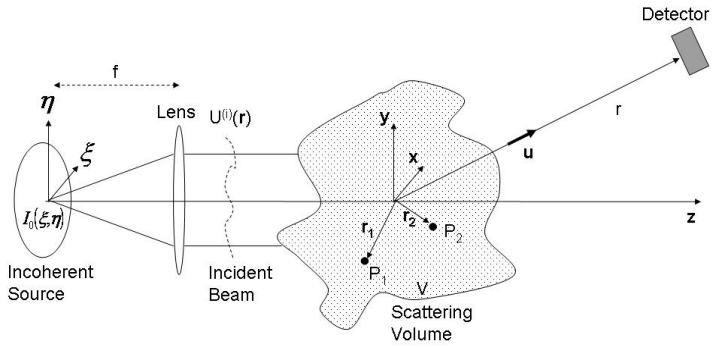

Figure 4.1: Typical scattering configuration for variable coherence tomography.

the expression [57]

$$C\left(\mathbf{r}_1,\mathbf{r}_2\right)=\left\langle \eta^*\left(\mathbf{r}_1\right)\eta\left(\mathbf{r}_2\right)\right\rangle_\eta \approx S_\eta\left(\mathbf{R}\right)\mu_\eta\left(\Delta\mathbf{r}\right), \tag{4.2}$$

where $\langle ... \rangle_\eta$ denotes the ensemble averaging over the realizations of $\eta\left(\mathbf{r}\right)$ and $S_\eta\left(\mathbf{r}\right)=C\left(\mathbf{r},\mathbf{r}\right)$ is the second moment of $\eta\left(\mathbf{r}\right)$.

Substituting Eqs. (4.1) and (4.2) into Eq. (2.38), the expression for the intensity scattered by a weakly scattering medium in a direction $\mathbf{u}$ and at a distance r becomes

$$I^{(s)}(r\mathbf{u})=\frac{k^4}{r^2}\iint_D S_\eta\left(\mathbf{R}\right)\mu_\eta\left(\Delta\mathbf{r}\right)I^{(i)}\left(\mathbf{R}\right)\mu^{(i)}\left(\Delta\mathbf{r}\right)\exp\left[ik\mathbf{u}\cdot\Delta\mathbf{r}\right]d^3\mathbf{r}_1 d^3\mathbf{r}_2. \tag{4.3}$$

Our scope is to obtain μ_η and for this purpose we propose to shape the coherence volume defined by $\mu^{(i)}\left(\Delta\mathbf{r}\right)$ such that the field coherent within a certain volume V_{c1} is correlated with the field in a volume V_{c2} centered at a position $\Delta\mathbf{r}_0$ away from V_{c1}. As a result, fields originating at scattering centers located in V_{c1} interfere with each other and also with the fields generated by scatterers in V_{c2}. Therefore, the interference in the scattered field carries

information about the correlation function of the complex susceptibility. Recently, it has been suggested [15, 56] that $\Delta\mathbf{r}_0$ can take values along the axis of propagation of certain beams such that the field is coherent at a pair of points separated longitudinally. We will now demonstrate that, in general, $\Delta\mathbf{r}_0$ can take any value along or transversely to the propagation axis of specially designated beams.

In order to shape the coherence volume, let us examine the situation where the source S has an intensity distribution $I_0(\xi,\eta)$ at the location defined by ξ and η. Within the paraxial approximation, the degree of spatial coherence [15, 58, 59] of this incident field at two points P_1 and P_2 located at $\mathbf{r}_1$ and $\mathbf{r}_2$ (see Fig. 4.1) is

$$\mu^{(i)}(\Delta\mathbf{r}) = \exp\left[-ik\Delta z\right] \frac{\iint_S I_0(\xi,\eta)\exp\left[i\frac{k}{f_s}\left(\xi\Delta x+\eta\Delta y\right)+i\frac{k\Delta z}{2f_s^2}\left(\xi^2+\eta^2\right)\right]d\xi d\eta}{\iint_S I_0(\xi,\eta)d\xi d\eta}, \quad (4.4)$$

where f_s is the focal length of L_s and Δx, Δy and Δz are the projections of the vector $\Delta\mathbf{r}$ onto the coordinate unit vectors $\mathbf{x}$, $\mathbf{y}$ and $\mathbf{z}$.

To be able to generate a field coherent at a specific pair of points [60], let us consider that the intensity profile in the source plane is similar to a Newton rings pattern (see Fig. 4.2) centered at (x_0, y_0) and extended up to the radius R:

$$I_0(\xi,\eta) = \frac{1}{2}\left(1+m\cos\left[2\pi\frac{(\xi-x_0)^2+(\eta-y_0)^2}{\alpha^2}-\beta\right]\right) Q\left(\sqrt{\xi^2+\eta^2}\right). \quad (4.5)$$

In Eq. (4.5), m is a modulation factor taking values between 0 and 1, R is the radius of the source and the function Q is defined as $Q(x) = 1$ for $x < R$ and equals zero otherwise. The phase of the cosine at x_0 and y_0 is given by β, while the size of the rings is adjusted by the parameter α.

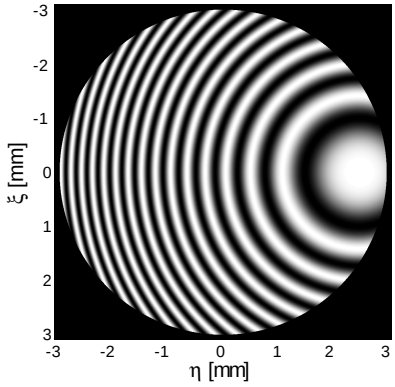

Figure 4.2: Intensity pattern in the plane (ξ, η) of the source.

Substituting Eq. (4.5) into Eq. (4.4), one can show that the degree of spatial coherence $\mu^{(i)}(\Delta\mathbf{r})$ of the incident field is of the form

$$\mu^{(i)}(\Delta\mathbf{r}) = \exp[-ik\Delta z]\, g(\Delta\mathbf{r}) + \frac{m}{2}\exp[i\{\phi(\Delta\mathbf{r}_0) - k\Delta z\}]\, g(\Delta\mathbf{r} + \Delta\mathbf{r}_0) \qquad (4.6)$$
$$+ \frac{m}{2}\exp[-i\{\phi(\Delta\mathbf{r}_0) + k\Delta z\}]\, g(\Delta\mathbf{r} - \Delta\mathbf{r}_0),$$

with the phase parameter $\phi(\Delta\mathbf{r}_0) = 2\pi(x_0^2 + y_0^2)/\alpha^2 - \beta$. The spatial separation vector

$$\Delta\mathbf{r}_0 = \frac{2\lambda f}{\alpha^2}(-x_0\mathbf{x} - y_0\mathbf{y} + f\mathbf{z}) \qquad (4.7)$$

determines the distance between the two separate volumes where the field is correlated.

When there is no intensity modulation across the source, i.e. when the parameter m equals zero in Eq. (4.5), the function g in Eq. (4.6) corresponds to the degree of spatial coherence of the incident beam:

$$g(\Delta\mathbf{r}) = \frac{\iint \frac{1}{2}Q\left(\sqrt{\xi^2+\eta^2}\right)\exp\left[i\frac{k}{f_s}(\xi\Delta x + \eta\Delta y) + i\frac{k\Delta z}{2f_s^2}\left(\xi^2+\eta^2\right)\right]d\xi d\eta}{\iint I_0(\xi,\eta)d\xi d\eta}. \qquad (4.8)$$

A typical degree of spatial coherence $\mu^{(i)}(\Delta\mathbf{r})$ described in Eq. (4.6) is plotted in Fig. 4.3. Note that the field is coherent at a pair of points if their separation is close to zero as described by the main peak in Fig. 4.3, or if their spatial separation is close to $\Delta\mathbf{r}_0$ which corresponds to the position of the smaller peak in Fig. 4.3. Because $\mu^{(i)}(\Delta\mathbf{r})$ is Hermitian, we also have correlation if the points separation is close to $-\Delta\mathbf{r}_0$. The shape of each peak is expressed by the function $g(\Delta\mathbf{r})$ in Eq. (4.8). For transversal coherence, i.e. $\Delta z = 0$, the expression of $g(\Delta\mathbf{r})$ is $J_1(\rho)/\rho$ and its FWHM is approximately $\lambda f/(2R)$. In the case of longitudinal coherence, i.e. $\Delta x = 0$ and $\Delta y = 0$, $g(\Delta\mathbf{r})$ takes the form [15] $\sin(\rho)/\rho$ and its FWHM is approximately $2\lambda f^2/R^2$.

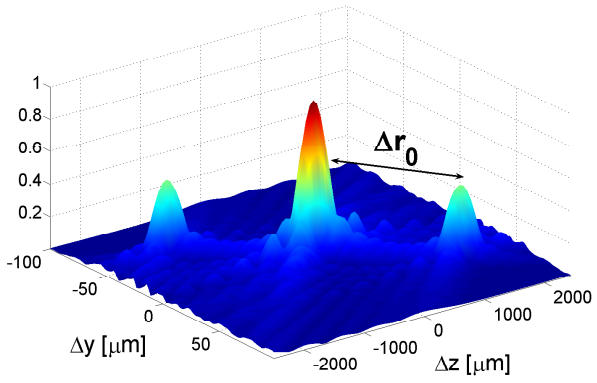

Figure 4.3: Degree of spatial coherence $\mu^{(i)}(\Delta x, \Delta y, \Delta z)$ of the incident field plotted as a function of the two points separation Δy and Δz and for $\Delta x = 0$.

4.2 Variable coherence tomography – Principle

To this point, we have been able to create a field with a spatial degree of coherence composed of two peaks mutually coherent and with an adjustable separation as described in Eq. (4.6) and plotted in Fig. 4.3. One can use now the special form for $\mu^{(i)}$ described in Eq. (4.6) in order to obtain, from Eq. (4.3), a new expression for the scattered intensity. If we consider that the incident beam and the random medium are both quasi-homogeneous, the functions $S_\eta(\mathbf{r})$ and $I^{(i)}(\mathbf{r})$ vary more slowly with $\mathbf{r}$ than μ_η and $\mu^{(i)}$. As a result, one can separate S_η and $I^{(i)}$ from μ_η and $\mu^{(i)}$ in the integration in Eq. (4.3). Then, using Eq. (4.6), one can show that the scattered intensity becomes

$$\begin{aligned} I^{(s)}(r\mathbf{u},\Delta\mathbf{r}_0) = D_I\{ & \int \mu_\eta(\Delta\mathbf{r})\, g(\Delta\mathbf{r}) \exp\left[ik\left(\mathbf{u}-\mathbf{z}\right)\cdot\Delta\mathbf{r}\right] d^3\Delta\mathbf{r} \\ & + \frac{m}{2}\exp\left[i\phi\left(\Delta\mathbf{r}_0\right)\right] \int \mu_\eta(\Delta\mathbf{r})\, g(\Delta\mathbf{r}+\Delta\mathbf{r}_0) \exp\left[ik\left(\mathbf{u}-\mathbf{z}\right)\cdot\Delta\mathbf{r}\right] d^3\Delta\mathbf{r} \\ & + \frac{m}{2}\exp\left[-i\phi\left(\Delta\mathbf{r}_0\right)\right] \int \mu_\eta(\Delta\mathbf{r})\, g(\Delta\mathbf{r}-\Delta\mathbf{r}_0) \exp\left[ik\left(\mathbf{u}-\mathbf{z}\right)\cdot\Delta\mathbf{r}\right] d^3\Delta\mathbf{r}\}, \end{aligned} \tag{4.9}$$

where

$$D_I = \frac{k^4}{r^2}\int_D S_\eta(\mathbf{r}_2')\, I^{(i)}(\mathbf{r}_2')\, d^3\mathbf{r}_2'. \tag{4.10}$$

Using the Hermitian properties of μ_η and g in Eq. (4.9), it follows, after straightforward calculations, that the scattered intensity can be written as

$$\begin{aligned} I^{(s)}(r\mathbf{u},\Delta\mathbf{r}_0) = {} & D_I G(k\mathbf{u},0) \\ & \times\left\{1 + m\left|\frac{G(k\mathbf{u},\Delta\mathbf{r}_0)}{G(k\mathbf{u},0)}\right| \cos\left[k\left(\mathbf{u}-\mathbf{z}\right)\cdot\Delta\mathbf{r}_0 - \phi\left(\Delta\mathbf{r}_0\right) - \phi_G\left(k\mathbf{u},\Delta\mathbf{r}_0\right) + \phi_G\left(k\mathbf{u},0\right)\right]\right\}. \end{aligned} \tag{4.11}$$

In Eq. (4.11), $\phi_G(k\mathbf{u},\Delta\mathbf{r}_0)$ is the argument of the function $G(k\mathbf{u},\Delta\mathbf{r}_0)$ representing the convolution between the two functions $\mu_\eta(\mathbf{r})$ and $g(\mathbf{r})\exp[ik(\mathbf{u}-\mathbf{z})\cdot\mathbf{r}]$:

$$G(k\mathbf{u},\Delta\mathbf{r}_0) = \int \mu_\eta(\mathbf{r}-\Delta\mathbf{r}_0)\, g(\mathbf{r}) \exp[ik(\mathbf{u}-\mathbf{z})\cdot\mathbf{r}]\, d^3\mathbf{r}. \tag{4.12}$$

The expression for the scattered intensity in Eq. (4.11) constitutes our main result. Within the first Born approximation, the incident field induces coherent scattering in the medium for points that are separated by $\Delta\mathbf{r}_0$. Therefore, if the complex susceptibility has a degree of correlation μ_η different from zero at $\Delta\mathbf{r}_0$, the scattered intensity will oscillate depending on the values of $\Delta\mathbf{r}_0$ and the direction $\mathbf{u}$. In an experiment, one can then vary $\Delta\mathbf{r}_0$ and record the scattered intensity $I^{(s)}(r\mathbf{u},\Delta\mathbf{r}_0)$ in a single direction $\mathbf{u}$. From this, $G(k\mathbf{u},\Delta\mathbf{r}_0)$, can be recovered using conventional envelope and phase reconstruction [20]. The degree of spatial correlation of the scattering medium $\mu_\eta(\Delta\mathbf{r}_0)$ is then obtain from Eq. (4.12).

Let us consider the case of a scattering potential of the form

$$\mu_\eta(\mathbf{r}) = \delta(\mathbf{r}) + m_\eta\delta(\mathbf{r}+\Delta\mathbf{r}_{scat}) + m_\eta\delta(\mathbf{r}-\Delta\mathbf{r}_{scat}) \tag{4.13}$$

where $0 \leq m_\eta \leq 1$ is the amplitude of the correlation at $\mathbf{r} = \pm\boldsymbol{\Delta}\mathbf{r}_{scat}$ and $\delta(\mathbf{r})$ is the delta function. Using Eq. (4.13) and for the case $\Delta\mathbf{r}_0 \neq 0$, Eq. (4.12) becomes

$$\begin{aligned} G(k\mathbf{u},\Delta\mathbf{r}_0) = {} & g(\Delta\mathbf{r}_0)\exp[ik(\mathbf{u}-\mathbf{z})\cdot\Delta\mathbf{r}_0] \\ & + m_\eta g(\Delta\mathbf{r}_0-\Delta\mathbf{r}_{scat})\exp[ik(\mathbf{u}-\mathbf{z})\cdot(\Delta\mathbf{r}_0-\Delta\mathbf{r}_{scat})] \\ & + m_\eta g(\Delta\mathbf{r}_0+\Delta\mathbf{r}_{scat})\exp[ik(\mathbf{u}-\mathbf{z})\cdot(\Delta\mathbf{r}_0+\Delta\mathbf{r}_{scat})]. \end{aligned} \tag{4.14}$$

When discussing the distance between the two coherence volumes where the field was correlated, we implicitly assumed that the volumes were distinct meaning that the width of g is small compared to the distance $|\Delta\mathbf{r}_0|$, i.e. $g(\Delta\mathbf{r}_0) \simeq 0$. If the dimensions of these volumes are too large, the volumes overlap and cannot be differentiated anymore. We will therefore assume in the following that $\Delta\mathbf{r}_0$ is always large enough so that we can neglect $g(\Delta\mathbf{r}_0) \simeq 0$ in Eq. (4.14). Since the degree of coherence is Hermitian, i.e. $\mu_\eta(\Delta\mathbf{r}_{scat}) = \mu_\eta^*(-\Delta\mathbf{r}_{scat})$, in order to avoid the ambiguity on the sign of $\Delta\mathbf{r}_{scat}$, we set the convention that $\Delta\mathbf{r}_{scat} \cdot \mathbf{z}$ and $\Delta\mathbf{r}_0 \cdot \mathbf{z}$ are both greater than zero. It also follows that one cannot have $\Delta\mathbf{r}_0 + \Delta\mathbf{r}_{scat} = \mathbf{0}$ meaning that $g(\Delta\mathbf{r}_0 + \Delta\mathbf{r}_{scat}) \simeq 0$ in Eq. (4.14) which now can be written as

$$G(k\mathbf{u},\Delta\mathbf{r}_0) \simeq m_\eta g(\Delta\mathbf{r}_0 - \Delta\mathbf{r}_{scat}) \exp\left[ik(\mathbf{u}-\mathbf{z}) \cdot (\Delta\mathbf{r}_0 - \Delta\mathbf{r}_{scat})\right]. \tag{4.15}$$

If $\Delta\mathbf{r}_0 = 0$, it follows from Eqs. (4.12) and (4.13) that $G(k\mathbf{u},0) = g(0)$. According to the expression of the degree of spatial coherence in Eq. (4.6) and using the approximation $g(\Delta\mathbf{r}_0) \simeq 0$, we obtain $\mu^{(i)}(0) = g(0)$. Since, by definition, $\mu^{(i)}(0) = 1$, it follows that $g(0) = 1$. Then, using Eq. (4.15), one can show that the scattered intensity in Eq. (4.11) becomes

$$I^{(s)}(r\mathbf{u},\Delta\mathbf{r}_0) = D_I\{1+ \tag{4.16}$$
$$m_\eta m\,|g(\Delta\mathbf{r}_0 - \Delta\mathbf{r}_{scat})| \cos\left[k(\mathbf{u}-\mathbf{z}) \cdot \Delta\mathbf{r}_0 - \phi(\Delta\mathbf{r}_0) - \phi_G(k\mathbf{u},\Delta\mathbf{r}_0) + \phi_G(k\mathbf{u},0)\right]\}.$$

One can clearly see now that the envelope of the oscillations in $I^{(s)}(r\mathbf{u},\Delta\mathbf{r}_0)$ has an amplitude directly proportional to the modulus $|g(\Delta\mathbf{r}_0 - \Delta\mathbf{r}_{scat})|$. Since $|g(0)| = 1$, the maximum amplitude of the oscillations is $m_\eta m$.

4.3 Experimental results

In a proof-of-concept experiment, an intensity distribution was generated over a spatially incoherent source in order to create a partially coherent beam with a degree of spatial coherence as described in Eq. (4.6). This beam illuminated a scattering medium with a scattering potential correlation $\mu_\eta(\mathbf{r})$ of the type given by Eq. (4.13). Measuring the scattered intensity along one direction, we were then able to reconstruct the degree of spatial correlation $\mu_\eta(\mathbf{r})$ following the procedure outlined in Section 4.2.

4.3.1 Construction of a correlated scattering system

In order to create a scattering medium with a degree of spatial correlation $\mu_\eta(\mathbf{r})$ of the form given in Eq. (4.13), we used a thin glass plate GP (see Fig. 4.4) covered on one side with a random layer of polystyrene spheres of diameter $3\mu m$. The glass plate GP makes an angle $\Delta\theta_{scat}$ with z, the axis of propagation of the incident beam. Parallel to the plate, a mirror M_s is located at a distance ΔL_{scat} from GP along z. The mirror creates an image GP' of the glass plate and we denote $\Delta\mathbf{r}_{scat} = (\Delta x_{scat}, \Delta y_{scat}, \Delta z_{scat})$ as the separation between a particle S on the glass plate and its image S' in the plane GP' (see Fig. 4.4). As we will see in Section 4.3.2, the incident field has a coherence volume significantly larger than the size of the spheres; hence, we can represent a sphere by a delta function. Accordingly, the

scattering potential is given by

$$\eta(\mathbf{r}) = \sum_i \delta(\mathbf{r} - \mathbf{r}_i) + \delta(\mathbf{r} - \mathbf{r}_i - \Delta\mathbf{r}_{scat}), \tag{4.17}$$

where $\mathbf{r}_i$ and $\mathbf{r}_i + \Delta\mathbf{r}_{scat}$ are the positions of the particle i and its image on the planes GP and GP' respectively.

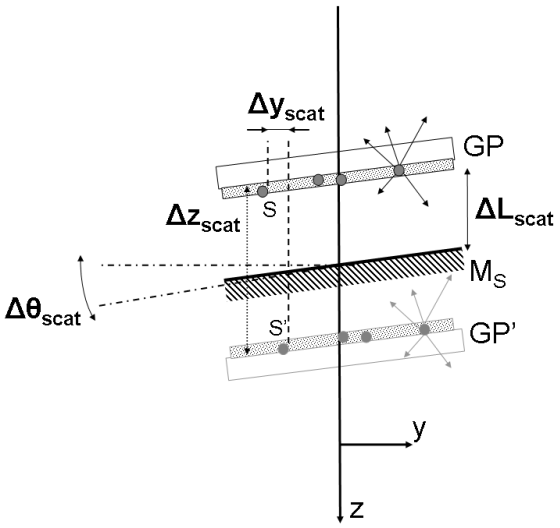

Figure 4.4: Schematic representation of the scattering medium.

The spheres are randomly placed on GP and, from Eq. (4.17), it follows that the second moment of the spatial correlation of the scattering potential is proportional to

$$C(\mathbf{r}_1,\mathbf{r}_2) \propto \delta(\Delta\mathbf{r}) + \frac{1}{2}\delta(\Delta\mathbf{r}+\Delta\mathbf{r}_{scat}) + \frac{1}{2}\delta(\Delta\mathbf{r}-\Delta\mathbf{r}_{scat}), \tag{4.18}$$

with $\Delta\mathbf{r} = \mathbf{r}_1 - \mathbf{r}_2$.

We recognize that the correlation in Eq. (4.18) has the same form as in Eq. (4.13) where the parameter m_η equals $1/2$. The relations between the geometrical parameters

Δx_{scat}, Δy_{scat}, Δz_{scat}, ΔL_{scat} and $\Delta\theta_{scat}$ describing the scattering medium are $\Delta z_{scat} = 2\Delta L_{scat}\cos^2(\Delta\theta_{scat})$, $\Delta y_{scat} = 2\Delta L_{scat}\cos(\Delta\theta_{scat})\sin(\Delta\theta_{scat})$ and $\Delta x_{scat} = 0$. Accordingly, by measuring ΔL_{scat} and $\Delta\theta_{scat}$, we inferred that $\Delta z_{scat} = 1.7mm$ and $\Delta y_{scat} = 0.08mm$.

4.3.2 Synthesis of the partially coherent probe beam

In order to recover the function C from a scattering experiment, we generated a beam with a degree of coherence given by Eq. (4.6). For this purpose, we use a Nd:YAG laser doubled in frequency at $\lambda = 532nm$ to generate the intensity profile given in Eq. (4.5). The laser beam passes through a concave lens L_0 (see Fig. 4.5) and illuminates a Michelson interferometer. The intensity pattern described in Eq. (4.5) is generated by detuning the two mirrors M_1 and M_2 by a distance ΔL from the zero path position. The output beam is then focused by the lens L_c and reflected by the mirror M_3. A circular aperture A is located in the focal plane of the lens L_c. The superposition of the fields coming from the two arms of the Michelson generates an interference pattern with an intensity profile in the plane of the aperture similar to a Newton's rings pattern:

$$I_A(x,y) = \frac{1}{2}\left(1 + \cos\left[\frac{2\pi}{\lambda}\Delta L\frac{(x-x_A)^2 + (y-y_A)^2}{f_c^2} - \frac{4\pi}{\lambda}\Delta L\right]\right), \tag{4.19}$$

where x and y are the coordinate in the plane of the aperture A with their origin taken at the center of the aperture, x_A and y_A are the coordinate of the rings center.

One can see that Eqs. (4.19) and (4.5) have similar forms. The periodicity of the rings in the intensity pattern is adjusted by the location ΔL of the mirror M_1 whereas the relative position $\mathbf{r}_A$ between the center of the rings and the fixed center of the aperture A depends on the angular inclination $\Delta\theta$ of the mirror M_3 which is controlled by two motors. Using the cube beam splitter CB_2, the lens L_1 images, with a magnification $\chi = 1.1$, the plane of the aperture A onto the plane of the rotating diffuser. Therefore, the intensity profile on the diffuser is given by $I_A(\mathbf{r}/\chi)$ which corresponds to the expression in Eq. (4.5) with the parameters $\alpha = \chi f_c\sqrt{\lambda/\Delta L}$, $\beta = 4\pi\Delta L/\lambda$, $x_0 = \chi x_A$ and $y_0 = \chi y_A$. The parameter R in Eq. (4.5) is the radius of the image by L_1 of the aperture A.

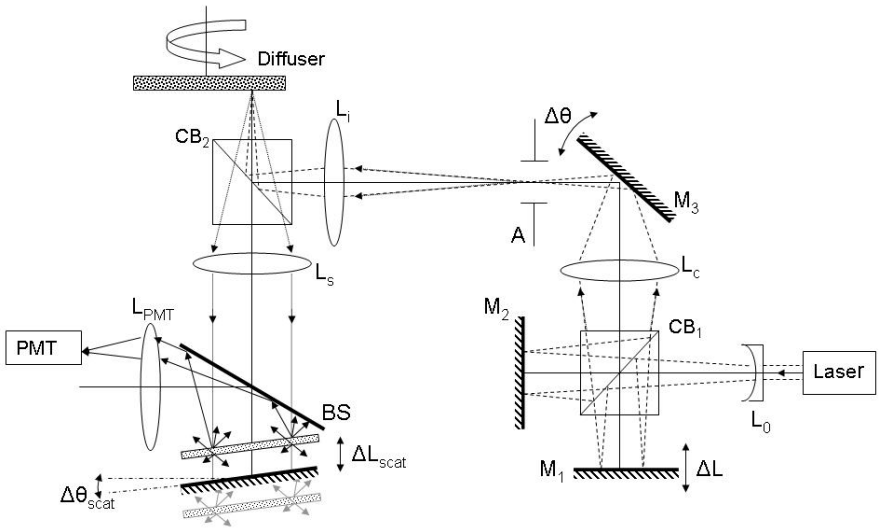

Figure 4.5: Experimental setup for variable coherence tomography.

The diffuser is a slightly rough piece of aluminum which backscatters the light uniformly in the direction of the lens L_s. The diffuser can therefore be considered as a spatially

incoherent secondary source with an intensity profile given by Eq. (4.5). The backscattered light from the diffuser passes through the cube beam splitter CB_2 and is collimated by the lens L_s. The beam emerging from L_s is our probe field which has a spatial degree of coherence given by Eq. (4.6). The focal length of L_s is $f_s = 62.9mm$ and we use $R = 3mm$. Using these parameters, one can evaluate the size of the volume of coherence given by $|g(\Delta\mathbf{r})|$. Its transversal width at half maximum is approximately $\lambda f_s/(2R) \simeq 6\mu m$ and its longitudinal length at half maximum is around $2\lambda f_s^2/R^2 = 470\mu m$. Note that the coherence volume is larger than the micro-spheres composing the scattering medium which allows using the approximation of Eq. (4.17).

4.3.3 Scattering potential reconstruction using variable coherence tomography

The experimentally designed partially coherent beam presented in Section 4.3.2 illuminates the correlated scattering system after passing through the beam splitter BS (see Fig. 4.5). The scattered intensity is then reflected on BS and collected by the lens L_{PMT}. A photomultiplier tube (PMT) reads the intensity passing through a pinhole located in the focal plane of L_{PMT}. The position of this pinhole is such that only the scattered intensity is detected. The PMT signal is recorded as a function of the position ΔL of the mirror M_1, while the center of the intensity pattern x_0 and y_0 is kept fixed. Then the scanning is repeated for the same set of values of ΔL but for different values of x_0 and y_0 which are controlled by the position of the mirror M_3.

According to Eq. (4.16), we have to adjust the coherence properties of the incident beam such that $|g(\Delta\mathbf{r}_0 - \Delta\mathbf{r}_{scat})|$ is maximum. Consequently, we need $\Delta\mathbf{r}_0 = \Delta\mathbf{r}_{scat}$ in order to have a high interference modulation. Using Eq. (4.7) and the relation $\alpha = \chi f_c\sqrt{\lambda/\Delta L}$ from Section 4.3.2, it follows that

$$-\frac{2f_s\Delta L}{(\chi f_c)^2}x_0 = \Delta x_{scat}, \quad -\frac{2f_s\Delta L}{(\chi f_c)^2}y_0 = \Delta y_{scat}, \quad \frac{2f_s^2\Delta L}{(\chi f_c)^2} = \Delta z_{scat}. \tag{4.20}$$

We have experimentally measured the intensity and, for each scanning set of ΔL, we calculated the average intensity D_I. We then divided the measured intensity by D_I and subtracted 1 in order to obtain the oscillating part of the intensity according to Eq. (4.16). The experimental measurements are displayed in Fig. 4.6 for three different values of y_0. On each curve, we superposed its envelope calculated from the Hilbert transform of the oscillating part of $I^{(s)}(r\mathbf{u}, \Delta\mathbf{r}_0)$. One can see from Fig. 4.6 that, in each plot, the intensity fluctuates as ΔL changes. However, the oscillations of the scattered intensity have a larger amplitude for a certain range of ΔL. According to Eq. (4.16), the envelope of the oscillations corresponds to $|g(\Delta\mathbf{r}_0 - \Delta\mathbf{r}_{scat})|$; the oscillation amplitude is therefore larger when $\Delta\mathbf{r}_0 - \Delta\mathbf{r}_{scat}$ approaches zero.

The envelopes of the intensity for the three different values of y_0 are also plotted in Fig. 4.7. The positions of the maxima are different, as they depend on the shape of the function $g(\mathbf{r})$. However, one can see that the envelope corresponding to $y_0 = -3mm$ has the highest maximum value because it corresponds to the situation in which $\Delta\mathbf{r}_0 \simeq \Delta\mathbf{r}_{scat}$ at the maximum position. We experimentally measured that $x_0 = 0.2mm$, $y_0 = -3mm$

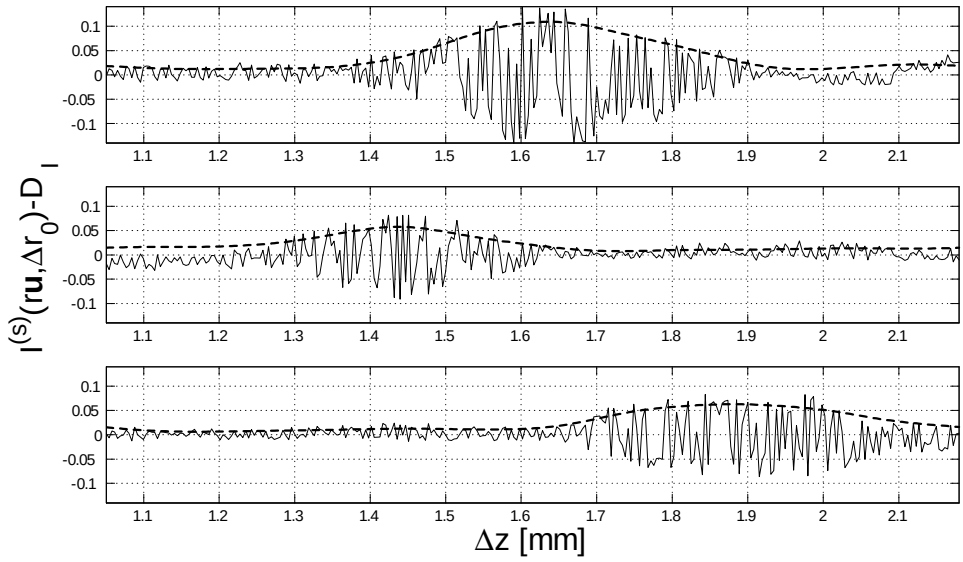

Figure 4.6: Oscillating part of the scattered intensity for $x_0 = 0.2mm$ and three different values of y_0. From top to bottom, $y_0 = -3mm$, $y_0 = -3.3mm$, $y_0 = -2.6mm$. The dashed line is the intensity envelope.

and $\Delta L = 5.6mm$. Since $\chi = 1.1$, $f_s = 62.9mm$ and $f_c = 150mm$, we deduced that $\Delta x_{scat} = 0.005mm$, $\Delta y_{scat} = 0.08mm$ and $\Delta z_{scat} = 1.63mm$. A good agreement is found with the value of $\Delta \mathbf{r}_{scat}$ measured directly: $\Delta x_{scat} = 0mm$, $\Delta y_{scat} = 0.08mm$, $\Delta z_{scat} = 1.7mm$.

The results in Fig. 4.7 clearly show that the correlation function of the complex susceptibility can be estimated from the envelope of the variations in the scattered intensity as the parameter $\Delta \mathbf{r}_0$ is changed. We obtained a fairly good signal to noise ratio in our experiment since the maximum modulation is around 0.11 (see Fig. 4.7) and the background signal is about 0.015. From Eq. (4.16), one can see that the maximum scattered intensity modulation is $m_\eta m$. In Section 4.3.1, we have established that $m_\eta = 0.5$, and assuming an

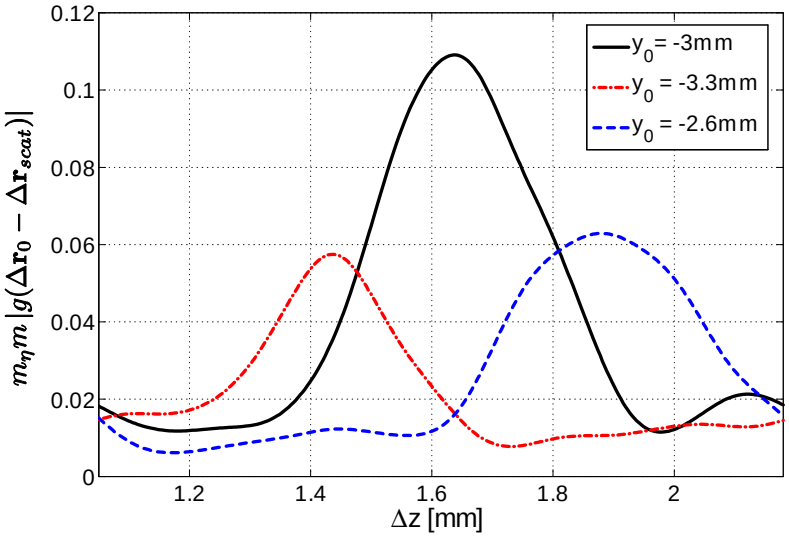

Figure 4.7: Envelopes of the scattered intensity for $x_0 = 0.2mm$ and $y_0 = -3mm$, $y_0 = -3.3mm$ and $y_0 = -2.6mm$.

ideal case where the intensity pattern on the diffuser is fully modulated, i.e. $m = 1$, the maximum scattered intensity modulation is 0.5. However, this estimation does not account for multi-scattering effects which can be considered as an incoherent background intensity that is independent of $\Delta\mathbf{r}_0$ and that reduces the amplitude of the modulation.

Note also that in Fig. 4.7 the FWHM of the envelope with the highest maximum value is $\approx 400\mu m$. In the longitudinal direction, the FWHM of $|g(\mathbf{r})|$ is the largest and it was evaluated to be $470\mu m$. We experimentally varied $\Delta\mathbf{r}_0$ and measured the envelope of $|g(\Delta\mathbf{r}_0 - \Delta\mathbf{r}_{scat})|$. Since $\Delta\mathbf{r}_{scat}$ has components along the unit vectors $\mathbf{x}$, $\mathbf{y}$ and $\mathbf{z}$, the envelope of $|g(\Delta\mathbf{r}_0 - \Delta\mathbf{r}_{scat})|$ was practically evaluated in a direction different from the longitudinal axis. For this reason, the measured width is smaller than the longitudinal one.

Furthermore, because the $\mathbf{z}$ component of $\Delta\mathbf{r}_{scat}$ is much larger than the $\mathbf{x}$ and $\mathbf{y}$ components, there is a small angle between the longitudinal axis and the direction along which the envelope of $|g(\Delta\mathbf{r}_0 - \Delta\mathbf{r}_{scat})|$ was evaluated. For this reason, the measured value of the FWHM is rather close to the longitudinal FWHM value.

4.4 Conclusion

Variable coherence tomography introduced in this chapter is a novel approach for solving the inverse problem associated with scattering from a random potential. In this method, the shape of the degree of spatial coherence of a beam is varied such that the field is correlated in two separate volumes with an adjustable spatial separation. We have demonstrated that such optical fields with special coherence properties can be further used in a tomographic procedure based on variable coherence. We successfully recovered experimentally the degree of correlation of the complex susceptibility by varying only the shape of the degree of coherence of the incident beam and measuring the scattered intensity in a single direction. Our method for determining the pair-correlation function of a scattering potential is practically appealing because intensity measurements are always easier to implement than measurements of cross-spectral density. Furthermore, the approach requires only an incoherent light source with adjustable intensity distribution that can be easily obtained using, for instance, a spatial light modulator.

In the experiments described here, the resolution is given by the dimensions of the coherence volume of the incident beam, which are large in comparison to the wavelength, especially in the longitudinal direction. The longitudinal size Δz of the coherence volume is indeed related to the transverse dimension Δx by the relation $\Delta z = 8\Delta x^2/\lambda$. From this last expression, we see that, unless Δx is on the order of the wavelength, Δz is much larger than Δx. Moreover, the use of a beam as a probing field limits our treatment to paraxial angles meaning that Δx cannot be smaller than 10λ and, therefore, the value of Δz is at least $10^3\lambda$. However, we note that our method is not limited to optical fields and it could find applications, for instance, in electron microscopy where the wavelength used can be much less than $1\mathring{A}$. Instead of limiting the probing field to small angles of incidence, one could use a larger number of incident angles in order to improve the resolution as it will be discussed in Chapter 6.

The reconstruction method of variable coherence tomography is based on the single scattering approximation. In general, unfortunately, the long-range coherence properties of the field do not survive multiple scattering since the visibility of the signal originating from the single scattering is significantly reduced by the incoherent intensity background. On the other hand, as we have seen in Section 2.2.4, the radiative transfer formalism is valid in the multiple scattering regime but it does not account for long-range correlations. Furthermore, the method discussed in Chapter 3 relies on the small angle approximation which limits the field propagation in the medium to distances smaller than the transport mean free path. To bridge the gap between these extremes, we will use an approach similar to variable

coherence tomography and we will introduce in the next chapter a sensing method capable of probing highly diffusive media.

CHAPTER 5

ENHANCED BACKSCATTERING WITH SHAPED PARTIALLY COHERENT LIGHT

As mentioned in the previous chapter, the interaction between optical waves and random media is often developed in a multiple scattering regime. In this context, much attention has been paid recently to the phenomenon of enhanced coherent backscattering (CBS). Since the coherence properties of the incident field were shown to affect the shape of the backscattering peak [61, 62], several sensing procedures have focused on varying the degree of coherence in order to infer various information about the target medium. For instance, broadband sources with reduced temporal coherence length have been used to probe superficial layers in biological tissues [17]. Very recently, the spatial coherence properties of an incident singular beam were changed in order to deduce the transport mean free path of a scattering medium without measuring the background intensity level as required in conventional CBS experiments [2].

After reviewing the origin and the basic concepts of CBS, we will show in this chapter that both the transport mean free path and the probability of radial intensity distribution can be retrieved by illuminating a diffusive medium with a spatially partially coherent beam. Similarly to the procedure of variable coherence tomography introduced in Chapter 4, the spatial coherence properties of the incident beam are shaped such that the field is correlated

in two distinct volumes separated by an adjustable distance. Notably, our technique does not require measuring the background intensity level and it can be quite easily applied to evaluate anisotropic diffusion coefficients.

5.1 Enhanced coherent backscattering

5.1.1 Multiple scattering and weak localization of light

Coherent enhanced backscattering originates from the constructive interferences of the scattered waves which generate, in the far-field , an enhancement of intensity over the diffuse background [63]. These interferences are produced in the exact backscattering direction by the light following time reversal paths in the medium; it is the only coherent effect that survives the ensemble averaging over the medium's realizations. The radiative transfer equation fails to predict enhanced backscattering since the ladder diagrams used in this formalism only consider short-range correlations occurring at scales on the order of the inhomogeneities size [12]. The maximally crossed or cyclical diagrams need to be introduced in the derivation of the scattered field in order to account for the long-range correlations between the waves following identical paths but in reverse sequence of scattering events [18].

Even though the first clear experimental demonstration of CBS using light was made in 1984 [64], an analogous phenomenon referred to as weak Anderson localization was observed earlier in the field of solid state physics in the case of electronic transport in metals. Recent

experimental measurements on the correlation between the spatial and angular distribution of the backscattered field have demonstrated the phase conjugation effect of CBS [65]. It follows that a diffusive scattering medium acts as coherent imaging system free of aberration. However, as it was shown in a double passage configuration, the contrast of the image is reduced by the background intensity [66].

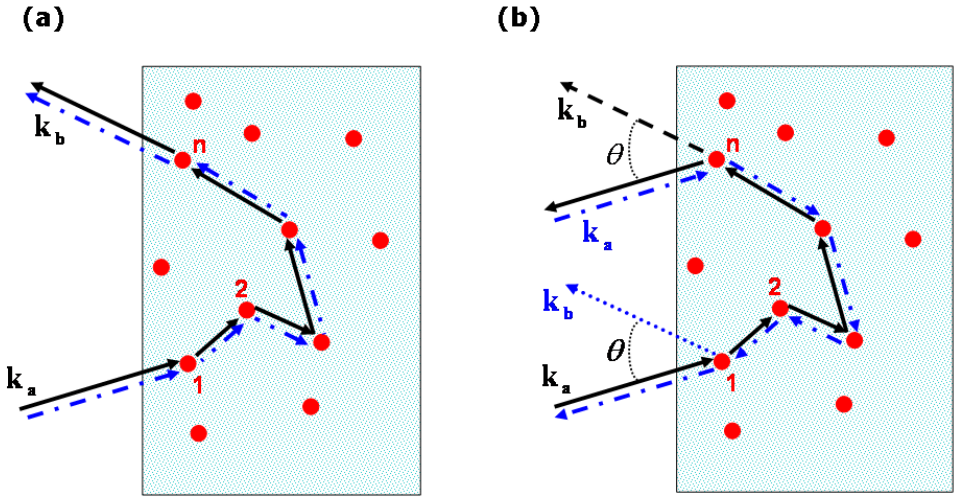

Figure 5.1: (a) Scattering trajectory contributing to the incoherent background intensity. (b) Time reciprocal path at the origin of coherent enhanced backscattering.

Let us consider a monochromatic plane wave characterized by the wave vector $\mathbf{k}_a$ and incident upon a multiple scattering media. In order to analyze the complete scattering mechanism, we first follow the trajectory of the light along the scattering sequence composed of the particles 1, 2, ..., n as illustrated in Fig. 5.1. The light enters the medium at the location $\mathbf{r}_i$ of the particle 1 and exits at the location $\mathbf{r}_j$ of the particle n with a direction

defined by the wave vector $\mathbf{k}_b$. The contribution of this scattering sequence to the total complex amplitude of the field leaving the medium in the direction $\mathbf{k}_b$ can be expressed as

$$\delta_{ij}^{m} A\left(\mathbf{k}_b, \mathbf{k}_a\right) = p_m \exp\left(i\phi_m\right) \exp\left(i\mathbf{k}_a \cdot \mathbf{r}_i - i\mathbf{k}_b \cdot \mathbf{r}_j\right), \tag{5.1}$$

with p_m and ϕ_m being the amplitude and the dynamical phase introduced during the scattering process. Summing Eq. (5.1) over all the possible paths m which lead from the initial point $\mathbf{r}_i$ to the final point $\mathbf{r}_j$, we obtain the following amplitude

$$\delta_{ij} A\left(\mathbf{k}_b, \mathbf{k}_a\right) = \sum_m p_m \exp\left(i\phi_m\right) \exp\left(i\mathbf{k}_a \cdot \mathbf{r}_i - i\mathbf{k}_b \cdot \mathbf{r}_j\right) \tag{5.2}$$

of the field which emerges at $\mathbf{r}_j$ with the wave vector $\mathbf{k}_b$ due to the impulse response of the incident field at point $\mathbf{r}_i$. The total field scattered by the medium in the direction $\mathbf{k}_b$ corresponds to the integration of $\delta_{ij} A\left(\mathbf{k}_b, \mathbf{k}_a\right)$ over all coordinates of the initial and final points $\mathbf{r}_i$ and $\mathbf{r}_j$. Consequently, using Eq. (5.2), the average total intensity scattered along $\mathbf{k}_b$ becomes

$$\left\langle \left| A\left(\mathbf{k}_b, \mathbf{k}_a\right) \right|^2 \right\rangle = \sum_{i,j,k,l} \left\langle f^*\left(\mathbf{r}_i, \mathbf{r}_j\right) f\left(\mathbf{r}_k, \mathbf{r}_l\right) \exp\left[i\mathbf{k}_a \cdot \left(\mathbf{r}_k - \mathbf{r}_i\right) - i\mathbf{k}_b \cdot \left(\mathbf{r}_l - \mathbf{r}_j\right)\right] \right\rangle, \tag{5.3}$$

where $\langle ... \rangle$ denotes the ensemble averaging over the medium's realizations and

$$f\left(\mathbf{r}_i, \mathbf{r}_j\right) = \sum_m p_m \exp\left(i\phi_m\right). \tag{5.4}$$

Because of the random phase introduced by the different configurations of the particles between realizations, the only terms which survive the ensemble averaging process correspond to the situations $(i = k, l = j)$ and $(i = j, k = l)$. Equation (5.3) can then be written as

$$\left\langle \left| A\left(\mathbf{k}_b, \mathbf{k}_a\right) \right|^2 \right\rangle = \sum_{i,j} P\left(\mathbf{r}_i, \mathbf{r}_j\right) \left\{1 + \cos\left[\left(\mathbf{k}_a + \mathbf{k}_b\right) \cdot \left(\mathbf{r}_j - \mathbf{r}_i\right)\right]\right\}, \tag{5.5}$$

where $P(\mathbf{r}_i, \mathbf{r}_j) = \left\langle |f(\mathbf{r}_i, \mathbf{r}_j)|^2 \right\rangle$ represents the probability distribution of intensity transfer from point $\mathbf{r}_i$ to the location $\mathbf{r}_j$.

The first component in the summation (5.5) is an incoherent term, independent of $\mathbf{k}_b$, which corresponds to the case illustrated in Fig. 5.1(a), where conjugated waves follow the same scattering sequence. These trajectories are the only ones taken into account by the radiative transfer equation or the diffusion equation. In addition to this constant intensity background, the second component in the summation (5.5) relates to the interference between waves travelling along reciprocal paths as shown in Fig. 5.1(b). If $\mathbf{k}_a + \mathbf{k}_b \neq 0$ or, more precisely, if the angle θ represented in Fig. 5.1(b) is larger than, typically, few degrees as we will see in the next section, then the summations over $\mathbf{r}_j$ and $\mathbf{r}_i$ average the cosine term to zero and only the incoherent background intensity remains. However, in the exact backscattering direction, i.e. $\mathbf{k}_a = -\mathbf{k}_b$, the cosine function is identically 1 and the wave travelling along a scattering sequence interfere constructively in the far-field with the conjugated wave which follows the same sequence in reverse order. The intensity in the backscattering direction is then enhanced and its value is twice the value of the background intensity.

5.1.2 Angular dependence in the diffusion approximation

The exact shape of the reflected intensity $\left\langle |A(\mathbf{k}_b, \mathbf{k}_a)|^2 \right\rangle$, also called albedo α, depends on the nature of the medium and the form of the probability distribution $P(\mathbf{r}_i, \mathbf{r}_j)$. In general, $P(\mathbf{r}_i, \mathbf{r}_j)$ obeys a transport equation which is well approximated by the diffusion

equation when considering multiple scattering trajectories far enough from the interface. The evaluation of $P(\mathbf{r}_i, \mathbf{r}_j)$ reduces then to a random walk problem where the probability of joining the points $\mathbf{r}_i$ and $\mathbf{r}_j$ without crossing the interface of the medium needs to be evaluated. In the case of a semi-infinite disordered medium occupying the half space $z \geq 0$, the diffusion equation (2.51) gives [67]

$$P(\boldsymbol{\rho}, z_i, z_j) = \frac{1}{4\pi c D}\left[\frac{1}{\sqrt{\boldsymbol{\rho}^2 + (z_i - z_j)^2}} - \frac{1}{\sqrt{\boldsymbol{\rho}^2 + (z_i + z_j + 2z_0)^2}}\right], \tag{5.6}$$

where D is the diffusion coefficient, c is the wave speed and the parameter $z_0 = 2l_t/3$ is imposed by the boundary conditions and depends on the transport mean free path l_t. In Eq. (5.6), the medium was assumed to be homogeneous such that P is a function of the transverse separation $\boldsymbol{\rho} = \mathbf{r}_{i\perp} - \mathbf{r}_{j\perp}$, where $\mathbf{r}_\perp$ is the projection of $\mathbf{r}$ onto the interface Σ of the medium defined by the plane (x, y).

Using Eq. (5.5) and accounting for the attenuation of the incident and emerging waves by an exponential factor, the albedo can be expressed as [18, 67]

$$\begin{aligned}\alpha(\mathbf{s}_b, \mathbf{s}_a) = \frac{c}{4\pi l_s^2}\iint_0^\infty \int_\Sigma \exp\left(-\frac{z_i}{\mu_a l_s}\right)\exp\left(-\frac{z_j}{\mu_b l_s}\right) P(\boldsymbol{\rho}, z_i, z_j) \\ \times \left\{1 + \cos\left[k(\mathbf{s}_{b\perp} + \mathbf{s}_{a\perp})\cdot\boldsymbol{\rho} + k(\mu_a - \mu_b)(z_i - z_j)\right]\right\} d^2\boldsymbol{\rho} dz_i dz_j,\end{aligned} \tag{5.7}$$

where $\mathbf{s}_\perp$ is the projection onto the plane (x, y) of the unit vector $\mathbf{s}$ along $\mathbf{k}$ and $\mu = |\cos(\theta)|$ is the absolute value of the projection of $\mathbf{s}$ along $\mathbf{z}$. Equation (5.7) was derived for isotropic scattering and, in this case, l_s represents the scattering mean free path. Moreover, considering paraxial directions for the incident and scattered fields, we have, in a good approximation,

$\mu_a = \mu_b = 1$ in Eq. (5.7). The albedo can then be written as

$$\alpha\left(\mathbf{s}_b, \mathbf{s}_a\right) = \alpha_d + \alpha_c\left(\mathbf{s}_b, \mathbf{s}_a\right), \tag{5.8}$$

with the incoherent albedo α_d defined as

$$\alpha_d = \frac{c}{4\pi l_s^2}\int_{\Sigma} P\left(\boldsymbol{\rho}\right) d^2\boldsymbol{\rho}, \tag{5.9}$$

and the coherent albedo $\alpha_c\left(\mathbf{s}_b, \mathbf{s}_a\right)$ which takes the form

$$\alpha_c\left(\mathbf{s}_b, \mathbf{s}_a\right) = \frac{c}{4\pi l_s^2}\,\mathrm{Re}\left\{\int_{\Sigma} P\left(\boldsymbol{\rho}\right)\exp\left[ik\left(\mathbf{s}_{b\perp} + \mathbf{s}_{a\perp}\right)\cdot\boldsymbol{\rho}\right] d^2\boldsymbol{\rho}\right\}. \tag{5.10}$$

As one can recognize from Eq. (5.10), the shape α_c of the coherent backscattering cone is proportional to the Fourier transform of the function

$$P\left(\boldsymbol{\rho}\right) = \iint_0^{\infty}\exp\left(-\frac{z_i + z_j}{l_s}\right) P\left(\boldsymbol{\rho}, z_i, z_j\right) dz_i dz_j, \tag{5.11}$$

which constitutes the probability distribution of joining two points at the surface of the medium separated by the vector $\boldsymbol{\rho}$. The integral in Eq. (5.10) can also be seen as an infinite superposition of interference patterns generated by Young pinholes separated by the distance ρ. For each pair of pinholes, the periodicity of the modulation is set by ρ while the amplitude depends on $P\left(\boldsymbol{\rho}\right)$. The integration over $\boldsymbol{\rho}$ and the ensemble averaging over the medium realizations wash out the interferences except in the exact backscattering direction where the fields interfere constructively.

Substituting Eq. (5.6) into Eq. (5.7), the albedo $\alpha\left(\mathbf{s}_b, \mathbf{s}_a\right)$ becomes [68]

$$\alpha\left(\mathbf{s}_b, \mathbf{s}_a\right) = \frac{3}{8\pi}\left\{1 + \frac{2z_0}{l_t} + \frac{1}{\left(1 + k_\perp l_t\right)^2}\left[1 + \frac{1 - \exp\left(-2\Delta k_\perp l_t\right)}{k_\perp l_t}\right]\right\}, \tag{5.12}$$

where $k_\perp = k\,|\mathbf{s}_{b\perp} - \mathbf{s}_{a\perp}|$ and the scattering mean free path l_s has been replaced by l_t based on heuristic arguments in order to allow for anisotropic scattering when the particles size is of the order or larger than the wavelength. The albedo, calculated using Eq. (5.12), is represented in Fig. 5.2 for a plane wave coming at normal incidence on a diffusive medium characterized by the transport mean free path $l_t = 100\mu m$. We observe that the intensity at $\mathbf{s}_\perp = 0$ is twice the background intensity at large angles. The angular width of the cone is on the order of $\lambda/(2\pi l_t)$ [68].

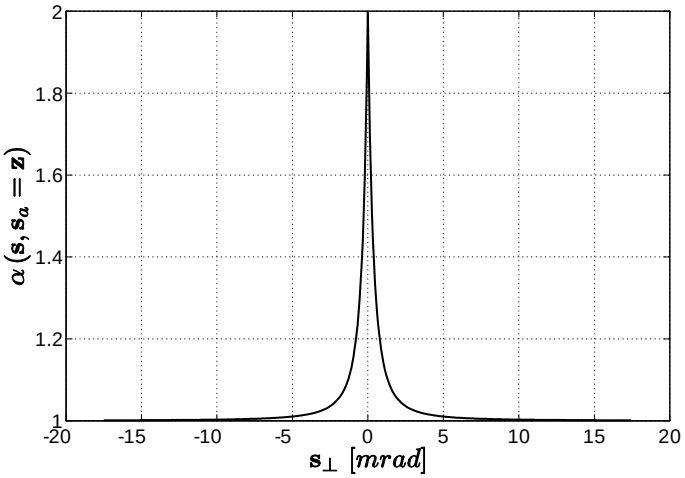

Figure 5.2: Angular intensity $\alpha(\mathbf{s}_b, \mathbf{s}_a)$ backscattered from a diffusive medium characterized by $l_t = 100\mu m$ and illuminated by a monochromatic plane wave at normal incidence, i.e. $\mathbf{s}_a = \mathbf{z}$. The albedo is normalized to the background intensity at large angles.

The absorption of the medium can also be taken into account by formally replacing $k_\perp$ by $\sqrt{\mathbf{k}_\perp^2 + 3/(l_a l_t)}$, with l_a being the absorption length [18]. Further treatments have

introduced corrections to the shape (5.12) of the coherent backscattering peak due to total internal reflection and boundary effects [69, 70].

5.1.3 Polarization of the enhanced backscattering peak

The previous description of CBS was based on the scalar approximation, which arises from the use of the diffusion equation. In this framework, the polarization of the incoming field is neglected, as well as the changes in the polarization state of the photons travelling along the scattering trajectories. Due to multiple scattering, the polarization of the field becomes randomized after some propagation length [71]. This depolarization process modifies the exact reciprocity of the time reversal paths, therefore modifying the interference effect. Consequently, the vectorial nature of the electromagnetic field needs to be considered in order to account for the depolarizing effect of multiple scattering [72, 73].

The coherent albedo $\alpha_c^{\parallel}$ observed in the co-polarized channel can be expressed as a superposition of the scalar coherent albedo defined in Eq. (5.10) and a broad contribution due to scattering paths shorter than the depolarization length [18, 74]. The cross-polarized coherent albedo $\alpha_c^{\perp}$ depends on the transfer of intensity from one polarization to the other. For the case of Rayleigh scattering, the enhancement between $\alpha_c^{\perp}$ and the incoherent background is smaller than for the co-polarized channel. However, as the size of the scatterers increases, the difference between $\alpha_c^{\parallel}$ and $\alpha_c^{\perp}$ reduces. In general, however, Eq. (5.12) gives good results if the backscattered intensity is examined in the co-polarized channel at small angles [18].

5.2 Enhanced backscattering of partially coherent light

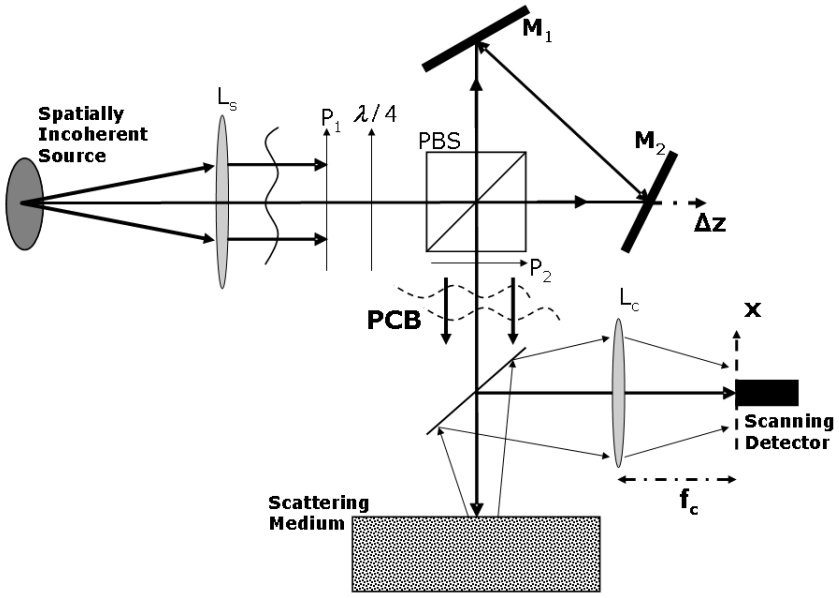

Figure 5.3: Schematic of the experimental setup used for enhanced backscattering with shaped spatially partially coherent light.

Let us consider the experimental setup sketched in Fig. 5.3 where a quasi-monochromatic spatially incoherent source S with intensity distribution $Q(\mathbf{x})$ is placed in the focal plane of a collecting lens L_s. The second-order coherence properties of the beam generated after L_s are characterized by the cross-spectral density $W(\mathbf{r}, \mathbf{r}') = \langle E^*(\mathbf{r}) E(\mathbf{r}') \rangle$ where $\mathbf{r}$ and $\mathbf{r}'$ are position vectors in space and the averaging $\langle ... \rangle$ is taken over the stationary ensemble $\{E(\mathbf{r})\}$ of field realizations. Using the van Cittert-Zernike theorem expressed in Eq. (2.19),

$W(\mathbf{r},\mathbf{r}')$ depends on $Q(\mathbf{x})$ according to the relation

$$W(\mathbf{r},\mathbf{r}') = \int_S Q(\mathbf{x}) \exp\left[i\frac{k}{f}\mathbf{x}\cdot(\mathbf{r}-\mathbf{r}')\right] d^2\mathbf{x}, \tag{5.13}$$

where k is the wave number and f is the focal length of L_s. As one can see from Eq. (5.13), $W(\mathbf{r},\mathbf{r}')$ depends only on the separation $\boldsymbol{\rho}=\mathbf{r}-\mathbf{r}'$, thus one can define $W(\mathbf{r},\mathbf{r}') = g(\boldsymbol{\rho})$. Considering a source of radius R with intensity distribution such that $Q(\mathbf{x}) = 1$ if $|\mathbf{x}| \leq R$ and equals zero otherwise, the function g illustrated in Fig. 5.4 satisfies

$$g(\boldsymbol{\rho}) = 4\pi R^2 \frac{J_1(u)}{u}, \tag{5.14}$$

with J_1 being the first order Bessel function and $u = kR|\boldsymbol{\rho}|/f$. In a plane transverse to the direction of propagation of the beam, the width of $g(\boldsymbol{\rho})$ is approximately $\lambda f/(2R)$ and relates to the transverse coherence length of the field.

As represented in Fig. 5.3, a polarizer P_1 and a quarter-wave plate placed after L_s allow us to vary the state of polarization of the beam before it enters the shear interferometer composed of a polarizing cube beam splitter PBS and two mirrors M_1 and M_2. At the output of the interferometer, the resulting beam is a superposition of two overlapping replicas of the incident field propagating along the same mean direction $\mathbf{z}$ and spatially separated by an adjustable distance ρ_0. The two orthogonally polarized replicas are projected along the same polarization state by a second polarizer P_2. The resulting beam has a cross-spectral density of the form

$$W_{\boldsymbol{\rho}_0}(\boldsymbol{\rho}) = g(\boldsymbol{\rho}) + \frac{m}{2}\exp(i\phi)\, g(\boldsymbol{\rho}-\boldsymbol{\rho}_0) + \frac{m}{2}\exp(-i\phi)\, g(\boldsymbol{\rho}+\boldsymbol{\rho}_0), \tag{5.15}$$

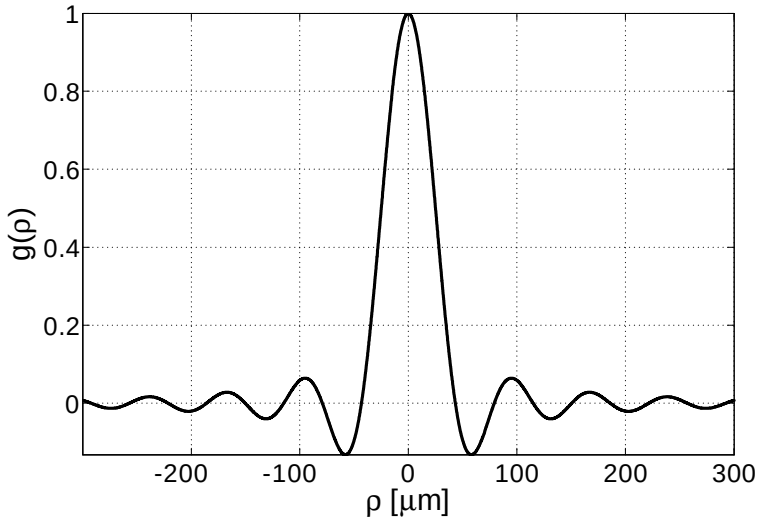

Figure 5.4: Normalized representation of the coherence function g defined in Eq. (5.14) and plotted for the parameters $R = 1.5mm$, $\lambda = 532nm$ and $f = 200mm$.

where $m = 2\sqrt{I_1 I_2}/\left(I_1 + I_2\right)$ accounts for the modulation and ϕ for the phase of the fringe pattern generated by the interference between the two fields of intensity I_1 and I_2 corresponding to the two paths of the interferometer. The phase ϕ can be adjusted by varying the orientation of the quarter wave plate and the polarizers. Using Eq. (2.19), the beam characterized by the cross-spectral density $W_{\boldsymbol{\rho}_0}$ can equivalently be described as a superposition of uncorrelated plane waves with propagating direction $\mathbf{s}_0$ and an average intensity given by

$$I\left(\mathbf{s}_0, \boldsymbol{\rho}_0\right) = \frac{1}{2} Q\left(f\mathbf{s}_{0\perp}\right)\left[1 + m\cos\left(k\mathbf{s}_{0\perp}\cdot\boldsymbol{\rho}_0 - \phi\right)\right], \tag{5.16}$$

where $\mathbf{s}_{0\perp}$ is the projection of $\mathbf{s}_0$ along $\mathbf{z}$.

The beam is incident upon a scattering medium characterized by the albedo $\alpha(\mathbf{s}, \mathbf{s}_0)$, where $\mathbf{s}$ and $\mathbf{s}_0$ relate to the propagation direction of the scattered and incident fields, respectively. The intensity $\overline{I_b}$ of the field backscattered in the direction $\mathbf{s}$ and averaged over both the incident field and different realizations of the scattering medium can be expressed as a convolution [61]

$$\overline{I_b}(\mathbf{s}, \boldsymbol{\rho}_0) = \int_{|\mathbf{s}_{0\perp}|\leq 1} \alpha(\mathbf{s}, \mathbf{s}_0) I(\mathbf{s}_0, \boldsymbol{\rho}_0) d^2\mathbf{s}_{0\perp}, \tag{5.17}$$

between the angular spectrum $I(\mathbf{s}_0, \boldsymbol{\rho}_0)$ of the incident field and the albedo $\alpha(\mathbf{s}, \mathbf{s}_0)$. Substituting Eqs. (5.8) and (5.16) into Eq. (5.17), the distribution of the backscattered intensity can be expressed as

$$\begin{aligned} \overline{I_b}(\mathbf{s}, \boldsymbol{\rho}_0) &= \frac{1}{2}\int_{|\mathbf{s}_{0\perp}|\leq 1} \alpha_d Q(f\mathbf{s}_{0\perp}) \left[1 + m\cos\left(k\mathbf{s}_{0\perp}\cdot\boldsymbol{\rho}_0 - \phi\right)\right] d^2\mathbf{s}_{0\perp} \\ &\quad + \frac{1}{2}\int_{|\mathbf{s}_{0\perp}|\leq 1} \alpha_c(\mathbf{s}, \mathbf{s}_0) Q(f\mathbf{s}_{0\perp}) d^2\mathbf{s}_{0\perp} \\ &\quad + \frac{m}{2}\int_{|\mathbf{s}_{0\perp}|\leq 1} \alpha_c(\mathbf{s}, \mathbf{s}_0) Q(f\mathbf{s}_{0\perp}) \cos\left(k\mathbf{s}_{0\perp}\cdot\boldsymbol{\rho}_0 - \phi\right) d^2\mathbf{s}_{0\perp}. \end{aligned} \tag{5.18}$$

Equivalently, $\overline{I_b}$ can be written as a superposition of three different intensity terms

$$\overline{I_b}(\mathbf{s}, \boldsymbol{\rho}_0) = I_d(\boldsymbol{\rho}_0) + I_c(\mathbf{s}) + \widetilde{I}_c(\mathbf{s}, \boldsymbol{\rho}_0), \tag{5.19}$$

where I_d, I_c and $\widetilde{I}_c$ correspond to the first, second and third integrals in Eq. (5.18), respectively. In the decomposition (5.19) of the backscattered intensity $\overline{I_b}$, the first term I_d is a diffuse background independent of the scattering angle and proportional to the total intensity of the incident beam. Using Eq. (5.13), I_d can be expressed as

$$I_d(\boldsymbol{\rho}_0) = \alpha_d \left\{ g(\mathbf{0}) + m\left|g(\boldsymbol{\rho}_0)\right| \cos\left[\psi_g(\boldsymbol{\rho}_0) - \phi\right] \right\}, \tag{5.20}$$

where ψ_g is the phase of g. Note that $\psi_g = 0$ in the case where g is real and takes the form of Eq. (5.14); however, the function g might also be complex if $Q(\mathbf{x})$ is not constant for $|\mathbf{x}| \leq R$.

The second term I_c in the right hand side of Eq. (5.19) relates to the coherent backscattering enhancement of intensity, which is observed when $m = 0$ in Eq. (5.16). Enhanced backscattering of partially coherent light has been studied previously for an incident Gaussian-type cross-spectral density [61]. This situation is equivalent to having an intensity distribution $Q(f\mathbf{s}_{0\perp})$ across the source with a Gaussian profile. Partially coherent light was shown to reduce and deform the shape of the enhancement peak as compared to the situation where a plane wave is incident upon the diffusive medium [61]. This suppression of the constructive interference of time reversed paths in the medium is due to the lack of spatial coherence in the phase of the incident field for distances longer or on the order of the transport mean free path. Only small scattering trajectories, where the field enters and exits within one coherence area, maintain their phase relationship and contribute to the coherent backscattering. The peak generated in this case has a reduced amplitude and a broader angular width. Using Eqs. (5.10) and (5.13), the intensity I_c takes the form

$$I_c(\mathbf{s}) = \frac{c}{4\pi l_s^2} \int P(\boldsymbol{\rho})\, g(\boldsymbol{\rho}) \exp[ik\mathbf{s}_\perp \cdot \boldsymbol{\rho}]\, d^2\boldsymbol{\rho}. \tag{5.21}$$

Note that $I_c(\mathbf{s})$ is real since g is Hermitian. Because the amplitude of g goes to zero as ρ increases, g acts as a filtering function in the integral (5.21). It follows that only the trajectories with entry and exit points separated by a distance ρ smaller than the width of $g(\boldsymbol{\rho})$ will contribute to the enhancement peak $I_c(\mathbf{s})$.

Finally, the third term $\widetilde{I}_c$ in the right hand side of Eq. (5.19) is an angularly modulated intensity whose amplitude of modulation is proportional to the probability $P(\boldsymbol{\rho}_0)$ for the light to enter the medium at a point $\mathbf{r}$ and exit at the location $\mathbf{r}+\boldsymbol{\rho}_0$. Substituting Eq. (5.10) into the last integral of Eq. (5.19), $\widetilde{I}_c$ can be expressed as

$$\widetilde{I}_c(\mathbf{s},\boldsymbol{\rho}_0) = \frac{m}{2}\frac{c}{4\pi l_s^2}\int_{|\mathbf{s}_{0\perp}|\leq 1}\int_{\boldsymbol{\rho}} Q(\mathbf{s}_0)\,P(\boldsymbol{\rho}) \times \cos\left[k\left(\mathbf{s}_\perp+\mathbf{s}_{0\perp}\right)\cdot\boldsymbol{\rho}\right]\cos\left(k\mathbf{s}_{0\perp}\cdot\boldsymbol{\rho}_0-\phi\right)d^2\boldsymbol{\rho}\,d^2\mathbf{s}_{0\perp}. \tag{5.22}$$

Using Eq. (5.13) in combination with the identity $2\cos(a)\cos(b)=\cos(a+b)+\cos(a-b)$ and the Hermitian property of the function g, the relation (5.22) becomes

$$\widetilde{I}_c(\mathbf{s},\boldsymbol{\rho}_0) = m\frac{c}{4\pi l_s^2}\,\mathrm{Re}\left\{\int P(\boldsymbol{\rho})\,g(\boldsymbol{\rho}-\boldsymbol{\rho}_0)\exp\left(ik\mathbf{s}_\perp\cdot\boldsymbol{\rho}+i\phi\right)d^2\boldsymbol{\rho}\right\}. \tag{5.23}$$

Defining the new variable $\mathbf{u}=\boldsymbol{\rho}-\boldsymbol{\rho}_0$, Eq. (5.23) can then be written as

$$\widetilde{I}_c(\mathbf{s},\boldsymbol{\rho}_0) = m\left|\chi(\mathbf{s},\boldsymbol{\rho}_0)\right|\cos\left[k\mathbf{s}_\perp\cdot\boldsymbol{\rho}_0+\psi(\mathbf{s},\boldsymbol{\rho}_0)+\phi\right], \tag{5.24}$$

where $\psi(\mathbf{s},\boldsymbol{\rho}_0)$ is the phase of the function χ defined as

$$\chi(\mathbf{s},\boldsymbol{\rho}_0) = \frac{c}{4\pi l_s^2}\int g(\boldsymbol{\rho})P(\boldsymbol{\rho}+\boldsymbol{\rho}_0)\exp\left[ik\mathbf{s}_\perp\cdot\boldsymbol{\rho}\right]d^2\boldsymbol{\rho}. \tag{5.25}$$

In Eq. (5.25), $g(\boldsymbol{\rho})$ acts as a filtering function which, in the integral, selects only values of $|\boldsymbol{\rho}|$ smaller than the width of g. Assuming that the variations of P are much slower than the variations of g or, in other words, g is narrow in comparison to P, then $\chi(\mathbf{s},\boldsymbol{\rho}_0)$ will depends on the value of $P(\boldsymbol{\rho})$ for $\boldsymbol{\rho}\approx\boldsymbol{\rho}_0$. Furthermore, in the limiting case where the transverse coherence of the incident field tends to zero, the function g is well approximated by a Delta

function in Eq. (5.25) and we obtain

$$\chi\left(\mathbf{s},\boldsymbol{\rho}_0\right)=\frac{c}{4\pi l_s^2}P\left(\boldsymbol{\rho}_0\right). \tag{5.26}$$

The intensity $\widetilde{I}_c$ is modulated angularly according to the cosine function in Eq. (5.24). The periodicity of the modulation is inversely proportional to $\boldsymbol{\rho}_0$ while the amplitude is given by the modulus of $\chi\left(\mathbf{s},\boldsymbol{\rho}_0\right)$, which is proportional to $P\left(\boldsymbol{\rho}_0\right)$ in the limiting case where g is a narrow function compared to P. Consequently, measuring the amplitude of the modulated intensity $\widetilde{I}_c$ leads directly to the value $P\left(\boldsymbol{\rho}_0\right)$ of the probability for the light to enter at a location $\mathbf{r}$ and exit at the point $\mathbf{r}+\boldsymbol{\rho}_0$. This result differs from the typical coherent backscattering experiment, where a single plane wave illuminates the sample. In this situation, the coherent albedo defined in Eq. (5.10) receives contributions from all the possible time reversal trajectories and, therefore, it does not provide directly the resolved probability $P\left(\boldsymbol{\rho}\right)$.

The two types of scattering trajectories contributing to the enhanced coherent peak are illustrated in Fig. 5.5(a). The intensity $I_c\left(\mathbf{s}\right)$ in Eq. (5.19) corresponds to the short-time reciprocal paths denoted as P_1. For these scattering trajectories, the light enters and exits within one speckle B and the constructive interferences generate in the far zone an intensity enhancement with the same angular width as the source. The term $\widetilde{I}_c\left(\mathbf{s},\boldsymbol{\rho}_0\right)$ relates to the longer reciprocal paths P_2 where the light enters at a speckle A and leave the medium within a speckle B located at a distance $\boldsymbol{\rho}_0$ from A. Since the fields in A and B are correlated, the waves travelling along P_2 produce, in the far zone, a modulated interference pattern

whose periodicity depends on the separation $\boldsymbol{\rho}_0$. In Fig. 5.5(b), the photon path distribution function is illustrated for the light entering and exiting the medium at two locations separated by $\boldsymbol{\rho}_0$. As the amplitude of $\boldsymbol{\rho}_0$ increases, the light probes deeper layers inside the diffusive sample, thus providing depth sensitivity to our technique.

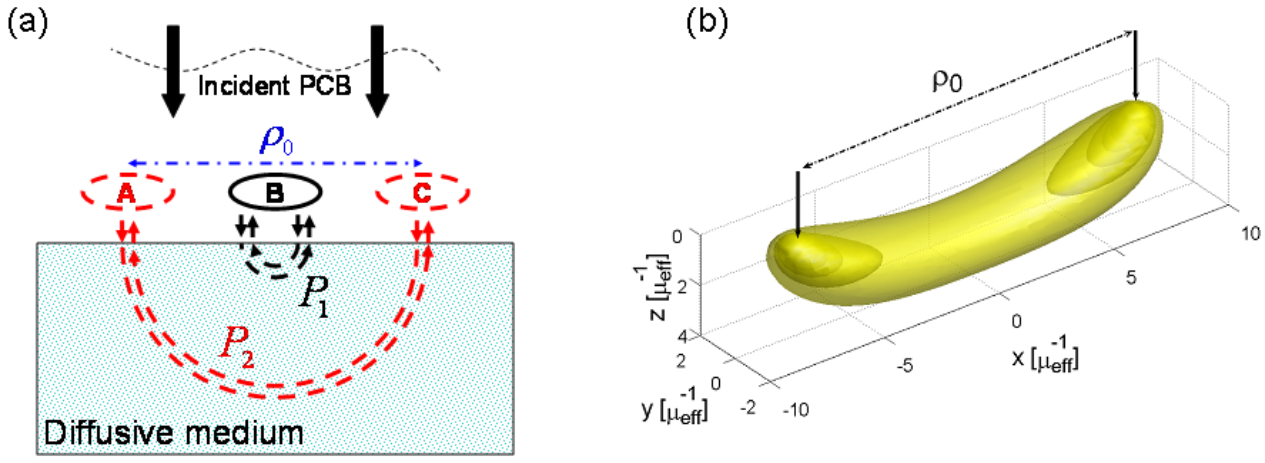

Figure 5.5: (a) Scattering paths contributing to the coherent backscattering peak when the incident light has a shaped degree of spatial coherence. (b) Photon migration path distributions for the light entering and exiting at points separated by ρ_0 [75]. The medium occupies the half space $z \geq 0$ and the coordinate units are normalized to the diffusive light migration length $L_{eff} = 1/\mu_{eff}$.

Using Eqs. (5.13) and (5.25) and substituting Eqs. (5.20), (5.21) and (5.24) into Eq. (5.19), the distribution of total backscattered intensity becomes

$$\overline{I_b}\left(\mathbf{s}, \boldsymbol{\rho}_0\right) = \alpha_d W_{\boldsymbol{\rho}_0}\left(\mathbf{0}\right) + \chi\left(\mathbf{s}, \mathbf{0}\right) + m\left|\chi\left(\mathbf{s}, \boldsymbol{\rho}_0\right)\right| \cos\left[k\mathbf{s} \cdot \boldsymbol{\rho}_0 + \psi\left(\mathbf{s}, \boldsymbol{\rho}_0\right) + \phi\right]. \tag{5.27}$$

The first term in the right hand side of Eq. (5.27) is the diffuse background intensity while the two last terms corresponds to the modulated enhanced backscattering peak. As shown in Fig. 5.6, $\overline{I_b}(\mathbf{s}, \boldsymbol{\rho}_0)$ is evaluated using Eq. (5.17) and the expression (5.12) for the albedo $\alpha(\mathbf{s}, \mathbf{s}_0)$. The calculation is performed for two configurations of the source, with the distance between correlated speckles set to $\rho_0 = 100\mu m$ and $\rho_0 = 200\mu m$, respectively. In both situations, the transport mean free path is $l_t = 100\mu m$. As expected for the case of an incident partially coherent field [61], the magnitude of the coherent peak is greatly reduced and reaches only a few percent compared to the factor two enhancement obtained when the incident field is a plane wave. Since the magnitude of $P(\boldsymbol{\rho}_0)$ decreases as ρ_0 increases, we observe a reduction of the modulation amplitude when ρ_0 is varied from $100\mu m$ to $200\mu m$.

5.3 Experimental results for a diffusive medium

To demonstrate the feasibility of the inversion procedure, an experiment was conducted on a water suspension of $200nm$ diameter polystyrene microspheres. The transport mean free path in the solution was evaluated to be $l_t = 100\mu m$. The spatially incoherent source was generated by illuminating a rotating diffuser with a coherent laser beam at the wavelength $\lambda = 532nm$. The diffuser was placed in front of a circular aperture with radius $R = 1.5mm$, which was itself located at a focal distance $f = 200mm$ from the lens L_s. The degree of spatial coherence of the incident partially coherent beam (PCB) was shaped using the interferometer illustrated in Fig. 5.3 and the direction of linear polarization of the beam

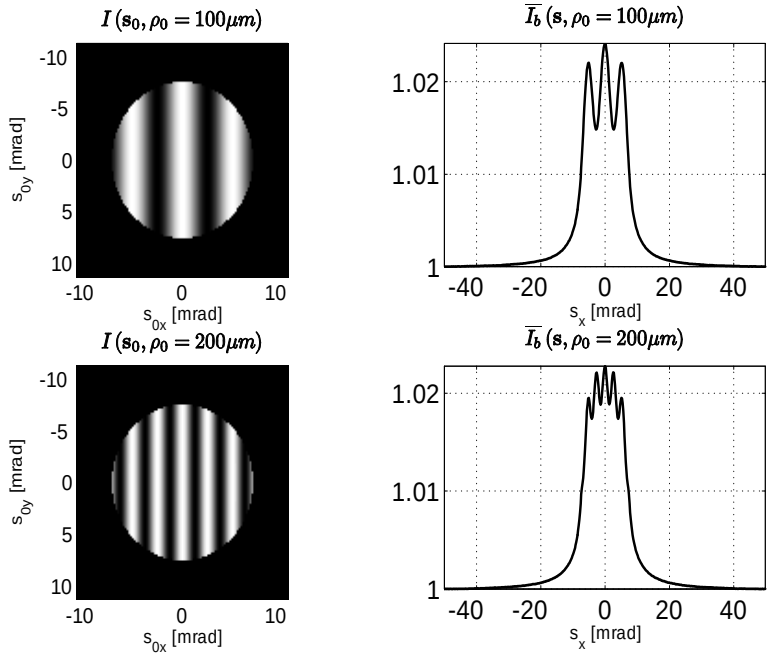

Figure 5.6: Distribution of backscattered intensity $\overline{I_b}(\mathbf{s}, \boldsymbol{\rho}_0)$ normalized to the background intensity. The calculation is performed for an incident field characterized by the angular distribution $I(\mathbf{s}_0, \boldsymbol{\rho}_0)$ with $\rho_0 = 100\mu m$ (top) and $\rho_0 = 200\mu m$ (bottom). The diffusive medium has a transport mean free path $l_t = 100\mu m$ while the source, with a radius set to $R_s = 1.5mm$, is located at a focal distance $f = 200mm$ from L_s.

was set by the polarizer P_2. The experimental angular intensity spectrum of the PCB is represented in Fig. 5.7 for the interferometer detuned such that $\rho_0 = 220\mu m$.

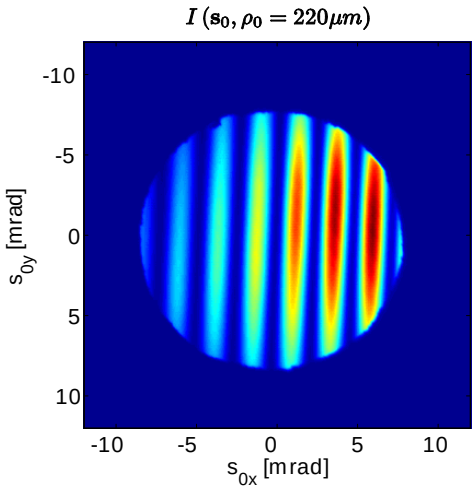

Figure 5.7: Angular intensity distribution $I(\mathbf{s}_0, \boldsymbol{\rho}_0)$ of the incident partially coherent beam when the distance between correlated speckle is $\rho_0 = 220\mu m$.

As illustrated in Fig. 5.8, the PCB goes through a non polarizing beam splitter NPBS before illuminating the scattering medium. The diameter of the beam impinging on the cuvette was around $2cm$. The reflected part of the PCB by the NPBS was dumped so that it would not to affect the measurements. Furthermore, to avoid a direct reflection from the air-glass interface, the $10mm$ long cuvette containing the water suspension was slightly titled. After reflection from the NPBS, the scattered light was collected by the lens L_c with focal length $f_c = 200mm$. Using a half-wave plate $\lambda/2$ and a polarizing beam splitter PBS, the scattered light was separated into a co-polarized and a cross-polarized channel. In the co-polarized channel, the intensity profile $\overline{I_b}(\mathbf{s}, \boldsymbol{\rho}_0)$ of the coherent backscattering peak

was measured along the axis **x** in the focal plane of L_c with a photomultiplier tube (PMT) connected to a scanning fiber. Located away from the focal plane of L_c in the cross-polarized channel, another PMT acted as a reference detector and recorded the variations of the total intensity I_{ref}. The intensities recorded were averaged over the ensemble of realizations by setting the PMTs' integration time much larger than the time scale of the fluctuations of both the scattering medium and the PCB. In addition to the time averaging, the extended size of the beam incident on the cuvette provided also a spatial averaging.

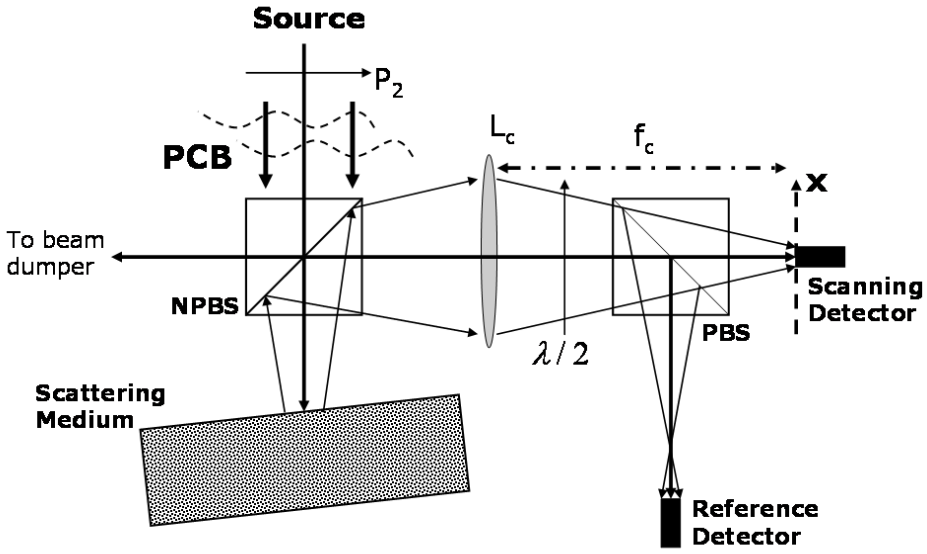

Figure 5.8: Schematic of the experimental detection setup used for enhanced backscattering with shaped spatially partially coherent light.

The measured intensity $\overline{I_b}(s_x, \boldsymbol{\rho}_0)$ was divided by I_{ref} in order to eliminate unwanted fluctuations of intensity, which might be caused by fluctuations in the power of the laser, vibrations of the rotating diffuser, or changes in the particles density due to uneven mixing.

Moreover, since the different collecting optics were all tilted in order to avoid undesired reflections, the angular intensity response was not constant across the considered range $\pm 10 mrad$. To compensate for this effect, the detector was scanned in the focal plane of L_c when the source was not modulated, i.e. $m = 0$. The measured intensity $\overline{I_b}(s_x)\big|_{m=0}$ served as a baseline and the corrected backscattered intensity profile became

$$\overline{I_b}(s_x, \boldsymbol{\rho}_0)\big|_{corr} = \frac{\overline{I_b}(s_x, \boldsymbol{\rho}_0)}{I_{ref}\ \overline{I_b}(s_x)\big|_{m=0}}. \tag{5.28}$$

The modulated intensity $\widetilde{I_c}(s_x, \boldsymbol{\rho}_0)$ is then proportional to $\overline{I_b}(s_x, \boldsymbol{\rho}_0)\big|_{corr} - \overline{I_s}$, where $\overline{I_s}$ is the average of $\overline{I_b}(s_x, \boldsymbol{\rho}_0)\big|_{corr}$ over s_x.

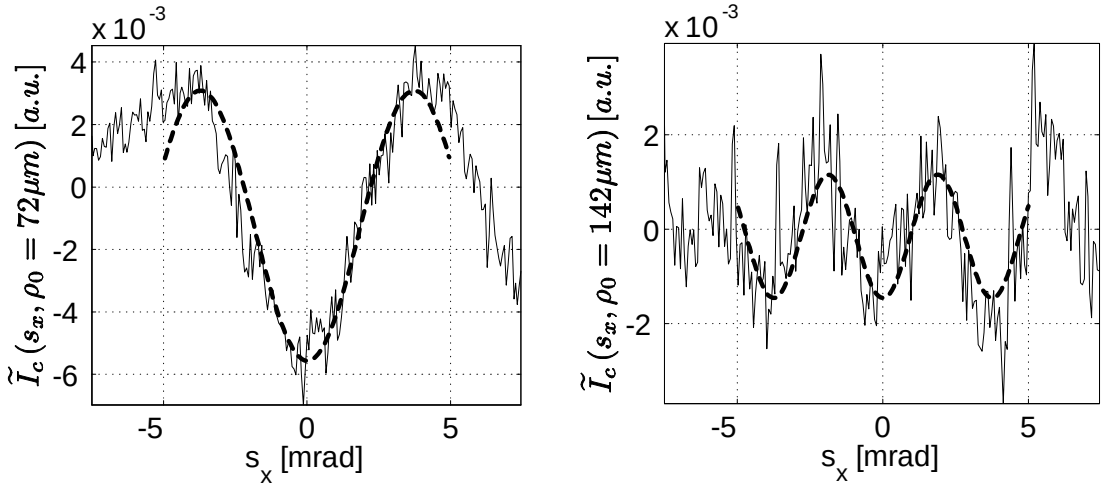

Figure 5.9: (solid line) Modulated part $\widetilde{I_c}(s_x, \boldsymbol{\rho}_0)$ of the angular scattered intensity measured for $\rho_0 = 72\mu m$ and $\rho_0 = 142\mu m$, respectively. (dashed lined) Fit of the experimental data with a cosine function in order to determine the amplitude of the modulation.

The intensities from the two detectors were recorded for different separations ρ_0 between correlated speckles. The resulting intensity $\widetilde{I_c}(s_x, \boldsymbol{\rho}_0)$ is shown in Fig. 5.9 for $\rho_0 = 72\mu m$ and

$\rho_0 = 142\mu m$, respectively. The amplitude $|\chi(\mathbf{s}, \boldsymbol{\rho}_0)|$ of the modulation was deduced by fitting the data with the function $A\cos(ks_x\rho_0 + \theta) + B$, where A needs to be determined, and, B and θ are unknown parameters which compensate for a possible shift of the measurements. The fitting functions correspond to the dashed curves in Fig. 5.9 and the results for the amplitude A are illustrated in Fig. 5.10. The validity of the experimental data was checked by comparing it with the analytical solution for $P(\rho)$ obtained from the Fourier transform of Eq. (5.10) using Eq. (5.12). The numerical calculation was performed for $l_t = 70$, 100 and $130\mu m$ and the results were all multiplied by the same constant factor in order to compare the curves with the normalized experimental data.

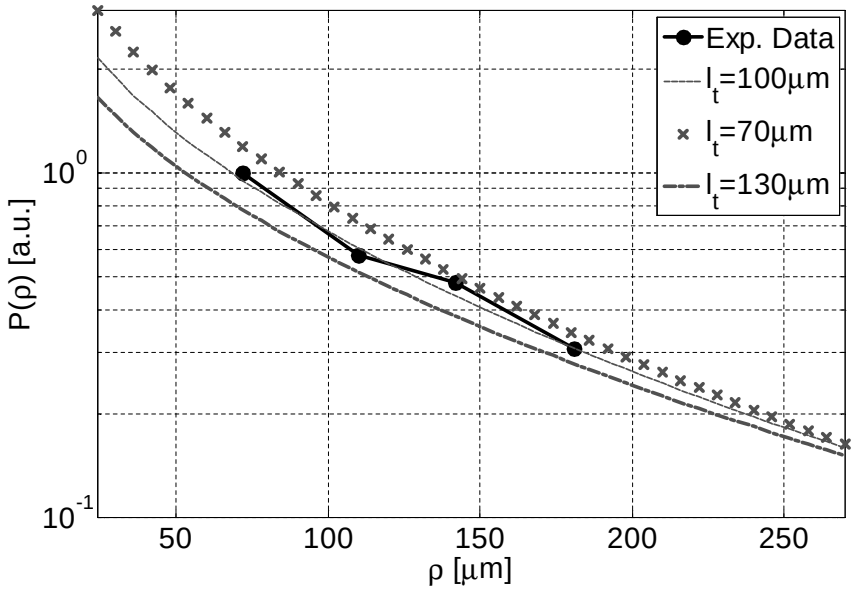

Figure 5.10: Experimental measurement of $P(\rho)$ as a function of the transverse separation ρ. The dashed curves correspond to the analytical solution for $P(\rho)$ obtained from Eqs. (5.10) and (5.12) for $l_t = 70$, 100 and $130\mu m$.

Figure 5.10 illustrates the good agreement between the analytical and experimental data, demonstrating that the probability of radial intensity distribution $P(\rho)$ can be retrieved by shaping the degree of spatial coherence of the illuminating field. The noise of the photon counting detectors was close to shot noise; consequently, the dynamic range of the measurement was limited by the maximum frequency rating of the PMTs. However, the intensity resolution can be improved using a fast detector and modulating the direction of detection $\mathbf{s}$ with, for instance, a scanning mirror.

5.4 Conclusion

In this chapter, we have demonstrated that shaping the degree of spatial coherence of the incident light enables the selection of specific photon trajectories in a multiple scattering medium. Contrary to recent techniques using a low temporal coherence illumination [17] or an incident vortex beam [2] where only shallow layers are being probed, our procedure can selectively target both shallow and deep layers, which are associated with short and long scattering paths, respectively. The principle of enhanced backscattering with shaped partially coherent light is similar to the sensing procedure where the light emitted from a source fiber is collected by a detector fiber, both fibers being located at the surface of a sample and separated by an adjustable distance [76]. In our technique however, there is an inherent advantage due to the significant spatial averaging obtained by using an extended incident beam where each pair of correlated speckles behaves as a pair of source-detector

fibers. A more accurate measurement of the scattering parameters is then expected. The depth resolved capability of our procedure may be of great interest for structural studies of multilayered or anisotropically inhomogeneous materials which are usually encountered in biomedical applications.

Finally, it should be noted that the correlated speckles composing the partially coherent incident field had the same polarization in our experiment. Using a similar polarized Sagnac interferometer, correlated speckles with orthogonal states of polarization could also be generated. Time reversal paths with cross-polarized entering and exiting photons would then be preferentially excited, thus, revealing the polarized nature of the photon diffusion. Other coherent manifestations of the localization of light, such as long-range correlations or the memory effect, also appear in multiple scattering media in both the forward and backward directions [67]. Following the same principle introduced in this chapter, an incident field with shaped degree of spatial coherence could be used to enhance the influence of specific light trajectories. However, these coherent effects depend on the probability of scattering paths crossing, which is extremely small when the transport mean free path is much larger than the wavelength. Localization of light is yet to be observed and this subject remains a very active research topic [77].

In both variable coherence tomography and the coherent backscattering technique presented in this chapter, the resolution was determined by the average size of the speckle which is typically larger than 10λ in the transversal dimension. By increasing the angular spec-

trum of the incident field, we will demonstrate in the next chapter that the spatial correlation properties of a medium can be reconstructed with subwavelength resolution.

CHAPTER 6

VARIABLE COHERENCE SCATTERING MICROSCOPY

Optical techniques for imaging and structural characterization are widespread. In the preceding chapters, we have demonstrated a number of sensing methods based on using the spatial coherence properties of optical radiations. In general, imaging techniques rely on propagating fields and, therefore, their spatial resolution is limited by the radiation's wavelength. Recent advances in near-field optics have led to the development of many microscopy techniques for achieving imaging with a spatial resolution beyond the classical diffraction limit. Atomic-force microscopy, near-field scanning optical microscopy [19] and photon scanning tunneling microscopy [78] have been successful in recovering images of subwavelength objects. However, this improved resolution comes at the expense of the most appealing characteristic of optical imaging, namely its parallel processing capability. Because a scanning probe operation is required to build up the image point by point, the approach is time consuming and, moreover, it is practically restricted to imaging of very small areas.

In many situations of practical interest, where conventional imaging is irrelevant, developing a tomographic procedure with subwavelength resolution and being able of measuring the second-order statistics of optical properties can be of considerable interest. This could be especially beneficial in determining structural organizational information about objects such as large nanostructure arrays. For instance, correlation measurements on monolayers of

biological cells have been recently performed demonstrating the increased medical interest in investigating the morphology of subcellular structures as well as long-range correlations between cells [79]. In this last experiment, however, the proposed method was model dependant and could hardly be applied to arbitrary scattering objects. Nevertheless, the development of nondestructive microscopic techniques is of major interest for characterizing biological media. In this context, it is worth mentioning that total internal reflection tomography [80] is an interesting approach which, unfortunately, requires challenging measurements of the optical fields. We note that an alternative method [81] based on power extinction measurements has been proposed but not demonstrated.

In this chapter, we introduce and demonstrate the principle of variable coherence scattering microscopy (VCSM). In this novel microscopy, the object under test is probed by an evanescent field which has its spatial coherence properties adjustable at subwavelength scales. Our results are remarkable in the sense that subwavelength resolution is achieved from simple far zone intensity measurements. Notably, the technique we are illustrating here can be implemented without any moving parts for both illuminating the sample and detecting the scattered light.

6.1 Spatial coherence shaping of an evanescent field

We have demonstrated in Chapter 4 that the degree of spatial correlation of a quasi-homogeneous scattering medium can be retrieved from simple intensity measurements [60].

The resolution of the reconstruction was limited by the size of the coherence volume, whose dimensions can exceed many wavelengths in the case of a propagating beam-like field. Exploiting the high frequency content of evanescent waves, a spatial resolution beyond the diffraction limit can be achieved [80, 82]. In the newly proposed method, an ensemble of evanescent waves are incoherently superposed in order to generate a field of speckles smaller than the wavelength. Moreover, in this field, the correlation properties can be adjusted between speckles separated by distances as large as several tens of wavelengths.

Let us consider an incoherent superposition of evanescent plane waves defined by their complex wave vectors $\mathbf{k} = (\mathbf{q}, i\gamma)$ where $\mathbf{q}$ is the transverse part and $\gamma = \sqrt{\mathbf{q}^2 - k_0^2}$. Evanescent waves are generated at the interface $(x, y, z = 0)$ between air $(z \geq 0)$ and a dielectric medium $(z < 0)$ with a refractive index n. Consequently, the modulus of the transverse wave vector $\mathbf{q}$ is confined to the region Γ defined by $k_0 \leq |\mathbf{q}| \leq nk_0$. Let us further consider that the intensity of the evanescent field is modulated in the $\mathbf{k}$ domain so that the plane wave defined by the transverse wave vector $\mathbf{q}$ has the intensity

$$I_e(\mathbf{q}) = \frac{1}{2} Q(\mathbf{q}) \left(1 + m \cos\left[\mathbf{q} \cdot \boldsymbol{\Delta\rho}_0 - \phi\right]\right), \tag{6.1}$$

where m is a modulation factor taking values between 0 and 1, and $Q(\mathbf{q})$ is positive if $\mathbf{q} \in \boldsymbol{\Gamma}$ and equals zero otherwise. The periodicity of the intensity modulation is adjusted by the value of the vector $\boldsymbol{\Delta\rho}_0$, while the phase ϕ is determined by the condition $\mathbf{q} \cdot \boldsymbol{\Delta\rho}_0 = 0$.

Substituting Eq. (6.1) into Eqs. (2.21) and (2.22), the cross-spectral density of the field resulting from the incoherent superposition of evanescent plane waves with intensity $I_e(\mathbf{q})$

takes the form

$$W^{(i)}(\mathbf{r}_1, \mathbf{r}_2) = \chi(\mathbf{\Delta\rho}, z_1, z_2) + \frac{m}{2}\exp[-i\phi]\,\chi(\mathbf{\Delta\rho} - \mathbf{\Delta\rho}_0, z_1, z_2) \\ + \frac{m}{2}\exp[i\phi]\,\chi(\mathbf{\Delta\rho} + \mathbf{\Delta\rho}_0, z_1, z_2), \tag{6.2}$$

where z_1 and z_2 are the projections of $\mathbf{r}_1$ and $\mathbf{r}_2$ along the z axis, and $\mathbf{\Delta\rho} = \mathbf{r}_{\perp 1} - \mathbf{r}_{\perp 2}$ with $\mathbf{r}_\perp$ being the projection of $\mathbf{r}$ onto the (x, y) plane. When the modulation factor m equals zero in Eq. (6.1), the incident field is spatially coherent in a volume defined by the function χ:

$$\chi(\mathbf{\Delta\rho}, z_1, z_2) = \frac{1}{2}\iint_{-\infty}^{\infty} Q(\mathbf{q})\exp[-\gamma(z_1 + z_2)]\exp[-i\mathbf{q}\cdot\mathbf{\Delta\rho}]\,d^2\mathbf{q}. \tag{6.3}$$

The cross-spectral density $W^{(i)}(\mathbf{r}_1, \mathbf{r}_2)$ of the evanescent field in the plane of the interface $z = 0$ is illustrated in Fig. 6.1. When the intensity $I_e(\mathbf{q})$ is modulated, i.e. when m is greater than zero, a secondary peak of coherence arises at a position $\mathbf{\Delta\rho}_0$ from the main coherence peak centered at $\mathbf{\Delta\rho} = \mathbf{0}$. The separation $\mathbf{\Delta\rho}_0$ can be continuously adjusted by varying the intensity $I_e(\mathbf{q})$. The incident field induces coherent scattering from regions in the medium which are separated by a distance of several wavelengths corresponding to the norm $|\mathbf{\Delta\rho}_0|$. Due to the evanescent nature of the incident field, only the high frequency components of the complex susceptibility corresponding to subwavelength features are excited during the scattering process.

For subwavelength structures and optically thin media it is appropriate to regard the scattering as being weak and therefore the first-order Born approximation can be used. The intensity scattered in the direction of the wave vector $\mathbf{k}_s$ and at a distance r in the far zone

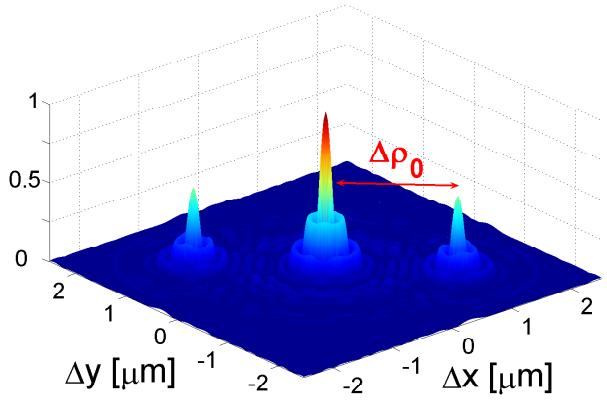

Figure 6.1: Normalized cross-spectral density of the evanescent field as evaluated from Eq. (6.3) for $z_1 = z_2 = 0$, $Q(\mathbf{q}) = 1$ and $k_0 \leq |\mathbf{q}| \leq nk_0$.

of the medium is given by Eq. (2.38)

$$I^{(s)}(\mathbf{k}_s) = \frac{k_0^2}{r^2} \iint_D C(\mathbf{r}_1, \mathbf{r}_2) W^{(i)}(\mathbf{r}_1, \mathbf{r}_2) \exp\left[i\mathbf{k}_s \cdot (\mathbf{r}_1 - \mathbf{r}_2)\right] d^3\mathbf{r}_1 d^3\mathbf{r}_2, \tag{6.4}$$

where $C(\mathbf{r}_1, \mathbf{r}_2)$ is the spatial correlation of the complex susceptibility $\eta(\mathbf{r})$ defined in Eq. (2.36):

$$C(\mathbf{r}_1, \mathbf{r}_2) = \langle \eta^*(\mathbf{r}_1) \eta(\mathbf{r}_2) \rangle_\eta . \tag{6.5}$$

From Eq. (6.2), one can see that the cross-spectral density $W^{(i)}(\mathbf{r}_1, \mathbf{r}_2)$ depends only on the transverse separation $\boldsymbol{\Delta\rho} = \mathbf{r}_{\perp 1} - \mathbf{r}_{\perp 2}$. It is therefore relevant to consider a quasi-homogeneous medium [4] with transversely invariant statistical properties, namely $C(\mathbf{r}_1, \mathbf{r}_2) = A\left[(\mathbf{r}_{\perp 1} + \mathbf{r}_{\perp 2})/2\right] \mu(\boldsymbol{\Delta\rho}, z_1, z_2)$ where μ is the degree of spatial correlation of the complex susceptibility and $A(\mathbf{r}_\perp) = C(\mathbf{r}_\perp, \mathbf{r}_\perp)$ is the second moment of C in the plane $z = 0$. The function $A(\mathbf{r}_\perp)$ is assumed to vary more slowly with $\mathbf{r}_\perp$ than the variation of $\mu(\boldsymbol{\Delta\rho}, z_1, z_2)$

with $\mathbf{\Delta\rho}$. From Eqs.(6.4) and (6.2), it follows that the scattered intensity depends on $\mathbf{\Delta\rho}_0$ as

$$I^{(s)}(\mathbf{k}_s, \mathbf{\Delta\rho}_0) = G(\mathbf{k}_s, \mathbf{0}) + m\,|G(\mathbf{k}_s, \mathbf{\Delta\rho}_0)| \cos\left[\mathbf{k}_{s\perp} \cdot \mathbf{\Delta\rho}_0 - \phi + \phi_G(\mathbf{k}_s, \mathbf{\Delta\rho}_0)\right], \tag{6.6}$$

with $\phi_G(\mathbf{k}_s, \mathbf{\Delta\rho}_0)$ being the argument of the function $G(\mathbf{k}_s, \mathbf{\Delta\rho}_0)$ defined as

$$G(\mathbf{k}_s, \mathbf{\Delta\rho}_0) = \frac{k_0^2}{r^2} A_0 \iint_{-\infty}^{\infty} \iint_{0}^{z_m} \mu\left(\mathbf{\Delta\rho} - \mathbf{\Delta\rho}_0, z_1, z_2\right) \chi\left(\mathbf{\Delta\rho}, z_1, z_2\right) \tag{6.7}$$

$$\times \exp\left[i\mathbf{k}_{s\perp} \cdot \mathbf{\Delta\rho} + ik_{sz}\left(z_1 - z_2\right)\right] d^2\mathbf{\Delta\rho} dz_1 dz_2.$$

In Eq. (6.7), z_m is the longitudinal extend of the medium. The integration over $\mathbf{\Delta\rho}$ can be extended to infinity because, in practice, the transverse dimensions of the object are much larger than both the transverse width of $\chi\left(\mathbf{\Delta\rho}, z_1, z_2\right)$ and the range of values taken by $|\mathbf{\Delta\rho}|$ for which $\mu\left(\mathbf{\Delta\rho}, z_1, z_2\right)$ is nonzero. The proportionality factor A_0 is defined as $A_0 = \int A\left(\mathbf{r}_\perp\right) d^2\ \mathbf{r}_\perp$ and is proportional to the transverse area of the object if A is constant.

Equation (6.6) along with Eq. (6.7) constitutes the basis of the variable coherence scattering microscopy. As the coherence properties of the illuminating evanescent field are varied, the scattered intensity in any given direction fluctuates accordingly to the correlation properties of the medium. Conventional envelope and phase reconstruction can be used to recover $G(\mathbf{k}_s, \mathbf{\Delta\rho}_0)$ and to infer information about the degree of spatial correlation μ. Although a complete inversion of Eq. (6.7) requires *a priori* knowledge about the z dependence of $\mu\left(\mathbf{\Delta\rho}, z_1, z_2\right)$, some practical situations could lead to a simpler expression of Eq. (6.7), which can be readily inverted. This is indeed the case if the correlation function is independent of z or if the sample is much thinner than the wavelength and no correlation along

the z direction can be assumed. However, even in the general case, structural informations about the sample can be obtained from the expression of $G(\mathbf{k}_s, \boldsymbol{\Delta\rho}_0)$ as we will show in the next section.

6.2 Experimental results on a monolayer of microspheres

To demonstrate the feasibility of the inversion procedure, a proof-of concept experiment has been conducted. In order to generate evanescent waves with transverse wave vectors $\mathbf{q} \in \boldsymbol{\Gamma}$, we used the spherical geometry shown in Fig. 6.2. The light emitted by a hemispherical secondary source H is collected by a hemisphere prism L concentric with H. The dimensions of H and L are such that the surface of the source lays in the focal surface of the prism. The radius and the refractive index of L are respectively $R_L = 21.5mm$ and $n = 1.78$. The intensity distribution across the source is modulated according to Eq. (6.1). Consequently, the light originating from a point on the spherical source H generates an evanescent plane wave at the planar interface (x, y) of the prism. The spatial incoherence of the source is obtained by slightly vibrating H with a much smaller time scale than the duration of the intensity measurements.

A frequency doubled Nd:Yag laser ($\lambda = 532nm$) and a Sagnac interferometer were used to generate the fringe pattern which was then projected onto a hemispherical diffuser used as a secondary source. In order to adjust the modulation frequency $\boldsymbol{\Delta\rho}_0$ of the intensity $I_e(\mathbf{q})$ in Eq. (6.1), the spacing of the fringes was varied by translating one of the mirrors of

the Sagnac interferometer. The light scattered by the sample in the z direction, i.e. $\mathbf{k}_{s\perp} = 0$, is collected by a multimode fiber located in the focal plane of a 10x microscope objective. The objective was placed above the object for convenience but the detection could have been done as well from below as represented in Fig. 6.2. The diameter of the field of view seen by the fiber was around $1mm$.

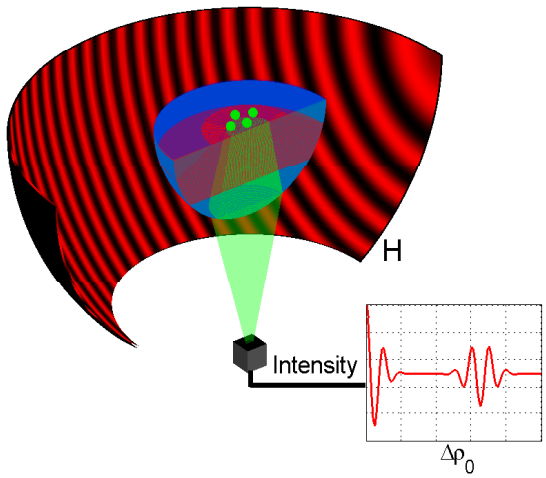

Figure 6.2: Schematic of the setup used to generate evanescent waves with transverse wave vectors $k_0 \leq |\mathbf{q}| \leq nk_0$.

The scattering system exemplified here is a monolayer of polystyrene microspheres of diameter $d = 0.97\mu m$ and index of refraction $n_s = 1.59$. Using conventional imaging analysis, we estimated the packing fraction to be $\eta = 0.7$ by taking several microscope images of the sample. The angular light scattered from such a monolayer of spheres is well described in the single scattering approximation [83] and it can be expressed as the product between the

single particle phase function $P(\mathbf{K})$ and the structure factor $S(\mathbf{K})$ describing the spheres' arrangement in the monolayer. We denote as $I^{(m)}(\mathbf{k}_{sz}, \mathbf{q}) = P(\mathbf{k}_{sz}, \mathbf{q}) S(\mathbf{q}) Q(\mathbf{q})$ the intensity scattered in the direction z by the monolayer of spheres illuminated by an evanescent waves with incident wave vector $\mathbf{k} = (\mathbf{q}, i\gamma)$ and intensity $Q(\mathbf{q})$. The expression for the scattered intensity in Eq. (6.4) establishes the following relationship between $I^{(m)}(\mathbf{k}_{sz}, \mathbf{q})$ and an effective spatial correlation function C describing the medium:

$$I^{(m)}(\mathbf{k}_{sz}, \mathbf{q}) = \frac{k_0^2}{r^2} \int_D \int_D C(\mathbf{r}_1, \mathbf{r}_2) W_p^{(i)}(\mathbf{r}_1, \mathbf{r}_2) \exp[ik_{sz}(z_1 - z_2)] d^3\mathbf{r}_1 d^3\mathbf{r}_2. \tag{6.8}$$

In formula (6.8), $W_p^{(i)}(\mathbf{r}_1, \mathbf{r}_2) = Q(\mathbf{q}) \exp[-i\mathbf{q}\cdot(\mathbf{r}_{\perp 1} - \mathbf{r}_{\perp 2})] \exp[-(z_1 + z_2)\gamma]$ represents the cross-spectral density of an evanescent plane wave with incident wave vector $\mathbf{k} = (\mathbf{q}, i\gamma)$ and intensity $Q(\mathbf{q})$. Using Eqs. (6.3), (6.7), (6.8) and the expression for $W_p^{(i)}$, the function $G(\mathbf{k}_{sz}, \boldsymbol{\Delta\rho}_0)$ can be regarded as the Fourier transform of $I^{(m)}(\mathbf{k}_{sz}, \mathbf{q})$ with respect to $\mathbf{q}$, namely

$$G(\mathbf{k}_{sz}, \boldsymbol{\Delta\rho}_0) = \int_{-\infty}^{\infty} I^{(m)}(\mathbf{k}_{sz}, \mathbf{q}) \exp(-i\mathbf{q} \cdot \boldsymbol{\Delta\rho}_0) d^2\mathbf{q}. \tag{6.9}$$

Being proportional to $Q(\mathbf{q})$, $I^{(m)}(\mathbf{k}_{sz}, \mathbf{q})$ vanishes for $\mathbf{q} \notin \boldsymbol{\Gamma}$ in the previous integral. Moreover, since the function $I^{(m)}(\mathbf{k}_{sz}, \mathbf{q})$ is real and even with respect to $\mathbf{q}$, $G(\mathbf{k}_{sz}, \boldsymbol{\Delta\rho}_0)$ is real and, using Eq. (6.6), the intensity $I^{(s)}(\mathbf{k}_{sz}, \boldsymbol{\Delta\rho}_0)$ scattered in the z direction becomes

$$I^{(s)}(\mathbf{k}_{sz}, \boldsymbol{\Delta\rho}_0) = G(\mathbf{k}_{sz}, \mathbf{0}) + mG(\mathbf{k}_{sz}, \boldsymbol{\Delta\rho}_0) \cos(\phi). \tag{6.10}$$

It follows that $I^{(m)}(\mathbf{k}_{sz}, \mathbf{q})$ can be determined by Fourier transforming $G(\mathbf{k}_{sz}, \boldsymbol{\Delta\rho}_0)$ obtained from the intensity data $I^{(s)}(\mathbf{k}_{sz}, \boldsymbol{\Delta\rho}_0)$. Since the function $I^{(m)}(\mathbf{k}_{sz}, \mathbf{q})$ depends only

on the modulus $|\mathbf{q}|$, the procedure is further simplified using a Hankel transform of zero order and the inversion formula becomes

$$I^{(m)}\left(\mathbf{k}_{sz},\mathbf{q}\right)=\frac{1}{m\cos\left(\phi\right)}\int_{0}^{\infty}\left[I^{(s)}(\mathbf{k}_{sz},\Delta\rho_{0})-G(\mathbf{k}_{sz},\mathbf{0})\right]J_{0}\left(q\Delta\rho_{0}\right)\Delta\rho_{0}d\Delta\rho_{0}, \tag{6.11}$$

where $G(\mathbf{k}_{sz},\mathbf{0})$ is the value of the scattered intensity for large $\Delta\rho_0$ where the function $G(\mathbf{k}_{sz},\boldsymbol{\Delta\rho}_0)$ is assumed to vanish.

$I^{(s)}(\mathbf{k}_{sz},\Delta\rho_0)$ was experimentally measured for $\Delta\rho_0$ ranging from 0 to $30\mu m$ and $I^{(m)}\left(\mathbf{k}_{sz},\mathbf{q}\right)$ was obtained as a the result of the Hankel transform according to Eq. (6.11). The result of this procedure is presented in Fig. 6.3 for q ranging from $k_0=11.8nm^{-1}$ to $nk_0=21nm^{-1}$. Also shown as an inset is the normalized intensity $I^{(s)}$ obtained experimentally. In order to check the validity of the experimental data, a comparison was made with available analytical expressions for $P\left(\mathbf{k}_{sz},\mathbf{q}\right)$, $S\left(\mathbf{q}\right)$ and $Q\left(\mathbf{q}\right)$. The scattering of an evanescent wave from a homogeneous sphere including multiple scattering components was calculated in terms of the partial wave expansion [81]

$$P\left(\mathbf{k}_{sz},\mathbf{q}\right)=\exp\left(-2z_{s}\sqrt{\mathbf{q}^{2}-k_{0}^{2}}\right)\left|\sum_{l=0}^{\infty}\left(2l+1\right)A_{l}P_{l}\left(\widehat{\mathbf{k}}_{sz}\cdot\widehat{\mathbf{k}}\right)\right|^{2}, \tag{6.12}$$

where P_l are the Legendre polynomials, $\widehat{\mathbf{k}}$ and $\widehat{\mathbf{k}}_{sz}$ are the normalized incident and scattered wave vectors and A_l are the partial wave expansion coefficients for a sphere of diameter $d=0.97\mu m$ and index of refraction $n_s=1.59$. The structure factor $S\left(\mathbf{q}\right)$ was computed using the Percus-Yevick approximation for the system of hard disks with a packing fraction $\eta=0.7$ [84]. Since the hemispherical source H emits light isotropically, the intensity $Q\left(\mathbf{q}\right)$ of the

evanescent plane waves illuminating the sample is simply proportional to the corresponding Fresnel transmission coefficient for unpolarized light [85].

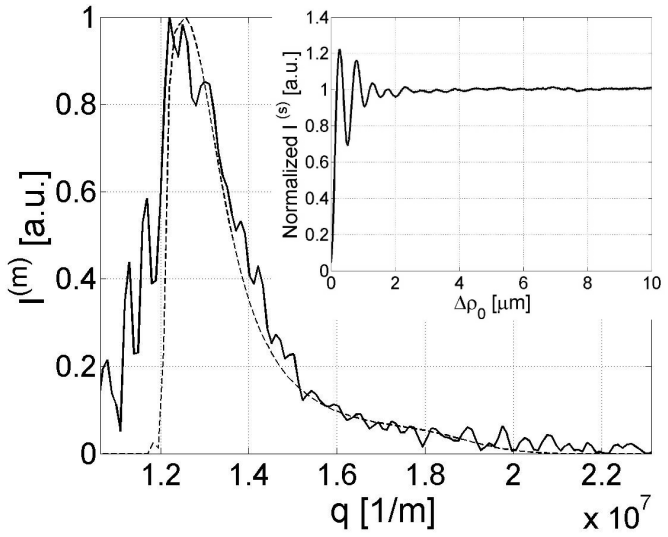

Figure 6.3: High spatial frequency content of the intensity $I^{(m)}(\mathbf{k}_{sz}, \mathbf{q})$ scattered by a monolayer of $0.97\mu m$ diameter particles. The solid line represents the results of the Hankel transform of the measured intensity $I^{(s)}(\mathbf{k}_{sz},\Delta\rho_0)$ whereas the dashed line corresponds to the analytical result obtained as explained in the text. The inset shows part of the normalized intensity $I^{(s)}(\mathbf{k}_{sz},\Delta\rho_0)$ obtained experimentally for $0 \leq \Delta\rho_0 \leq 10\mu m$.

The good agreement between the experimental and analytical data showed in Fig. 6.3 clearly demonstrates that the high spatial frequency content of the scattered intensity can be retrieved using VCSM. Our technique is therefore sensitive to the structural properties of subwavelength features over an extended field of view, which, in our experiment, had a diameter of $1mm$ but could, in principle, be even larger. Because the light scattered from the sample can be detected from either above or below the sample, as shown in Fig. 6.2,

VCSM can be easily integrated with other types of microscopies for a more comprehensive measurement capability.

6.3 Conclusion

In this chapter, we introduced the concept of a novel microscopy technique based on controlling the spatial coherence properties of the illuminating field at subwavelength scale. We have demonstrated that the high spatial frequency components of the sample can be reconstructed from simple far zone intensity measurements. Most importantly, subwavelength resolution is obtained over a very large field of view without using a scanning probe. Contrary to standing-wave total internal reflection fluorescence imaging [86], VCSM does not require fluorophore tagging of biological specimens. We also note that our technique is implemented without any moving parts, which makes VCSM an ideal candidate for high throughput sensing and screening for various applications in biology and medicine.

The method introduced in this chapter is of general importance because it demonstrates a modality of solving an inverse problem based only on far-field intensity data while achieving a resolution better than the radiation's wavelength. Finally, we would like to point out that, in the tomographic procedures introduced in this chapter and also in Chapter 4, the autocorrelation of the complex susceptibility η was retrieved. While, in these methods, the amplitude of the Fourier transform of η can be calculated, the phase is practically

lost. However, we will demonstrate in the following chapter that both amplitude and phase information can still be recovered by using a beam of adjustable degree of spatial coherence.

CHAPTER 7

CORRELATED IMAGING WITH SHAPED SPATIALLY PARTIALLY COHERENT LIGHT

Much attention has been paid recently to the correlated imaging protocol in which the image of an object is retrieved non-locally by correlating the intensity fluctuations of two spatially correlated beams. The first experimental demonstration of two-photon imaging [89] and Fourier imaging [90] involved a pair of entangled photons generated by spontaneous down-conversion. In these experiments, one of the photon was directed in the path containing an object and a fixed detector, while, in the path of the other photon, a detector was scanned in order to reproduce a sharp image of the object or its Fourier transform. Ghost imaging was shown to persist for arbitrary down-conversion efficiency [91] and, more interestingly, it was experimentally demonstrated that classical incoherent sources could be used to mimic the procedure of quantum coincidence imaging [92, 93, 94]. Applications of this technique can be found in x-ray diffraction since a lensless Fourier-transform image can be obtained using a spatially incoherent source [95].

However, in both correlated imaging and Fourier imaging, only the modulus of the transmittance or the amplitude of the spatial frequencies of the object are measured. One procedure has been successful in recovering phase information [96], yet it requires a cumbersome homodyne detection. In this chapter, we propose and demonstrate an alternative way to ob-

tain both amplitude and phase information about the spatial frequencies of an object. Using a shaped partially coherent beam and measuring the correlation of intensity fluctuations, we show that the complex Fourier transform of an object can be recovered.

7.1 Correlated imaging

7.1.1 Correlated imaging with a classical source

Let us consider the experimental setup sketched in Fig. 7.1. The light emitted by a quasi-monochromatic and spatially incoherent source S, located in the focal plane of a lens L_s, is separated in two distinct optical paths by a non-polarizing beam splitter BS. One path contains an object of complex transmittance T located at a distance h from L_s. A fixed pinhole detector D_1 is placed on the optical axis at a distance d from the object. In the reference path, another pinhole detector D_2 is scanned in the transverse plane located at a distance $d + h$ from L_s. The outputs of the two intensity detectors are multiplied and the resulting signal is proportional to the second-order intensity correlation function

$$G^{(2)}(\mathbf{r}_1, \mathbf{r}_2) = \langle I(\mathbf{r}_1) I(\mathbf{r}_2) \rangle , \tag{7.1}$$

where $I(\mathbf{r})$ is the intensity at position $\mathbf{r}$ and $\langle ... \rangle$ denotes the ensemble average over the field realizations. Expressing the intensity I as a sum of its average value and a fluctuating part

such that $I = \langle I \rangle + \Delta I$, Eq. (7.1) becomes

$$G^{(2)}(\mathbf{r}_1, \mathbf{r}_2) = \langle I(\mathbf{r}_1) \rangle \langle I(\mathbf{r}_2) \rangle + \langle \Delta I(\mathbf{r}_1) \Delta I(\mathbf{r}_2) \rangle . \tag{7.2}$$

In Eq. (7.2), the second term $\Delta G^{(2)}(\mathbf{r}_1, \mathbf{r}_2) = \langle \Delta I(\mathbf{r}_1) \Delta I(\mathbf{r}_2) \rangle$ measures the correlation of intensity fluctuations.

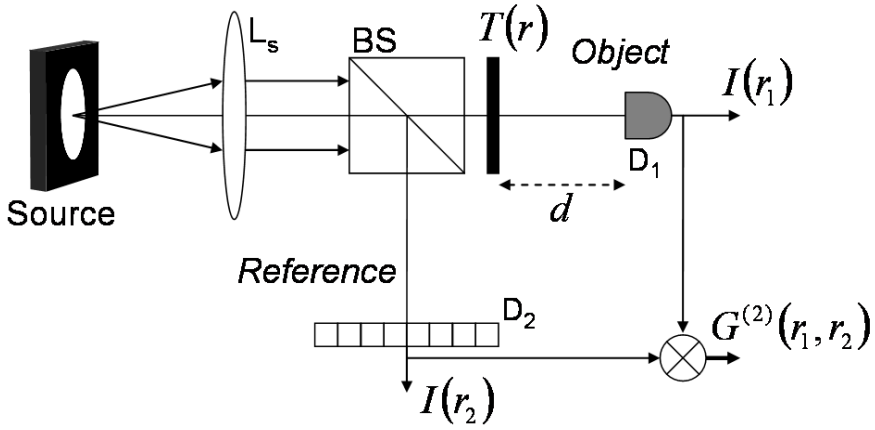

Figure 7.1: Schematic of the setup used for correlated imaging. The source is thermal, quasi monochromatic and spatially incoherent with a uniform intensity distribution.

In order to relate the second-order intensity correlation function expressed in Eqs. (7.1) and (7.2) to the transmittance T of the object, we first consider one monochromatic realization $E_0(\mathbf{r})$ of the incident field ensemble in the transverse planes located at a distance h from L_s in both arms. Propagating $E_0(\mathbf{r})$ to the detection plane in the reference arm leads to

$$E_2(\mathbf{r}_2) = \int E_0(\mathbf{r}) h_2(\mathbf{r}_2, \mathbf{r}) d^2\mathbf{r}, \tag{7.3}$$

where $h_2(\mathbf{r}_2, \mathbf{r})$ is the deterministic impulse response function of the reference system. Considering a thin screen object and a deterministic impulse response function $h_1(\mathbf{r}_1, \mathbf{r}')$, the field in the detection plane of the object arm becomes

$$E_1(\mathbf{r}_1) = \int E_0(\mathbf{r}')\, T(\mathbf{r}')\, h_1(\mathbf{r}_1, \mathbf{r}')\, d^2\mathbf{r}'. \tag{7.4}$$

Since the intensities detected at points $\mathbf{r}_1$ and $\mathbf{r}_2$ depend on the fields as $I_1(\mathbf{r}_1) = |E_1(\mathbf{r}_1)|^2$ and $I_2(\mathbf{r}_2) = |E_2(\mathbf{r}_2)|^2$, substituting Eqs. (7.3) and (7.4) into Eq. (7.1), we obtain the following expression for the second-order intensity correlation function

$$\begin{aligned} G^{(2)}(\mathbf{r}_1, \mathbf{r}_2) = \int & \langle E_0^*(\mathbf{r}_0)\, E_0(\mathbf{r}_0')\, E_0^*(\mathbf{r})\, E_0(\mathbf{r}')\rangle\, T^*(\mathbf{r})\, T(\mathbf{r}') \\ & \times h_2^*(\mathbf{r}_2, \mathbf{r}_0)\, h_2(\mathbf{r}_2, \mathbf{r}_0')\, h_1^*(\mathbf{r}_1, \mathbf{r})\, h_1(\mathbf{r}_1, \mathbf{r}')\, d^2\mathbf{r}_0 d^2\mathbf{r}_0' d^2\mathbf{r} d^2\mathbf{r}'. \end{aligned} \tag{7.5}$$

As one can see from Eq. (7.5), $G^{(2)}$ depends on the fourth-order correlation function of the incident field which, in general, cannot be expressed in terms of the second-order correlation function $W_0(\mathbf{r}, \mathbf{r}') = \langle E_0^*(\mathbf{r})\, E_0(\mathbf{r}')\rangle$. However, since our source is spatially incoherent, it can be regarded as a superposition of a large number of independent radiating elements, and the field E_0 obeys Gaussian statistic. The moment theorem can then be applied to relate the second-order to the fourth-order correlation function. It follows:

$$\begin{aligned} \langle E_0^*(\mathbf{r}_0)\, E_0(\mathbf{r}_0')\, E_0^*(\mathbf{r})\, E_0(\mathbf{r}')\rangle &= \langle E_0^*(\mathbf{r}_0)\, E_0(\mathbf{r}_0')\rangle \langle E_0^*(\mathbf{r})\, E_0(\mathbf{r}')\rangle \\ &\quad + \langle E_0^*(\mathbf{r}_0)\, E_0(\mathbf{r}')\rangle \langle E_0^*(\mathbf{r})\, E_0(\mathbf{r}_0')\rangle. \end{aligned} \tag{7.6}$$

Substituting Eq. (7.6) into Eq. (7.5), $G^{(2)}$ can then be expressed as

$$G^{(2)}(\mathbf{r}_1, \mathbf{r}_2) = \langle I_1(\mathbf{r}_1)\rangle \langle I_2(\mathbf{r}_2)\rangle + |W(\mathbf{r}_1, \mathbf{r}_2)|^2, \tag{7.7}$$

where the cross-correlation function $W(\mathbf{r}_1, \mathbf{r}_2) = \langle E_1^*(\mathbf{r}_1) E_2(\mathbf{r}_2) \rangle$ takes the form [99]

$$W(\mathbf{r}_1, \mathbf{r}_2) = \iint W_0(\mathbf{r}, \mathbf{r}') T(\mathbf{r}') h_2^*(\mathbf{r}_2, \mathbf{r}) h_1(\mathbf{r}_1, \mathbf{r}') d^2\mathbf{r} d^2\mathbf{r}'. \tag{7.8}$$

Equation (7.7) is known as the Siegert relation [97] and is applicable in the case of quasi-thermal light. The first element of the sum (7.7) is an incoherent background term which originates from accidental coincidence counts, while the second term $\Delta G^{(2)}(\mathbf{r}_1, \mathbf{r}_2) = |W(\mathbf{r}_1, \mathbf{r}_2)|^2$ corresponds to the correlation of intensity fluctuations. In conventional two-photon and correlated imaging [95], the spatially incoherent source has a uniform intensity distribution. Consequently, when varying the positions $\mathbf{r}_1$ and $\mathbf{r}_2$ of the detectors in the reference and object arms, the measurements of the average intensities $\langle I_1(\mathbf{r}_1) \rangle$ and $\langle I_2(\mathbf{r}_2) \rangle$ are constant and therefore do not provide sufficient information in order to reconstruct the transmittance of the object [98]. However, as one can see from Eq. (7.8), the correlation between the intensity fluctuations in both arms depends on T.

In order to simplify the relation between $\Delta G^{(2)}(\mathbf{r}_1, \mathbf{r}_2)$ and T, we further consider the free space Fresnel approximation for the impulse response functions h_1 and h_2 so that

$$h_i(\mathbf{r}_i, \mathbf{r}) = \frac{\exp(ikd)}{i\lambda d} \exp\left[i\frac{k}{2d} \left(\mathbf{r}_i^2 + \mathbf{r}^2 \right) \right] \exp\left(-i\frac{k}{d} \mathbf{r}_i \cdot \mathbf{r} \right), \tag{7.9}$$

where k is the wave vector and $i = 1, 2$. Without loss of generality, the detector D_1 is set at a fixed position $\mathbf{r}_1 = 0$. Equations (7.8) and (7.9) then yield

$$W(\mathbf{0}, \mathbf{r}_2) = \exp\left[-i\frac{k}{2d} \mathbf{r}_2^2 \right] \iint W_0(\mathbf{r}, \mathbf{r}') T(\mathbf{r}') \exp\left[i\frac{k}{2d} \left(\mathbf{r}'^2 - \mathbf{r}^2 \right) + i\frac{k}{d} \mathbf{r}_2 \cdot \mathbf{r} \right] d^2\mathbf{r} d^2\mathbf{r}'. \tag{7.10}$$

According to Eq. (4.4), the cross-spectral density of the incident field in the transverse plane of the object is related to the intensity distribution $I_s(\boldsymbol{\xi})$ across the source by the

relation

$$W_0(\mathbf{r},\mathbf{r}') = \int_S I_s(\boldsymbol{\xi}) \exp\left[i\frac{k}{f}\boldsymbol{\xi}\cdot(\mathbf{r}-\mathbf{r}')\right] d\boldsymbol{\xi}, \tag{7.11}$$

where f is the focal length of L_s. $W_0(\mathbf{r},\mathbf{r}')$ depends only on the transverse separation $\Delta\mathbf{r} = \mathbf{r}-\mathbf{r}'$, and considering a circular source of radius R with uniform intensity distribution so that $I_s(\boldsymbol{\xi}) = 1$ if $|\boldsymbol{\xi}| \leq R$ and equals zero otherwise, the cross-spectral density takes the form

$$W_0(\Delta\mathbf{r}) = 4\pi R^2 J_1(x)/x, \tag{7.12}$$

with J_1 being the first order Bessel function and $x = kR|\Delta\mathbf{r}|/f$. The width of $W_0(\Delta\mathbf{r})$ is approximately $\lambda f/(2R)$ and relates to the transverse coherence length of the beam, which determines the resolution of the imaging scheme [99]. Assuming that the smallest features of the object are larger than the transverse coherence length of the incident field, W_0 is well approximated by a Delta function in Eq. (7.10) and we obtain

$$W(\mathbf{0},\mathbf{r}_2) = \exp\left[-i\frac{k}{2d}\mathbf{r}_2^2\right] \int T(\mathbf{r}) \exp\left(i\frac{k}{d}\mathbf{r}_2\cdot\mathbf{r}\right) d^2\mathbf{r}. \tag{7.13}$$

Defining the Fourier transform of T as

$$\widetilde{T}(\mathbf{q}) = \int T(\mathbf{r}) \exp(-i\mathbf{q}\cdot\mathbf{r})\, d^2\mathbf{r}, \tag{7.14}$$

the relation (7.13) between $W(\mathbf{0},\mathbf{r}_2)$ and $T(\mathbf{r})$ can be expressed as

$$|W(\mathbf{0},\mathbf{r}_2)|^2 = \left|\widetilde{T}\left(-\frac{k}{d}\mathbf{r}_2\right)\right|^2. \tag{7.15}$$

According to Eq. (7.15), measuring the excess coincidence counts $\Delta G^{(2)}(\mathbf{0},\mathbf{r}_2)$ as a function of the detector's position $\mathbf{r}_2$ in the reference arm yields the amplitude of the Fourier

transform of the object's transmittance. Even though the incident field is spatially incoherent, coherent Fourier imaging is achieved by correlating the intensity fluctuations in both arms. Also referred as "ghost imaging", since $\widetilde{T}$ is recovered by scanning the detector in the arm which does not contain the object, correlated imaging is a technique particularly attractive for lensless applications and situations, such as x-ray imaging [95], where only spatially incoherent sources are available.

One of the main limitation of correlated imaging is the lack of phase information since only the amplitude of the Fourier transform is retrieved. In order to overcome this drawback, we propose in the next section to modulate the intensity distribution across the source and shape the degree of spatial coherence of the incident field. Moreover, we will show that the reconstruction of the Fourier transform can be achieved in a robust manner with two fixed detectors.

7.1.2 Correlated imaging with shaped spatially partially coherent light

Let us consider in Fig. 7.2 the new configuration for the correlated imaging setup, where both detectors D_1 and D_2 are now fixed on the optical axis. The expression given in Eq. (7.8) for the cross-spectral density of the fields at the locations $\mathbf{r}_1 = \mathbf{0}$ and $\mathbf{r}_2 = \mathbf{0}$ in the detectors' plane becomes

$$W(\mathbf{0},\mathbf{0}) = \iint W_0(\mathbf{r},\mathbf{r}')\, T(\mathbf{r}')\, h_2^*(\mathbf{0},\mathbf{r})\, h_1(\mathbf{0},\mathbf{r}')\, d^2\mathbf{r} d^2\mathbf{r}'. \tag{7.16}$$

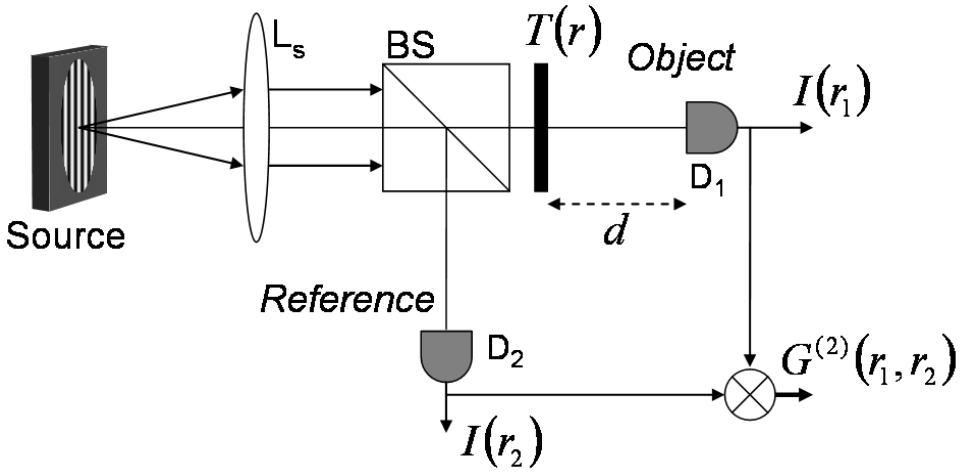

Figure 7.2: Schematic of the setup used for correlated imaging with shaped spatially partially coherent light.

In the previous section, the Fourier transform of T was evaluated by scanning D_2 in the reference arm. Our approach considers measuring the coincidence rate of two fixed detectors, while varying the coherence properties of the incident field described by W_0 in Eq. (7.16). For this purpose, we consider the following modulated intensity distribution across the source

$$I_s(\boldsymbol{\xi}) = \frac{1}{2} Q(\xi) \left[1 + m \cos\left(\frac{k}{f} \boldsymbol{\xi} \cdot \boldsymbol{\Delta}\mathbf{r}_0 - \phi \right) \right], \tag{7.17}$$

where m is a modulation factor with $0 \leq m \leq 1$, R is the source's radius and $Q(x) = 1$ if $x \leq R$ and equals zero otherwise. The periodicity of the intensity modulation is adjusted by the value of the vector $\boldsymbol{\Delta}\mathbf{r}_0$, while ϕ is an adjustable phase term. Using the van Cittert-

Zernike theorem expressed in Eq. (2.19), the coherence function of the field after L_s becomes

$$W_0(\mathbf{r},\mathbf{r}') = g(\boldsymbol{\Delta}\mathbf{r}) + \frac{m}{2}\exp(i\phi)\, g(\boldsymbol{\Delta}\mathbf{r}-\boldsymbol{\Delta}\mathbf{r}_0) + \frac{m}{2}\exp(-i\phi)\, g(\boldsymbol{\Delta}\mathbf{r}+\boldsymbol{\Delta}\mathbf{r}_0), \tag{7.18}$$

where $\boldsymbol{\Delta}\mathbf{r} = \mathbf{r}-\mathbf{r}'$ and

$$g(\boldsymbol{\Delta}\mathbf{r}) = 2\pi R^2 J_1(x)/x, \tag{7.19}$$

with $x = kR|\boldsymbol{\Delta}\mathbf{r}|/f$. Similarly to the width of $W_0(\Delta\mathbf{r})$ defined in Eq. (7.12), the width of $g(\boldsymbol{\Delta}\mathbf{r})$ is approximately $\lambda f/(2R)$ and relates to the resolution of the imaging scheme [99]. The field commonly used in correlated imaging corresponds to the case $m = 0$ in Eq. (7.18).

As seen in Chapter 4, modulating the intensity distribution across the source generates a field composed of correlated volumes of coherence, which introduce coherent scattering from parts of the object separated by a distance $\boldsymbol{\Delta}\mathbf{r}_0$ [60]. Substituting Eq. (7.18) into Eq. (7.16) and using the Fresnel approximation expressed in Eq. (7.9), we obtain the resulting correlation of intensity fluctuations

$$\Delta G^{(2)}(\mathbf{0},\mathbf{0}) = \left| \begin{array}{c} \iint g(\boldsymbol{\Delta}\mathbf{r})T(\mathbf{r}')\exp\left[-i\frac{k}{2d}\left(\Delta\mathbf{r}^2+2\mathbf{r}'\cdot\Delta\mathbf{r}\right)\right]d^2\mathbf{r}'d^2\Delta\mathbf{r} \\ +\frac{m\exp(i\phi)}{2}\iint g(\boldsymbol{\Delta}\mathbf{r}-\boldsymbol{\Delta}\mathbf{r}_0)T(\mathbf{r}')\exp\left[-i\frac{k}{2d}\left(\Delta\mathbf{r}^2+2\mathbf{r}'\cdot\Delta\mathbf{r}\right)\right]d^2\mathbf{r}'d^2\Delta\mathbf{r} \\ +\frac{m\exp(-i\phi)}{2}\iint g(\boldsymbol{\Delta}\mathbf{r}+\boldsymbol{\Delta}\mathbf{r}_0)T(\mathbf{r}')\exp\left[-i\frac{k}{2d}\left(\Delta\mathbf{r}^2+2\mathbf{r}'\cdot\Delta\mathbf{r}\right)\right]d^2\mathbf{r}'d^2\Delta\mathbf{r} \end{array} \right|^2 . \tag{7.20}$$

Recognizing the Fourier transform of T defined in Eq. (7.14), Eq. (7.20) becomes

$$\Delta G^{(2)}(\mathbf{0},\mathbf{0}) = \left| \begin{array}{c} \int g(\boldsymbol{\Delta}\mathbf{r})\widetilde{T}\left(\frac{k}{d}\boldsymbol{\Delta}\mathbf{r}\right)\exp\left(-i\frac{k}{2d}\Delta\mathbf{r}^2\right)d^2\Delta\mathbf{r} \\ +\frac{m\exp(i\phi)}{2}\int g(\boldsymbol{\Delta}\mathbf{r}-\boldsymbol{\Delta}\mathbf{r}_0)\widetilde{T}\left(\frac{k}{d}\boldsymbol{\Delta}\mathbf{r}\right)\exp\left(-i\frac{k}{2d}\Delta\mathbf{r}^2\right)d^2\Delta\mathbf{r} \\ +\frac{m\exp(-i\phi)}{2}\int g(\boldsymbol{\Delta}\mathbf{r}+\boldsymbol{\Delta}\mathbf{r}_0)\widetilde{T}\left(\frac{k}{d}\boldsymbol{\Delta}\mathbf{r}\right)\exp\left(-i\frac{k}{2d}\Delta\mathbf{r}^2\right)d^2\Delta\mathbf{r} \end{array} \right|^2 . \tag{7.21}$$

In the second and third integrals of Eq. (7.21), we define, respectively, the new variables $\mathbf{\Delta r}' = \mathbf{\Delta r} - \mathbf{\Delta r}_0$ and $\mathbf{\Delta r}'' = \mathbf{\Delta r} + \mathbf{\Delta r}_0$ so that $\Delta G^{(2)}(\mathbf{0},\mathbf{0})$ can be written as

$$\Delta G^{(2)}(\mathbf{0},\mathbf{0}) = \left| \begin{array}{c} \int g(\mathbf{\Delta r})\widetilde{T}\left(\frac{k}{d}\mathbf{\Delta r}\right)\exp\left[\Phi\left(\mathbf{\Delta r},\mathbf{0}\right)\right]d^2\Delta\mathbf{r} \\ +\frac{m\exp(i\phi+i\psi)}{2}\int g(\mathbf{\Delta r}')\widetilde{T}\left[\frac{k}{d}\left(\mathbf{\Delta r}'+\mathbf{\Delta r}_0\right)\right]\exp\left[\Phi\left(\mathbf{\Delta r}',\mathbf{\Delta r}_0\right)\right]d^2\Delta\mathbf{r}' \\ +\frac{m\exp(-i\phi+i\psi)}{2}\int g(\mathbf{\Delta r}'')\widetilde{T}\left[\frac{k}{d}\left(\mathbf{\Delta r}''-\mathbf{\Delta r}_0\right)\right]\exp\left[\Phi\left(\mathbf{\Delta r}'',-\mathbf{\Delta r}_0\right)\right]d^2\Delta\mathbf{r}'' \end{array} \right|^2, \tag{7.22}$$

with $\psi = -k\mathbf{\Delta r}_0^2/(2d)$ and

$$\Phi\left(\mathbf{\Delta r},\mathbf{\Delta r}_0\right) = -i\frac{k}{2d}\Delta\mathbf{r}^2 - i\frac{k}{d}\Delta\mathbf{r}\cdot\mathbf{\Delta r}_0. \tag{7.23}$$

Corresponding to the first element in the right hand side of Eq. (7.23), the phase term $\exp\left[-ik\mathbf{\Delta r}'^2/(2d)\right]$ in Eq. (7.22) can be neglected since d is usually on the order of few centimeters and the range of values of $\mathbf{\Delta r}$ is limited by the width of g, which does not exceed $10\mu m$ in a typical experiment. This approximation results in the following correlation of intensity fluctuations

$$\Delta G^{(2)}(\mathbf{0},\mathbf{0}) = \left|\chi_e(\mathbf{0}) + m\exp(i\psi)\left[\chi_e(\mathbf{\Delta r}_0)\cos(\phi) - \chi_o(\mathbf{\Delta r}_0)\sin(\phi)\right]\right|^2, \tag{7.24}$$

with χ_e and χ_o being the even and odd parts of χ defined as

$$\chi(\mathbf{\Delta r}_0) = \int g(\mathbf{\Delta r}')\widetilde{T}\left[\frac{k}{d}\left(\mathbf{\Delta r}' - \mathbf{\Delta r}_0\right)\right]\exp\left(i\frac{k}{d}\mathbf{\Delta r}'\cdot\mathbf{\Delta r}_0\right)d^2\mathbf{\Delta r}'. \tag{7.25}$$

Furthermore, in the limiting case where the transverse coherence of the incident field tends to zero, the function g is well approximated by a Delta function in Eq. (7.25) and we obtain

$$\chi(\mathbf{\Delta r}_0) = \widetilde{T}\left(-k\mathbf{\Delta r}_0/d\right). \tag{7.26}$$

Measuring $\Delta G^{(2)}(\mathbf{0},\mathbf{0})$ as a function of $\mathbf{\Delta r}_0$ for $\phi = 0,\ \pi,\ \pi/2$ and $-\pi/2$, leads to a linear system of equations (see Section 7.1.2.1) from which one can calculate independently $\left|\chi_j(\mathbf{\Delta r}_0)\right|$ as well as the quantity $\cos\left[\psi(\mathbf{\Delta r}_0) + \theta_j(\mathbf{\Delta r}_0) - \theta_e(\mathbf{0})\right]$ related to the arguments θ_j of χ_j, where $j = e,\ o$. Contrary to conventional correlated imaging, where only the modulus of $\widetilde{T}$ is recovered, the special structure of the incident coherence function allows also phase information to be obtained.

7.1.2.1 Calculation of the Fourier transform of the transmittance from experimental intensity measurements

This section provides specific details about the system of equations one needs to solve in order to retrieve the amplitude and the phase information of χ. The intensity-intensity correlation $G^{(2)}_{meas}$ measured experimentally is related to the average intensities $\langle I_1(\mathbf{r}_1 = \mathbf{0})\rangle$ and $\langle I_2(\mathbf{r}_2 = \mathbf{0})\rangle$, and to the correlation of intensity fluctuations $\Delta G^{(2)}(\mathbf{0},\mathbf{0})$ by the relation

$$G^{(2)}_{meas} = A\langle I_1(\mathbf{0})\rangle\langle I_2(\mathbf{0})\rangle + A\alpha\Delta G^{(2)}(\mathbf{0},\mathbf{0}). \tag{7.27}$$

In this last equation, A and α are unknown proportionality coefficients. Equation (7.27) differs from the Siegert relation expressed in Eq. (7.7) by the term α satisfying $0 \leq \alpha \leq 1$. The reason of this discrepancy originates from the finite response time of the detection system. In our case, fast detectors able to resolve in time the fluctuations of intensity were not used. Instead, the intensity measurements were performed using photomultiplier tubes (PMT) and the number of detected photons within one gate time were recorded. A

coincidence circuit and a photon counter were then used to obtain the number of coincident counts $G^{(2)}_{meas}$. With T_r and T_c being the resolution time of the circuit and the coherence time of the source, respectively, α satisfies the relation [97]

$$\alpha = T_c/T_r, \tag{7.28}$$

valid only for $T_c \leq T_r$. Even though the two PMTs used were identical, a mismatch in the electronic would introduce a time delay between the two arms of the interferometer. This delay would further reduce α and the efficiency of the coincidence circuit.

The average numbers of counts measured by the PMTs D_1 and D_2 are related to the average intensities $\langle I_1(\mathbf{r}_1 = \mathbf{0})\rangle$ and $\langle I_2(\mathbf{r}_2 = \mathbf{0})\rangle$ by the unknown proportionality coefficients A_1 and A_2:

$$\begin{cases} \langle I_1\rangle_{meas} = A_1 \langle I_1(\mathbf{0})\rangle \\ \langle I_2\rangle_{meas} = A_2 \langle I_2(\mathbf{0})\rangle \end{cases}. \tag{7.29}$$

In Eqs. (7.27) and (7.29), A, A_1 and A_2 need to be determined in order to recover $\Delta G^{(2)}$ from Eq. (7.27). Using Eqs. (7.3) and (7.18), the intensity in the reference arm can be shown to depend on $\mathbf{\Delta r}_0$ as follow

$$\langle I_2(\mathbf{0})\rangle = g(\mathbf{0}) + m\,\mathrm{Re}\left[g(\mathbf{\Delta r}_0)\exp(-i\phi)\right]. \tag{7.30}$$

As represented in Fig. 7.3, $\langle I_2(\mathbf{0})\rangle$ is calculated as a function of the coherence parameter $\mathbf{\Delta r}_0$ using Eq. (7.19). Because of the Bessel function in the expression (7.19) of g, the intensity $\langle I_2(\mathbf{0})\rangle$ oscillates with $\mathbf{\Delta r}_0$. However, for large values of $|\mathbf{\Delta r}_0|$, $\langle I_2(\mathbf{0})\rangle$ tends to an asymptotic limit $g(\mathbf{0})$. The reference intensity is normalized to this asymptotic value,

which is experimentally measured by setting a large value for $|\mathbf{\Delta r}_0|$. Similarly and keeping the same source configuration, $\langle I_1 \rangle_{meas}$ is normalized after removing the object.

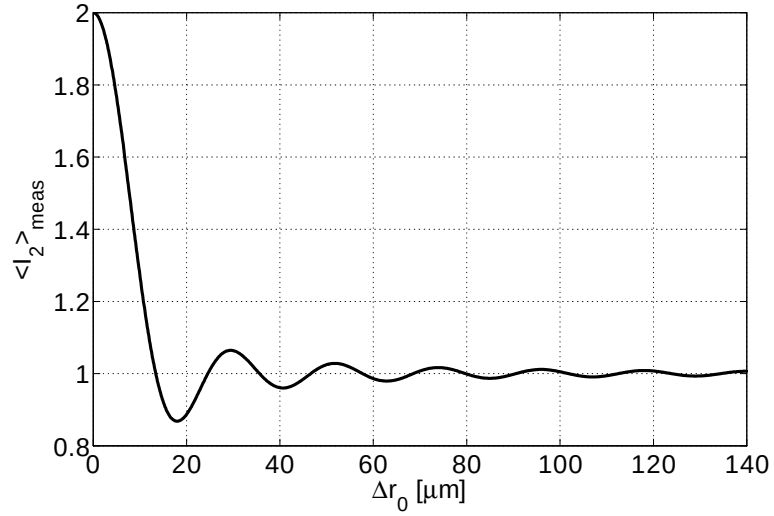

Figure 7.3: Reference intensity as a function of the coherence parameter $\mathbf{\Delta r}_0$ and normalized to its asymptotic limit $g(0)$. The wavelength is $\lambda = 532nm$ and the source parameters are $f = 62mm$, $m = 1$, $\phi = 0$ and $R = 2mm$.

Still without the test object, the detector D_2 in the reference arm is detuned from its position $\mathbf{r}_2 = \mathbf{0}$. Represented in Fig. 7.4 are the intensities $\langle I_1 \rangle_{meas}$, $\langle I_2 \rangle_{meas}$, and the coincidence counts $G^{(2)}_{meas}$ measured experimentally for r_2 ranging from $-40\mu m$ to $40\mu m$. As expected, $\langle I_1 \rangle_{meas}$ and $\langle I_2 \rangle_{meas}$ are constant while $G^{(2)}_{meas}$ is enhanced by a factor $\alpha = 0.28$ for $\mathbf{r}_2 \approx \mathbf{0}$. The width of the enhancement is around $13\mu m$ and corresponds to the width $\lambda f/(2R)$ of the function g. If D_2 is detuned to a position $|\mathbf{r}_2| >> \lambda f/(2R)$ so that $|\mathbf{r}_2 - \mathbf{r}_1|$ is much larger than the width of g, then we have $\Delta G^{(2)}(\mathbf{0}, \mathbf{r}_2) = 0$. It follows that the number of coincidence count is directly proportional to $\langle I_1(\mathbf{0}) \rangle \langle I_2(\mathbf{0}) \rangle$ and the recorded

value $G^{(2)}_{meas}\Big|_{Norm}$ is used to normalize the measured intensity correlation $G^{(2)}_{meas}$. The object is then put back in place and D_2 is set again at the position $\mathbf{r}_2 = \mathbf{0}$. From now on, $G^{(2)}_{meas}$, $\langle I_1 \rangle_{meas}$, and $\langle I_2 \rangle_{meas}$ refers to the normalized pulse measurements. The excess coincidence counts is then calculated from the relation

$$\alpha \Delta G^{(2)}(\mathbf{0}, \mathbf{0}) = G^{(2)}_{meas} - \langle I_1 \rangle_{meas} \langle I_2 \rangle_{meas} . \tag{7.31}$$

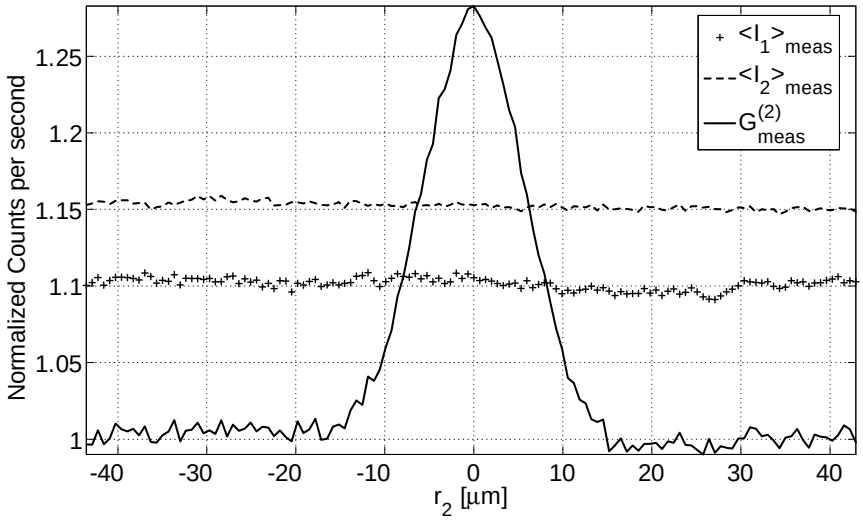

Figure 7.4: Measurement of the intensities $\langle I_1 \rangle_{meas}$, $\langle I_2 \rangle_{meas}$, and the coincidence counts $G^{(2)}_{meas}$ as a function of the position r_2 of the detector D_2. The number of counts $\langle I_1 \rangle_{meas}$ and $\langle I_2 \rangle_{meas}$ are normalized to their average value and then shifted in the graph for better legibility. $G^{(2)}_{meas}$ was normalized to its average background value.

In order to recover the even part of χ, the quantities $G^{(2)}_{meas}$, $\langle I_1 \rangle_{meas}$, and $\langle I_2 \rangle_{meas}$ are measured as a function of $\mathbf{\Delta r}_0$ for the different phases $\phi = 0$ and $\phi = \pi$. Substituting Eq.

(7.24) into Eq. (7.27), a set of two equations is then obtained

$$\begin{cases} \alpha\Delta G^{(2)}\left(\mathbf{0},\mathbf{0}\right)\big|_{\phi=0} = \alpha\left|\chi_e\left(\mathbf{0}\right)\right|^2 + \alpha m^2\left|\chi_e\left(\boldsymbol{\Delta}\mathbf{r}_0\right)\right|^2 + 2\alpha m\,\mathrm{Re}\left[\exp\left(i\psi\right)\chi_e\left(\boldsymbol{\Delta}\mathbf{r}_0\right)\chi_e^*\left(\mathbf{0}\right)\right] \\ \alpha\Delta G^{(2)}\left(\mathbf{0},\mathbf{0}\right)\big|_{\phi=\pi} = \alpha\left|\chi_e\left(\mathbf{0}\right)\right|^2 + \alpha m^2\left|\chi_e\left(\boldsymbol{\Delta}\mathbf{r}_0\right)\right|^2 - 2\alpha m\,\mathrm{Re}\left[\exp\left(i\psi\right)\chi_e\left(\boldsymbol{\Delta}\mathbf{r}_0\right)\chi_e^*\left(\mathbf{0}\right)\right] \end{cases}. \tag{7.32}$$

The modulation parameter m is retrieved by measuring $m = \langle I_2\left(\mathbf{0}\right)\rangle\big|_{\boldsymbol{\Delta}\mathbf{r}_0=0} - 1$. Furthermore, considering the value of $\Delta G^{(2)}\left(\mathbf{0},\mathbf{0}\right)$ at $\boldsymbol{\Delta}\mathbf{r}_0 = 0$ in both equations of the system (7.32), one can calculate independently $\left|\chi_e\left(\boldsymbol{\Delta}\mathbf{r}_0\right)\right|$ as well as the quantity $\cos\left[\psi\left(\boldsymbol{\Delta}\mathbf{r}_0\right) + \theta_e\left(\boldsymbol{\Delta}\mathbf{r}_0\right) - \theta_e\left(\mathbf{0}\right)\right]$. In the situation where $\chi_e\left(\mathbf{0}\right) = 0$, only $\left|\chi_e\left(\boldsymbol{\Delta}\mathbf{r}_0\right)\right|$ can be retrieved; however, this difficulty can be easily resolved by placing one of the detectors at a transverse position $\mathbf{r}_D$ such that $\widetilde{T}\left(-k\mathbf{r}_D/d\right) \neq 0$. A linear system of equations similar to the previous one is then obtained.

Deducing the amplitude and phase information of the odd part of χ from the experimental intensity measurements follows a similar procedure. In this case, the source phase parameter needs to be set to $\phi = \pi/2$ and $\phi = -\pi/2$.

7.1.3 Klyshko's geometrical optics approach

To better understand the effect of using an incident partially coherent field in the correlated imaging scheme, we consider Klyshko's geometrical optics approach for two-photon imaging [89, 100]. In this method, the setups represented in Figs. 7.1 and 7.2 are unfolded with respect to the source S and D_1 acts as a point source illuminating the object. As shown in Figs. 7.5(a) and 7.5(b), the right hand side of S corresponds to the reference arm

whereas the object arm is located on the left hand side of S. In Fig. 7.5(a), the intensity distribution across S is not modulated, i.e. $m = 0$ in Eq. (7.17), and the source behaves as a phase conjugation mirror [93]. The position of D_2 corresponds to the location of the Fourier plane Σ of the object T and the image T' of T by the source is located at a distance d in front of D_2. When I_s is modulated, as represented in Fig. 7.5(b), S acts as a grating phase conjugation mirror with transmission given by Eq. (7.17). The light originating from D_1 is then diffracted in one order 0 and two orders $+1$ and -1 with phase shift $-\phi$ and ϕ, respectively. Without the object, the orders $+1$ and -1 converge in the plane Σ at the positions $\mathbf{\Delta r}_0$ and $-\mathbf{\Delta r}_0$, respectively, as shown in Fig. 7.5(b).

When the object's image T' is illuminated by a spherical wave focusing at a position $\mathbf{\Delta r}_0$ in the plane Σ, the field $U_\Sigma^0(\mathbf{r}_2, \mathbf{\Delta r}_0)$ in the plane Σ takes the form

$$U_\Sigma^0(\mathbf{r}_2, \mathbf{\Delta r}_0) = \widetilde{T}\left[\frac{k}{d}(\mathbf{r}_2 - \mathbf{\Delta r}_0)\right] \exp\left(ik\frac{\mathbf{r}_2^2}{2d} + i\psi\right), \tag{7.33}$$

and corresponds to the Fourier component $\widetilde{T}[k(\mathbf{r}_2 - \mathbf{\Delta r}_0)/d]$ multiplied by a spherical carrier wave centered on axis at the image plane of T and with phase shift $\psi = -k\mathbf{\Delta r}_0^2/(2d)$. It follows that the field at $\mathbf{r}_2 = 0$ consists of contributions from three spatial frequencies of T and, accounting for the phase shifts of orders $+1$ and -1, the total field U_Σ^T becomes

$$U_\Sigma^T(\mathbf{0}) = U_\Sigma^0(\mathbf{0}) + \frac{m}{2}\exp(-i\phi)\, U_\Sigma^0(\mathbf{0}, \mathbf{\Delta r}_0) + \frac{m}{2}\exp(i\phi)\, U_\Sigma^0(\mathbf{0}, -\mathbf{\Delta r}_0). \tag{7.34}$$

Substituting Eq. (7.33) into Eq. (7.34), taking the modulus square of $U_\Sigma^T(\mathbf{0})$ and separating $\widetilde{T}$ into the odd and even parts, one obtains the same expression given in Eq. (7.24). Therefore, the possibility of recovering the phase information originates from the grating

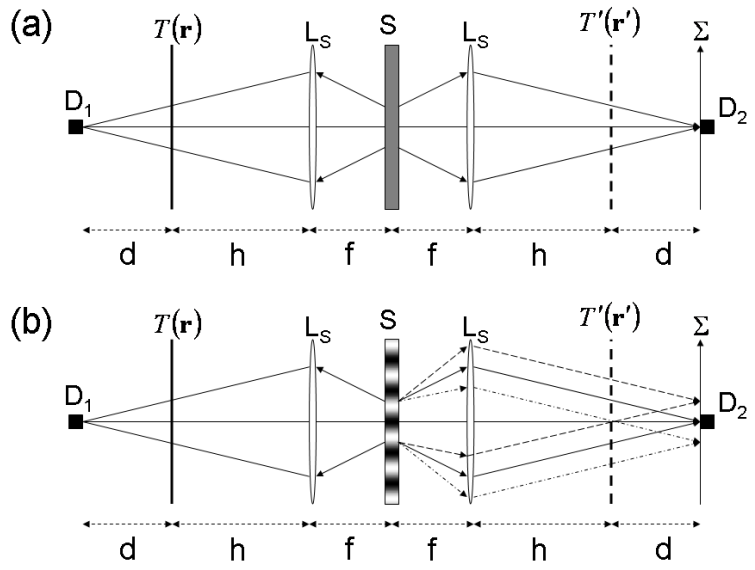

Figure 7.5: Scheme (a) corresponds to the unfolded representation of the setup used in conventional correlated imaging where the spatially incoherent source S has a uniform intensity distribution. In scheme (b), the intensity distribution across S is modulated according to Eq. (7.17).

structure of S, which produces at the detector an interference between the spatial components $\widetilde{T}(0)$, $\widetilde{T}(k\boldsymbol{\Delta}\mathbf{r}_0/d)$ and $\widetilde{T}(-k\boldsymbol{\Delta}\mathbf{r}_0/d)$.

7.1.4 Duality between classical and two-photon correlated imaging

The duality between partial coherence and partial entanglement [101] allows us to conceive a quantum imaging scheme equivalent to using a thermal source with adjustable intensity distribution in order to obtain both amplitude and phase information about the object.

In this configuration, the source consists of a monochromatic pump field E_p with angular frequency ω_p illuminating a thin nonlinear crystal. A two-photon entangled state is then generated by spontaneous parametric down-conversion [89]. In the unfolded representation of the setup in Fig. 7.6, the signal photon with angular frequencies ω_s and wave vector $\mathbf{k}_s$ propagates to the left of the source while the idler photon with angular frequencies ω_i and wave vector $\mathbf{k}_i$ propagates to the right. The source lays in the focal plane of a lens L_s with focal length f. The object T is located at a distance f from L_s in the signal arm while the detector D_1 is placed at a distance d away from the object.

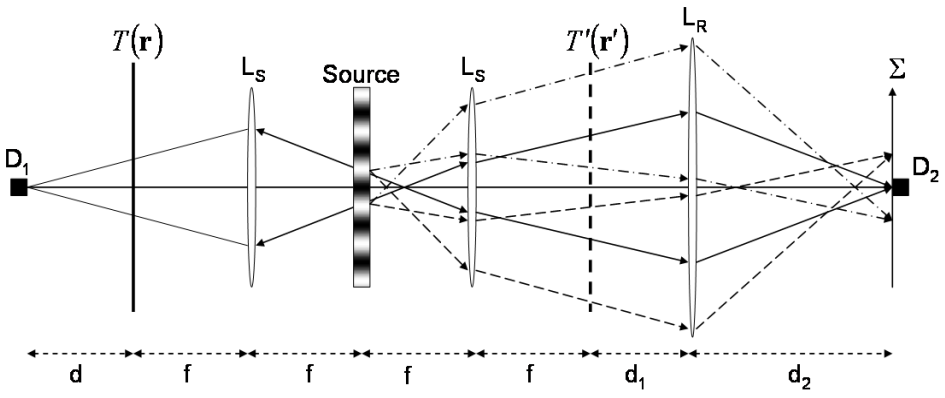

Figure 7.6: Unfolded representation of the two-photon correlated imaging setup. The complex Fourier transform of the object is reconstructed by using a biphoton source with adjustable degree of entanglement.

In analogy with the classical case (see Fig. 7.5(b)), where the intensity distribution I_s across the classical source was modulated according to Eq. (7.17), we consider a pump field

E_p with transverse spatial distribution

$$E_p(\mathbf{q}) = 1 + m\cos[\mathbf{q}\cdot\mathbf{\Lambda} - \phi], \tag{7.35}$$

where $\mathbf{\Lambda}$ is the spatial frequency of the modulation, m is the modulation amplitude taking values between 0 and 1, and ϕ is a fixed phase term. For a thin crystal, the conservation of momentum involves that $\mathbf{k}_{i\perp} + \mathbf{k}_{s\perp} = n\mathbf{\Lambda}$ with $n = 0$, 1 or -1, and where $\mathbf{k}_{i\perp}$ and $\mathbf{k}_{s\perp}$ correspond to the transverse wave vectors of the idler and signal photons, respectively. The spatial modulation of the pump field leads to the emission of a photon pair in a partially entangled state

$$\begin{aligned}|\Psi\rangle = &\sum_{s,i} \delta_\omega \delta(\mathbf{k}_{i\perp} + \mathbf{k}_{s\perp}) |\mathbf{k}_s\rangle \otimes |\mathbf{k}_i\rangle \\ &+ \frac{m}{2}\exp(i\phi)\sum_{s,i} \delta_\omega \delta(\mathbf{k}_{i\perp} + \mathbf{k}_{s\perp} - \mathbf{\Lambda}) |\mathbf{k}_s\rangle \otimes |\mathbf{k}_i\rangle \\ &+ \frac{m}{2}\exp(-i\phi)\sum_{s,i} \delta_\omega \delta(\mathbf{k}_{i\perp} + \mathbf{k}_{s\perp} + \mathbf{\Lambda}) |\mathbf{k}_s\rangle \otimes |\mathbf{k}_i\rangle,\end{aligned} \tag{7.36}$$

where the Delta function $\delta_\omega = \delta(\omega_s + \omega_i - \omega_p)$ derives from the energy conservation. The state (7.36) is a superposition of two-photon probability amplitudes. However, contrary to purely entangled photons, the momentum measurement of one photon does not yield with certainty the momentum of the other photon. Instead, the wave vector of the second photon can take three different values $\mathbf{k}_{s\perp} = -\mathbf{k}_{i\perp} + n\mathbf{\Lambda}$ with $n = 0$, 1 or -1. Using the van Cittert-Zernike theorem for biphoton source [101], it follows that the biphoton wave function takes the form

$$\psi_0(\boldsymbol{\beta}) \propto h(\beta) + \frac{m}{2}\exp(i\phi)\, h(\boldsymbol{\beta} - \boldsymbol{\beta}_0) + \frac{m}{2}\exp(-i\phi)\, h(\boldsymbol{\beta} + \boldsymbol{\beta}_0), \tag{7.37}$$

where $\boldsymbol{\beta}_0 = f\boldsymbol{\Lambda}$ and $\beta = k_s\mathbf{r}_s + k_i\mathbf{r}_i$ with $\mathbf{r}_s$ and $\mathbf{r}_i$ being two position vectors in the transverse planes located at a distance f from L_s in the signal and idler arms, respectively. To take into account the finite extend of the pump beam, $E_p(\mathbf{q})$ is multiplied by a Gaussian transverse profile $\exp\left[-q^2/\left(2\sigma_p^2\right)\right]$ of width σ_p. The finite size of the pump results in an imperfect two-photon momentum correlation characterized by the function

$$h(\beta) = \pi\sigma_p^2 \exp\left[-\sigma_p^2\beta^2/\left(2f^2\right)\right]. \tag{7.38}$$

The duality between the van Cittert-Zernike theorem for biphoton sources and classical sources [101] is illustrated by the similarity between expression (7.37) of the biphoton wave function and the form of the coherence function in Eq. (7.18).

In absence of transverse modulation of the pump field, i.e. $m = 0$, the crystal acts as a mirror in Klyshko's representation of the imaging setup in Fig. 7.6. In order to observe the diffraction pattern of T, a lens L_R is inserted in the idler arm at a distance $d_1 + f$ from L_s. The Fourier transform $\widetilde{T}$ is then observed in the plane Σ when the distance d_2 between L_R and the detector D_2 satisfies the thin-lens equation

$$\frac{1}{d_2} + \frac{1}{z} = \frac{1}{f_R}, \tag{7.39}$$

where f_R is the focal length of L_R and $z = d_1 + dk_s/k_i$. When E_p is modulated, the crystal acts as a grating with transmission given by Eq. (7.35). Similarly to the expression of the classical field in Eq. (7.34), the value of the biphoton wave function at the positions of D_1 and D_2 is a superposition of three diffraction patterns $\widetilde{T}(0)$, $\widetilde{T}\left[k_s\boldsymbol{\beta}_0/(d_ik_i)\right]$ and $\widetilde{T}\left[-k_s\boldsymbol{\beta}_0/(d_ik_i)\right]$. The rate of coincidence counts is then identical to the expression of the correlation of intensity

fluctuations in Eq. (7.24) for the classical case. The function $\chi_j(\mathbf{\Delta r}_0)$ in Eq. (7.25) is now replaced with

$$\chi_j^q(\boldsymbol{\beta}_0) = \int h(\beta)\,\widetilde{T}\left[k_s(\boldsymbol{\beta}-\boldsymbol{\beta}_0)/(d_i k_i)\right]\exp\left[i\boldsymbol{\beta}\cdot\boldsymbol{\beta}_0/(d_i k_i)\right]d^2\boldsymbol{\beta}. \tag{7.40}$$

The capability of inferring phase information about $\widetilde{T}$ is due to the partial entanglement of the two photons, which results in an interference between the three possible states one photon can take when the other one has already been measured.

Ignoring the diffraction limit imposed by the finite size of the imaging lenses, the uncertainty in the reconstruction of $\widetilde{T}$ results from the imperfect two-photon momentum correlation and is quantified by the width of $h(\beta)$. In the degenerate case where $k_s = k_i$ and $\Delta\beta = k\Delta(\mathbf{r}_s+\mathbf{r}_i)$, the uncertainty is $\Delta(\mathbf{r}_s+\mathbf{r}_i) = f/(k\sigma_p)$. For a classical source, the resolution is related to the transverse coherence length of the field given by the variance $\Delta(\mathbf{r}-\mathbf{r}') = f/(k\sigma_s)$ of the function $g(\mathbf{r}-\mathbf{r}')$. In this case, g is defined as

$$g(\mathbf{r}-\mathbf{r}') = \pi R^2 \exp\left[-k^2\sigma_s^2\frac{(\mathbf{r}-\mathbf{r}')^2}{2f^2}\right], \tag{7.41}$$

where we have considered $Q(\xi) = \exp\left[-\xi^2/(2\sigma_s^2)\right]$ in Eq. (7.17), σ_s being the size of the source. Similarly to the conclusions reached by D'Angelo [102], the resolutions in both cases are comparable. Apart from the lower visibility originating from the first term in the right hand side of Eq. (7.7), classical correlated imaging can mimic all the features of two-photon imaging [103].

7.2 Experimental results

In order to demonstrate the possibility of retrieving both the amplitude and the phase information of an object using a partially coherent beam, a correlated imaging experiment has been conducted. As illustrated in Fig. (7.7), a linearly polarized laser operating at $\lambda = 532nm$ and a Sagnac interferometer composed of a polarizing beam splitter PBS and two mirrors $M1$ and $M2$ were used to generate the fringe pattern that was projected onto a rotating diffuser in order to create a thermal-like secondary source. The periodicity of the fringes was adjusted by scanning the mirror $M2$ with a computer controlled translation stage. The radius of the source set to $R = 2mm$ was adjusted by the circular aperture A located in the focal plane of L_1 and imaged onto the diffuser placed in the focal plane of the lens L_2. In order to cancel the wavefront deformation introduced by the imperfect mirrors, and obtain a fringe pattern as identical as the expected interference field, the laser beam was focused by L_1 in the center of the Sagnac interferometer.

The phase ϕ of the intensity distribution on the secondary source was controlled by a half and quarter-wave plates placed after L_1. The modulation of the interference pattern was adjusted by the orientation of the polarizer P. The half-wave plate, the polarizing beam splitter and the quarter-wave plate located after P and before the diffuser were arranged in order to maximize the power of the scattered light collected by the lens L_s. The $25mm$ diameter lens L_s had a focal length of $f = 62mm$.

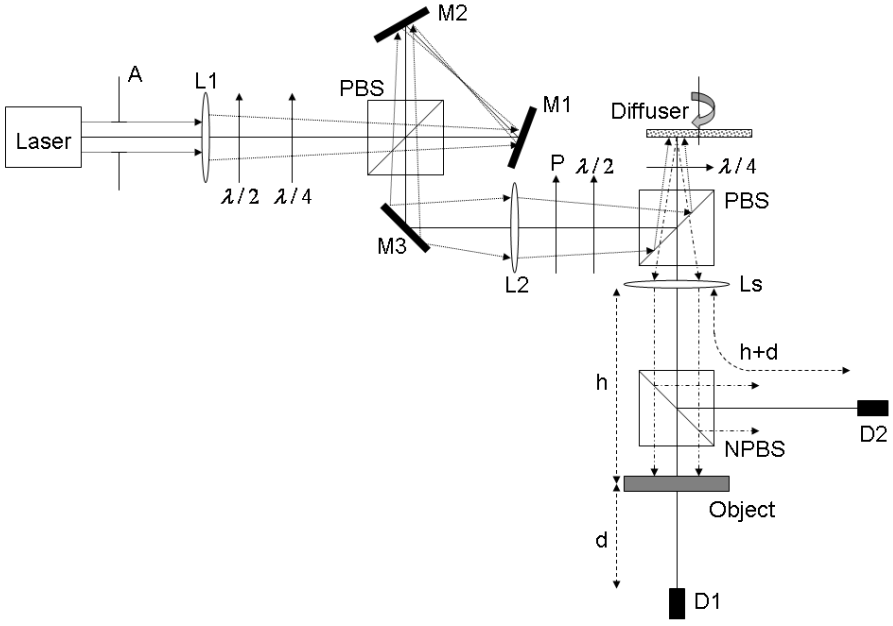

Figure 7.7: Schematic of the experimental setup used for correlated imaging with shaped spatially partially coherent light.

The partially coherent beam generated after L_s was divided in two identical replicas by a non-polarizing beam splitter NPBS. The object was a $500\mu m$ pitch step amplitude transmission grating located at a distance $d = 5cm$ from D_1. The light was detected by two photomultipliers connected with two fibers having a collection area smaller than the transverse coherence area of the incident beam. A coincidence circuit and three separate pulse counters were used simultaneously to record the intensities in both arms and the coincidence counts.

To demonstrate the phase sensitivity, the experiment was conducted for two different positions of the grating. The grating was first centered on the optical axis with minimum

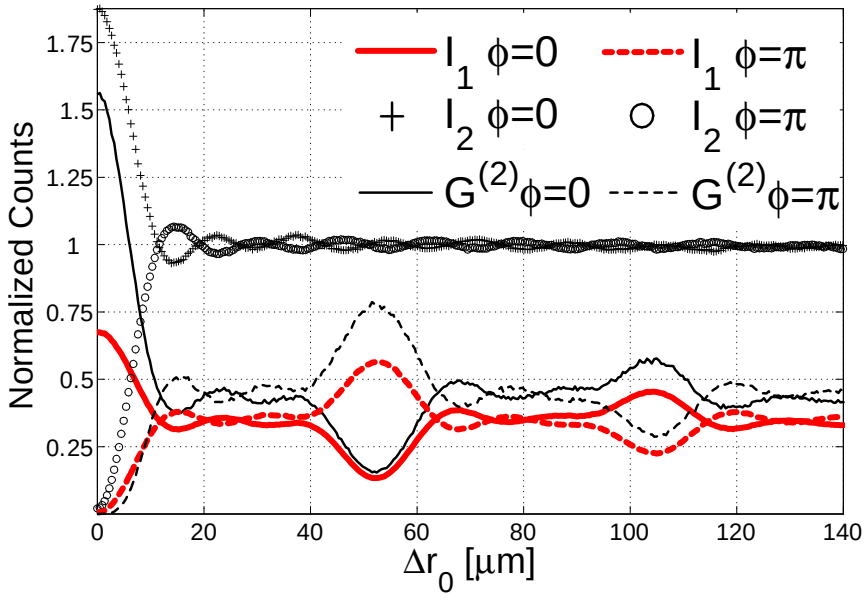

Figure 7.8: Coincidence counts $G^{(2)}$ and intensities in the object arm (I_1) and the reference arm (I_2) measured as a function of the source parameter Δr_0 for $\phi = 0$ (solid curve) and $\phi = \pi$ (dotted curve) when the grating is in the position $T(0) = 0$. The intensities are normalized with respect to the values obtained without the object and for $\Delta r_0 \sim 200\mu m$.

transmission, i.e. $T(0) = 0$. As shown in Fig. 7.8, the coincidence rate as well as the intensity in both arms were measured for $\phi = 0$ and $\phi = \pi$ as a function of the coherence parameter Δr_0 for values ranging from 0 to $140\mu m$. In this configuration, the first harmonic of $\widetilde{T}$ is negative as represented in Fig. 7.9(b1). The second position of the grating corresponds to maximum transmission of the grating on the optical axis, i.e. $T(0) = 1$. As shown in Fig. 7.9(a1), the first harmonic is positive in this case. Note that in both configurations of the

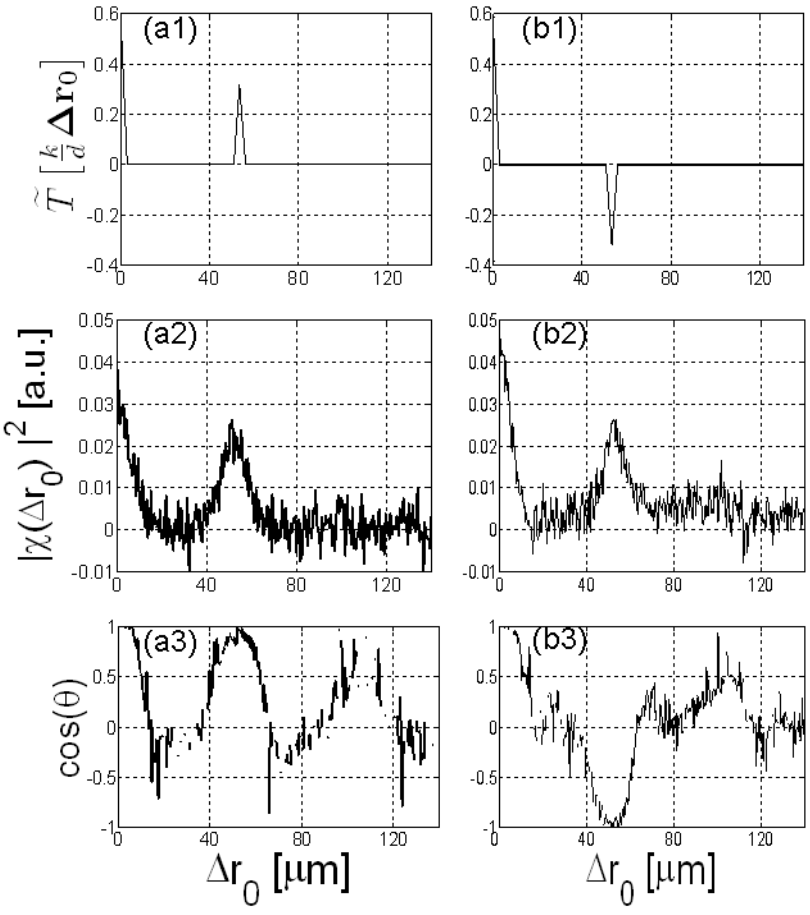

Figure 7.9: The analytic Fourier transform of the grating's transmittance is shown in graphic (a1) for the case $T(0) = 1$. The measured amplitude $|\chi_e|^2$ and the phase cosine are represented in plots (a2) and (a3), respectively. As shown in (b2) and (b3), the same measurements were performed in the case $T(0) = 0$ corresponding to the analytic Fourier transform plotted in (b1).

object, $\widetilde{T}$ is even, and, since I_s is constant for $m = 0$, the function g is real and χ_e relates directly to the even part of $\widetilde{T}$. Only measurements for $\phi = 0$ and $\phi = \pi$ are then necessary.

Using Eq. (7.24), we computed $|\chi_e(\Delta r_0)|^2$ and $\cos[\psi(\Delta r_0) + \theta_e(\Delta r_0) - \theta_e(0)]$ for both configurations. As expected, $|\chi_e|^2$ is not modified between the two grating's positions, as represented in Figs. 7.9(a2) and 7.9(b2). However, between the two cases in Figs. 7.9(a3) and 7.9(b3), we observe a difference in the phase term around $\Delta r_0 \sim 50\mu m$ where the harmonic's sign changes. This demonstrates the phase sensitivity of our procedure to the object's spatial frequencies. While our reconstruction was 1D, measuring a 2D Fourier transform requires rotating $\mathbf{\Delta r}_0$, which can easily be done using, for instance, a spatial light modulator.

7.3 Conclusion

In this chapter, we have demonstrated that, by varying the intensity distribution over an incoherent source, amplitude and phase information about the spatial frequencies of an object can be obtained from correlation measurements of intensity fluctuations. Since the detectors are fixed in both reference and object arms, our approach constitutes a robust detection scheme which could be of interest when environmental constrains do not permit the use of complex optical systems. This technique is also particularly attractive for x-ray diffraction because of the incoherence of most x-ray sources and the difficulty of fabricating lenses for such short wavelengths [95]. Finally, considering the duality between partial coherence and partial entanglement [101], an equivalent scheme using a biphoton source has been presented.

Even though the resolution in both schemes was demonstrated to be similar, entangled photon sources allow higher signal visibilities because the background noise inherent to quasi-thermal sources is absent.

CHAPTER 8

SUMMARY OF ORIGINAL CONTRIBUTIONS AND CONCLUSIONS

In many situations, the stochastic nature of electromagnetic radiation and the fluctuations in the optical properties of media in which this radiation propagates preclude a deterministic description and one must resort to a statistical characterization of the scattered fields. In this situation, light scattering approaches are used to determine the structural properties of heterogeneous media as described by statistical descriptors such as the correlation of its scattering potential. Although many sensing methods rely on measuring the coherence properties of scattered fields, the use of a variable spatial coherence gating has not been previously considered in the context of inverse scattering. In this dissertation, we have discussed and demonstrated a number of optical sensing techniques based on shaping the degree of spatial coherence of a quasi-homogeneous incident field.

Depending on the structural properties of an optically inhomogeneous medium, its complex susceptibility can have a correlation length either on the order or much larger than the inhomogeneities' size. The first situation is typical of a medium composed of a collection of independent particles. In this case, we have demonstrated experimentally that the radiative transfer equation makes a good description of the scattering process when the incident beam is partially coherent. By varying the coherence volume between limits, which are much larger

or smaller than the particle diameter, we have been able to recover both the concentration and the scattering cross-section of scattering particles[1]. Furthermore, understanding the subtle effect of coherence could also lead to novel approaches for controlling the divergence of beams propagating through scattering media and should be of interest for applications including guiding and tracking, and also active remote sensing through long atmospheric paths.

On the other hand, when the particles composing the medium possess a certain degree of correlation, the radiative transfer equation fails to accurately describe the propagation of the field. Using the first order Born approximation, we have introduced the principle of variable coherence tomography[2], where the structural properties of a medium are recovered by shaping the degree of spatial coherence of the incident beam and therefore inducing coherent scattering from different regions of the object. Our approach is appealing from a practical point of view because it requires only a spatially incoherent source with adjustable intensity distribution and far-field intensity measurements, which are much easier to implement than cross-spectral density measurements[3].

Since the Born approximation cannot be practically generalized to scattering orders higher than two, variable coherence tomography is not suited to measure long-range correlation properties of the complex susceptibility in multiple scattering media. However,

[1]E. Baleine, A. Dogariu, "Propagation of partially coherent beam through particulate media", J. Opt. Soc. Am. A **11**, 2041-2045 (2003)

[2]E. Baleine, A. Dogariu, "Variable coherence tomography", Opt. Lett. **29**, 1233-1235 (2004)

[3]E. Baleine, A. Dogariu, "Variable coherence tomography for inverse scattering problems", J. Opt. Soc. Am. A **21**, 1917-1923 (2004)

spatial coherence gating can be applied to enhance the long-range correlation of the field scattered from a diffusive medium. Using the phenomenon of coherent backscattering, we have demonstrated that specific scattering trajectories can be isolated by manipulating the degree of spatial coherence of the illuminating beam. As a result, depth resolved sensing of the scattering properties can be obtained, which is of great interest for the detection of subsurface hidden objects and the structural studies of multilayered or anisotropically inhomogeneous materials[4]. Moreover, considering an incident field composed of cross-polarized correlated speckles, our approach could be generalized to examine the polarized nature of the photon diffusion.

When using spatial coherence gating, each pair of correlated speckles relates to a particular scattering path or a specific pair of scatterers. Nevertheless, the recorded signal is a contribution from the scattered intensities originating from all the correlated speckle pairs composing the incident field. Consequently, the medium's parameters retrieved are spatially averaged over the size of the illuminating beam, thus, providing a robust description of the statistical properties of the object. While the field of view in the inversion procedure is set by the dimension of the incident field, the resolution is independently determined by the width of the coherence volume. This characteristic is quite different from conventional microscopic techniques, where the field of view observed decreases as the resolution improves. There is however another way to obtain high resolution independently of the field of view: in the practice of near-field optics, a small probing tip is scanned over a finite area. The

[4]E. Baleine, A. Dogariu, "Variable coherence enhanced backscattering", (in preparation).

resolution is determined by the size of the tip but the scanning mechanism over the sample limits practically the imaging area. To overcome this limitation and taking advantage of the parallel processing capability of spatial coherence gating, we have introduced the principle of variable coherence scattering microscopy[5] (VCSM), where the structural properties of subwavelength features are recovered by shaping the degree of coherence of an evanescent field. Remarkably, in this novel approach for solving the inverse problem, the subwavelength resolution is achieved from simple far-zone measurements. Besides, the technique does not require any moving parts, therefore making VCSM a good candidate for high throughput sensing and screening for various applications in biology and medicine, where current microscopic approaches rely on isolating small volumes of analyte or require high-resolution scanning over minute dimensions of a sample[6].

Because variable coherence tomography relies on spatially incoherent sources and simple detection schemes, this technique is particularly attractive for x-ray diffraction. However, using this tomographic procedure, only the amplitude of the Fourier frequencies of the complex susceptibility can be obtained. In order to also recover the phase information, we have introduced a lensless correlated imaging technique, where the Fourier transform of an object is retrieved by modulating the intensity distribution across a spatially incoherent source and measuring the correlation of intensity fluctuations recorded by two different detectors[7].

[5]E. Baleine, A. Dogariu, "Variable coherence scattering microscopy", Phys. Rev. Lett. **95**, 193904 (2005)

[6]E. Baleine, A. Dogariu, "Variable coherence allows sensing with subwavelength resolution", Optics & Photonics News (OPN), *Optics in 2006*, Vol. **17**, No. 12 (2006).

[7]E. Baleine, G. S. Agarwal, A. Dogariu, "Correlated imaging with shaped spatially partially coherent light", Opt. Lett. **31**, 2124-2126 (2006)

Using the duality between partial coherence and partial entanglement, we have proposed an equivalent scheme where the degree of entanglement between two photons is shaped.

In closing, we emphasize that the idea of using the spatial coherence properties of radiation in tomographic procedures is applicable to any type of electromagnetic radiation. Operating on principles of statistical optics, such a sensing approach can become an alternative for various target detection schemes, cutting-edge microscopies or x-ray imaging methods.

APPENDIX

PUBLICATIONS AND PRESENTATIONS

Publications

1. E. Baleine, A. Dogariu, "Variable coherence enhanced backscattering", (in preparation).

2. E. Baleine, A. Dogariu, "Variable Coherence Allows Subwavelength Resolution Sensing", Optics & Photonics News , *Optics in 2006*, OPN **17**(12), 23 (2006).

3. E. Baleine, G. S. Agarwal, A. Dogariu, "Correlated imaging with shaped spatially partially coherent light", Opt. Lett. **31**, 2124-2126 (2006).

4. E. Baleine, A. Dogariu, "Variable coherence scattering microscopy", Phys. Rev. Lett. **95**, 193904 (2005).

5. E. Baleine, A. Dogariu, "Variable coherence tomography for inverse scattering problems", J. Opt. Soc. Am. A **21**, 1917-1923 (2004).

6. E. Baleine, A. Dogariu, "Variable coherence tomography", Opt. Lett. **29**, 1233-1235 (2004).

7. M. Mujat, E. Baleine, A. Dogariu, "Interferometric imaging polarimeter", J. Opt. Soc. Am. A **21**, 2244-2249 (2004).

8. E. Baleine, A. Dogariu, "Propagation of partially coherent beam through particulate media", J. Opt. Soc. Am. A **11**, 2041-2045 (2003).

9. A. Zoubir, J. Eichenholz, E. Fujiwara, D. Grojo, E. Baleine, A. Rapaport, M. Bass, B. Chai, M. Richardson, "Non-critical phase-matched second harmonic generation in GdYCOB", Appl. Phys. B **77**, 437-440 (2003).

Presentations

1. E. Baleine, A. Dogariu, "Variable coherence enhanced backscattering" (FWY2, Oral), OSA Frontiers in Optics, October 2006, Rochester, New York.

2. E. Baleine, A. Dogariu, "Correlated imaging with shaped partially coherent light" (FTuM5, Oral), OSA Frontiers in Optics, October 2005, Tucson, Arizona.

3. E. Baleine, L. Denney, T. Wilbur, J. Biggerstaff, A. Dogariu, "Optical hematorheology using multimode common path interferometry" (JWA32, Poster), OSA Frontiers in Optics, October 2005, Tucson, Arizona.

4. E. Baleine, A. Dogariu, "Variable coherence microscopy" (5896-09 S2B, Oral), SPIE – Optics and Photonics, Unconventional Imaging, August 2005, San Diego, California.

5. E. Baleine, A. Dogariu, "Variable coherence scattering microscopy" (CTuB3, Oral), OSA – topical meeting on Computational Optical Sensing and Imaging, June 2005, Charlotte, North Carolina.

6. E. Baleine, A. Dogariu, "Variable coherence tomography" (Oral), Post Deadline Session, CLEO OSA, May 2004, San Francisco, California.

7. E. Baleine, A. Dogariu, "Variable coherence tomography for measuring the pair correlation function" (FH37, Poster), BIOMED – biomedical optics – OSA, April 2004, Miami, Florida.

8. E. Baleine, A. Dogariu, "Propagation and scattering of partially coherent beams in Particulate Media" (Poster), OSA annual meeting, September 2002,Orlando, Florida.

LIST OF REFERENCES

[1] M. Mujat and A. Dogariu, "Real-Time Measurement of the Polarization Transfer Function", Appl. Opt. **40**, 34-44 (2001).

[2] C. Schwartz and A. Dogariu, "Enhanced backscattering of optical vortex fields", Opt. Lett. **30**, 1431-1433 (2005).

[3] E. Wolf, "Principles of development of diffraction tomography", in Trends in Optics, Vol. 3, ed. A. Consortini (Academic press, San Diego, Calif., 1996), pp. 83-110.

[4] D. G. Fisher and E. Wolf, "Theory of diffraction tomography for quasi-homogeneous random objects", Opt. Com. **133**, 17-21 (1997).

[5] S. Fantini, S. A. Walker, M. A. Franceschini, M. Kaschke, P. M. Schlag, and K. T. Moesta, "Assessment of the size, position, and optical properties of breast tumors in vivo by noninvasive optical methods", Appl. Opt. **37**, 1982 -1988 (1998).

[6] A. F. Fercher, W. Drexler, C. K. Hitzenberger and T. Lasser, "Optical coherence tomography–principles and applications", Rep. Prog. Phys. **66**, 239-303 (2003).

[7] D. Huang and al., "Optical coherence tomography", Science **254**, 1178-1181 (1991).

[8] G. Popescu and A. Dogariu, "Optical path-length spectroscopy of wave propagation in random media", Opt. Lett. **24**, 442-444 (1999).

[9] A. Dogariu, C. Kutsche, P. LiKamWa, G. Boreman, and B. Moudgil, "Time-domain depolarization of waves retroreflected from dense colloidal media", Opt. Lett. **22**, 585-587 (1997).

[10] P. S. Carney, *Optical Theorems in Statistical Wavefields with Applications*, PhD thesis, University of Rochester, Rochester, NY, June 1999.

[11] A. Walther, "Radiometry and coherence", J. Opt. Soc. Am. **63**, 1622-1623 (1973).

[12] L. A. Apresyan and Y. A. Kravtsov, *Radiation Transfer - Statistical and Wave Aspects* (Gordon & Breach, 1996).

[13] P. M. Voyles, J. M. Gibson, and M. M. J. Treacy, "Fluctuation Microscopy: A probe of Atomic Correlations in Disordered Materials", J. Electron Microscopy **49**, 259 (2000).

[14] P. S. Carney, E. Wolf and G. S. Agarwal, "Diffraction tomography using power extinction measurements", J. Opt. Soc. Am. A **16**, 2643-2648 (1999).

[15] J. Rosen and M. Takeda, "Longitudinal spatial coherence applied for surface profilometry", Appl. Opt. **39**, 4107-4111 (2000).

[16] Yu. N. Barabanenkov, "On the spectral theory of radiation transport equations", Sov. Phys. JETP **29**, 679-684 (1969).

[17] Y. L. Kim et al., "Low-coherent backscattering spectroscopy for tissue characterization", Appl. Opt. **44**, 366-377 (2005).

[18] E. Akkermans, P. E. Wolf, R. Maynard, and G. Maret, "Therotical study of the coherent backscattering of light by disordered media", J. Phys. France **49**, 77-98 (1988).

[19] E. Betzig and J. K. Trautman, "Near-Field Optics: Microscopy, Spectroscopy, and Surface Modification Beyond the Diffraction Limit", Science **257**, 189-195 (1992).

[20] L. Mandel and E. Wolf, *Optical Coherence and Quantum Optics* (Cambridge University Press, Cambridge, 1995).

[21] L. Mandel and E. Wolf, *Optical Coherence and Quantum Optics* (Cambridge University Press, Cambridge, 1995), Chap 4.3.1.

[22] E. Wolf, New theory of partial coherence in the space-frequency domain. Part I: spectra and cross spectra of steady state sources", J. Opt. Soc. Am. **72**, 343-351 (1982).

[23] E. Wolf, "Unified theory of coherence and polarization of random electromagnetic beams", Phys. Lett. A **312**, 263-267 (2003).

[24] L. Mandel and E. Wolf, *Optical Coherence and Quantum Optics* (Cambridge University Press, Cambridge, 1995), Chap 3.2.2.

[25] J. J. Greffet, M. De La Cruz-Gutierrez, P. V. Ignatovich and A. Radunsky, "Influence of spatial coherence on scattering by a particle", J. Opt. Soc. Am. A **20**, 2315-2320 (2003).

[26] L. Mandel and E. Wolf, *Optical Coherence and Quantum Optics* (Cambridge University Press, Cambridge, 1995), Chap 5.3.2.

[27] W. H. Carter and E. Wolf, "Coherence and radiometry with quasihomogeneous planar sources", J. Opt. Soc. Am. **67**, 785-796 (1977).

[28] L. Mandel and E. Wolf, *Optical Coherence and Quantum Optics* (Cambridge University Press, Cambridge, 1995), Chap 4.4.4.

[29] J. Turunen, A. Vasara and A. T. Friberg, "Propagation invariance and self-imaging in variable-coherence optics", J. Opt. Soc. Am. A **8**, 282-289 (1991).

[30] J. Turunen, "Invariant propagation of uniform-intensity Schell-model fields", J. Mod. Opt. **49**, 1795-1799 (2002).

[31] M. Born and E. Wolf, *Principles of Optics*, 7^{th} Ed. (Cambridge University Press, Cambridge, 2003).

[32] J. Jannson, T. Jannson and E. Wolf, "Spatial coherence discrimination in scattering", Opt. Lett. **13**, 1060-1062 (1988).

[33] C. Iaconis and I. A. Walmsley, "Direct measurement of the two-point field correlation function", Opt. Lett. **21**, 1783-1785 (1996).

[34] M. G. Raymer, M. Beck, and D. F. McAlister, "Complex wave-field reconstruction using phase-space tomography", Phys. Rev. Lett. **72**, 1137-1140 (1994).

[35] U. Frisch, Wave propagation in random media. *Probabilistic Methods in Applied Mathematics*, ed by. A. T. Bharucha-Reid (Academic Press, New York, 1968).

[36] H.C. van de Hulst, *Light Scattering by Small Particles* (Dover publications, New York, 1981).

[37] S. Chandrasekhar, *Radiative Transfer* (Dover, 1960).

[38] A. Ishimaru, *Wave propagation and scattering in random media* (Academic Press, New York, 1978).

[39] M. S. Patterson, B. Chance, and B. C. Wilson, "Time resolved reflectance and transmittance for the noninvasive measurement of tissue optical properties," Appl. Opt. **28**, 2331-2336 (1989).

[40] D. J. Pine, D. A. Weitz, P. M. Chaikin, and E. Herbolzheimer, "Diffusing-wave spectroscopy", Phys. Rev. Lett. **60**, 1134-1137 (1988).

[41] R. F. Lutomirski, "Atmospheric degradation of electrooptical system performance", Appl. Opt. **17**, 3915-3921 (1978).

[42] N. S. Kopeika, D. Sadot, and I. Dror, "Aerosol light scatter vs turbulence effects in image blur", in *Optics Atmospheric Propagation and Adaptive Systems II*, A. Kohnle and A. D. Devir, eds., Proc. SPIE **3219**, 44-51 (1998).

[43] Y. Kuga and A. Ishimaru, "Modulation transfer function and image transmission through randomly distributed spherical particles", J. Opt. Soc. Am. A **2**, 2330-2336 (1985).

[44] A. Wax and J. E. Thomas, "Measurement of smoothed Wigner phase-space distributions for small-angle scattering in a turbid medium", J. Opt. Soc. Am. A **15**, 1896-1908 (1998).

[45] C.-C. Cheng and M. G. Raymer, "Propagation of transverse optical coherence in random multiple-scattering media", Phys. Rev. A **62**, 023811 (2000).

[46] G. Gbur and E. Wolf, "Spreading of partially coherent beams in random media", J. Opt. Soc. Am. A **19**, 1592-1598 (2002).

[47] S.A Ponomarenko, J.-J. Greffet, and E. Wolf, "The diffusion of partially coherent beams in turbulent media", Opt. Com. **208**, 1-8 (2002).

[48] A. Dogariu and S. Amarande, "Propagation of partially coherent beams: the turbulence-induced degradation", Optics Lett. **28**, 10-12 (2003).

[49] P. S. Carney, E. Wolf and G. S. Agarwal, "Statistical generalizations of the optical cross-section theorem with application to inverse scattering", J. Opt. Soc. Am. A **14**, 3366-3371 (1997).

[50] P. S. Carney and E. Wolf, "An energy theorem for scattering of partially coherent beams", Opt. Commun. **155**, 1-6 (1998).

[51] F. Gori, C. Plama, and M. Santarsiero, "A scattering experiment with partially coherent light", Opt. Commun. **74**, 353-356 (1990).

[52] For a review, see M. J. Bastiaans, "Application of the Wigner distribution function to partially coherent light", J. Opt. Soc. Am. A **3**, 1227-1238 (1986).

[53] H. T. Yura, L. Thrane and P. E. Andersen, "Closed-form solution for the Wigner phase-space distribution function for diffuse reflection and small-angle scattering in a random medium", J. Opt. Soc. Am. A **17**, 2464-2474 (2000).

[54] S. John, G. Pang, and Y. Yang, "Optical coherence propagation and imaging in a multiple scattering medium", J. Biomed. Opt. **1**, 180-191 (1996).

[55] D. A. de Wolf, "Coherence of a light beam through an optically dense turbid layer", Appl. Opt. **17**, 1280-1285 (1978).

[56] W. Wang, H. Kozaki, J. Rosen and M. Takeda,"Synthesis of longitudinal coherence functions by spatial modulation of an extended light source: a new interpretation and experimental verifications", Appl. Opt. **41**, 1962-1971 (2002).

[57] W. H. Carter and E. Wolf, "Scattering from quasi-homogeneous media", Opt. Com. **67**, 85-90 (1988).

[58] J. Rosen and A. Yariv, "Longitudinal partial coherence of optical radiation", Opt. Com. **117**, 8-12 (1995).

[59] A. Zarubin, "Three-dimensional generalization of the Van Cittert-Zernike theorem to wave and particle scattering", Opt. Com. **100**, 491-507 (1993).

[60] E. Baleine and A. Dogariu, "Variable coherence tomography", Opt. Lett. **29**, 1233-1235 (2004).

[61] T. Okamoto, T. Asakura, "Enhanced backscattering of partially coherent light", Opt. Lett. **21**, 369-371 (1996).

[62] M. Tomita, H. Ikari, , " Influence of finite coherence length of incoming light on enhanced backscattering", Phys. Rev. B **43**, 3716-3719 (1991).

[63] Y. N. Barabanenkov, Y. A. Kravtsov, V. D. Ozrin and A. I. Saichev, "Enhanced Backscattering in Optics", Progress in Optics 29 (E. Wolf ed.) (North Holland, Amsterdam, 1991).

[64] Y. Kuga, A. Ishimaru, "Retroreflectance from a dense distribution of spherical particles", J. Opt. Soc. Am. A **1**, 831-835 (1984).

[65] F. Reil and J. E. Thomas, "Observation of phase conjugation of light arising from enhanced backscattering in a random medium", Phys. Rev. Lett. **95**, 143903 (2005).

[66] H. M. Escamilla, E. R. M´endez, and Amalia Martinez, "Image formation in the double-passage scattering configuration", J. Opt. Soc. Am. A **13**, 1439-1447 (1996).

[67] E. Akkermans, G. Montambaux, "Mesoscopic physic of photons", J. Opt. Soc. Am. B **21**, 101-112 (2004).

[68] E. Akkermans, P. E. Wolf, and R. Maynard, "Coherent Backscattering of Light by Disordered Media: Analysis of the Peak Line Shape", Phys. Rev. Lett. **56**, 1471-1474 (1986).

[69] J. X. Zhu, D. J. Pine, and D. A. Weitz, "Internal reflection of diffusive light in random media", Phys. Rev. A **44**, 3948–3959 (1991).

[70] M. Ospeck and S. Fraden ,"Influence of reflecting boundaries and finite interfacial thickness on the coherent backscattering cone", Phys. Rev. E **49**, 4578–4589 (1994).

[71] M. Xu and R. R. Alfano, "Random Walk of Polarized Light in Turbid Media", Phys. Rev. Lett. **95**, 213901 (2005).

[72] M. J. Stephen and G. Cwilich, "Rayleigh scattering and weak localization: Effects of polarization", Phys. Rev. B **34**, 7564–7572 (1986).

[73] V. L. Kuzmin, V. P. Romanov, and L. V. Kuzmin, "Depolarization of coherent backscattering", Opt. Spectrosc. **72**, 125-130 (1992).

[74] L. F. Rojas-Ochoa, D. Lacoste, R. Lenke, P. Schurtenberger, and F. Scheffold, "Depolarization of backscattered linearly polarized light", J. Opt. Soc. Am. A **21**, 1799-1804 (2004).

[75] S. Feng and F. Zeng, "Monte Carlo Simulations of Photon Migration Path Distributions in Multiple Scattering Media", SPIE proc. **1888**, 78-89 (1993).

[76] W. Cui, C. Kumar, and B. Chance, "Experimental study of migration depth for the photons measured at sample surface", SPIE proc. **1431**, 180-191 (1991).

[77] M. Störzer, P. Gross, C. M. Aegerter, and G. Maret, "Observation of the Critical Regime Near Anderson Localization of Light", Phys. Rev. Lett. **96**, 063904 (2006).

[78] R. C. Reddick, R. J. Warnack and T. L. Ferrel, "New form of scanning optical microscopy", Phys. Rev. B **39**, 767-770 (1989).

[79] Adam Wax, C. Yang, V. Backman, K. Badizadegan, C. W. Boone, R. R. Dasari, and M. S. Feld, "Cell organization and sub-structure measured using angle-resolved low coherence interferometry", Biophys. J. **82**, 2256-2264 (2002).

[80] P. S. Carney and J. C. Schotland, "Three-dimensional total internal reflection microscopy ",Opt. Lett. **26**, 1072-1074 (2001).

[81] P. S. Carney, V. A. Markel and J. C. Schotland, "Near-Field Tomography without Phase Retrieval", Phys. Rev. Lett. **86**, 5874-5877 (2001).

[82] G. S. Agarwal, "Subwavelength resolution using evanescent waves", Pure Appl. Opt. **7**, 1143-1149 (1998).

[83] V. A. Loiko, V. P. Dick and A. P. Ivanov, "Features in coherent transmittance of a monolayer of particles", J. Opt. Soc. Am. A **17**, 2040-2045 (2000).

[84] M. Baus and J. L. Colot, "Theoretical structure factors for hard-core fluids", J. Phys. C: Solid State Phys. **19**, L643-L648 (1986).

[85] M. Born and E. Wolf, *Principle of Optics* (Cambridge U. Press, Cambridge, England, 1999), 7th ed., Chap. 1, pp. 38-51.

[86] G. E. Cragg and P. T. C. So, "Lateral resolution enhancement with standing evanescent waves", Opt. Lett. **25**, 46-48 (2000).

[87] Backman, V., M. B. Wallace, L. T. Perelman, J. T. Arendt, R. Gurjar, M. G. Muller, Q. Zhang, G. Zonios, E. Kline, T. McGillican, S. Shapshay, T. Valdez, K. Badizadegan, J. M. Crawford, M. Fitzmaurice, S. Kabani, H. S. Levin, M. Seiler, R. R. Dasari, I. Itzkan, J. Van Dam, and M. S. Feld, "Detection of preinvasive cancer cells", Nature **406**, 35-36 (2000).

[88] V. Backman, V Gopal, M. Kalashnikov, K. Badizadegan, R. Gurjar, A. Wax, I. Georgakoudi, M. Mueller, C.W. Boone, R. R. Dasari, and M. S. Feld, "Measuring cellular structure at sub-micrometer scale with light scattering spectroscopy", IEEE J Sel Top Quant. Elec. **7**, 887-893 (2001).

[89] T. B. Pittman, Y. H. Shih, D. V. Strekalov, and A. V. Sergienko, "Optical imaging by means of two-photon quantum entanglement", Phys. Rev. A **52**, R3429 (1995).

[90] D. V. Strekalov, A. V. Sergienko, D. N. Klyshko, and Y. H. Shih, "Observation of Two-Photon "Ghost" Interference and Diffraction", Phys. Rev. Lett. **74**, 3600-3603 (1995).

[91] A. Gatti, E. Brambilla, and L. A. Lugiato, "Entangled Imaging and Wave-Particle Duality: From the Microscopic to the Macroscopic Realm", Phys. Rev. Lett. **90**, 133603 (2003).

[92] R. S. Bennink, S. J. Bentley, and R. W. Boyd, "Two-Photon Coincidence Imaging with a Classical Source", Phys. Rev. Lett. **89**, 113601 (2002).

[93] A. Valencia, G. Scarcelli, M. D'Angelo, and Y. Shih, "Two-Photon Imaging with Thermal Light", Phys. Rev. Lett. **94**, 063601 (2005).

[94] D. Zhang, Y. H. Zhai, and L. A. Wu, "Correlated two-photon imaging with true thermal light", Opt. Lett. **30**, 2354 (2005).

[95] J. Cheng and S. Han, "Incoherent Coincidence Imaging and Its Applicability in X-ray Diffraction", Phys. Rev. Lett. **92**, 093903 (2004).

[96] M. Bache, E. Brambilla, A. Gatti, and L. A. Lugiato, "Ghost imaging using homodyne detection", Phys. Rev. A **70**, 023823 (2004).

[97] L. Mandel and E. Wolf, *Optical Coherence and Quantum Optics* (Cambridge University Press, Cambridge, 1995), Chap 14.7.

[98] M. Bache, D. Magatti, F. Ferri, A. Gatti, E. Brambilla, and L. A. Lugiato, "Coherent imaging of a pure phase object with classical incoherent light", Phys. Rev. A **73**, 053802 (2006).

[99] A. Gatti, E. Brambilla, M. Bache, and L. A. Lugiato, "Correlated imaging, quantum and classical", Phys. Rev. A **70**, 013802 (2004).

[100] D. N. Klyshko, *Photons and Nonlinear Optics* (Gordon and Breach, New York, 1988).

[101] B. E. A. Saleh, A. F. Abouraddy, A. V. Sergienko, and M. C. Teich, "Duality between partial coherence and partial entanglement", Phys. Rev. A **62**, 043816 (2000).

[102] M. D'Angelo, A. Valencia, M. H. Rubin and Y. Shih, "Resolution of quantum and classical ghost imaging", Phys. Rev. A **72**, 013810 (2005).

[103] A. Gatti, E. Brambilla, M. Bache, and L. A. Lugiato, "Ghost Imaging with Thermal Light: Comparing Entanglement and Classical Correlation", Phys. Rev. Lett. **93**, 093602 (2004).